SCUOLA DI DOTTORATO

UNIVERSITÀ DEGLI STUDI DI MILANO-BICOCCA

School of Medicine and Surgery

PhD Program in Molecular and Translational Medicine
(DIMET)

XXXIII Cycle

Nanomechanics in Cancer Research

Buglione Enrico

Registration number: 835767

Tutor: Prof. Francesco Mantegazza

Co-tutor: Prof. Massimo Masserini

Coordinator: Prof. Andrea Biondi

ACADEMIC YEAR

2019/2020

CHAPTER 1

General introduction

1.1 Cancer 7

1.1.1 General features 7

1.1.2 Cancer onset 8

1.1.3 Oncogenes 9

1.1.4 Regulation of the proto-oncogene *c-KIT* 10

1.1.5 G-quadruplexes 11

1.1.6 Cancer progression 14

1.1.7 Chronic Lymphocytic Leukemia 15

1.1.8 BTK signaling 16

1.1.9 BTK inhibitors 17

1.2 Physics of cancer 20

1.2.1 Cells in motion 20

1.2.2 Moving from the inside 21

1.2.3 Pressure modification 23

1.2.4 Mechanoreciprocity 25

1.2.5 Mechanoreciprocity in cancer 26

1.2.6 The stiffness in cellular biophysics 27

1.3 Nanomechanics 29

1.3.1 Origins, history and achievements 29

1.3.2 Nanomechanical techniques 30

1.3.3 Magnetic Tweezers 31

1.3.4 Atomic Force Microscopy 34

1.3.5 Real-time deformability cytometry 37

1.3.6 Nanomechanical application in cancer research 39

1.4 Scope of the thesis 41

1.5 Bibliography 44

CHAPTER 2

Nanomechanics of G-quadruplexes within the promoter of the *c-kit* oncogene.

2.1 Abstract 54

2.2 Introduction 55

2.3 Results 59

2.4 Discussion 72

2.5 Conclusions 78

2.6 Methods 79

2.7 Supplementary data 84

2.8 Bibliography 96

CHAPTER 3

Targeted therapy affects Chronic Lymphocytic Leukemia cells mechanical properties.

3.1 Abstract 102

3.2 Introduction 103

3.3 Methods 107

3.4 Results 110

3.5 Discussion 124

3.6 Conclusions 129

3.7 Supplementary methods 130

3.8 Supplementary results 131

3.9 Bibliography 146

CHAPTER 4

Summary, conclusions and future perspectives 151

4.1 Bibliography 156

4.2 Publication outside the thesis topic 158

Chapter 1

General introduction

1.1 Cancer

1.1.1 General features

The term cancer indicates a large group of diseases, whose main feature is an abnormal and uncontrolled cell growth, potentially diffusible throughout the whole body. Despite the great breakthroughs of the past decades in shedding light on the pathological mechanisms of cancer, as well as in developing anticancer drugs, finding a cure to the many forms of cancer which do exist is still a challenging task [Hanahan D and Weinberg RA, 2011]. Indeed, the current estimation of people affected by cancer is more than 100 million, causing about 8.8 million deaths per year (15.4% of total deaths) [Haidong W *et al.*, 2015]. For such reasons, until last year, cancer was the most studied disease.

In most cases, cancer-related symptoms occur only in late stages of the disease, making the identification of cancer difficult. Currently, screening tests remain the most effective method to obtain an early diagnosis. Depending on the type of cancer, on its location and on its stage, different treatments are available, including chemotherapies, radiations and hormone therapies as well as surgery. The therapies known so far act at the systemic level, producing often severe side effects. In the last few decades, lots of efforts were made in developing targeted therapies designed to locally aim cancer, thus reducing side effects. Despite the efforts made so far, most forms of cancer still remain incurable. For this reason, prevention and habitual screening

represent the pillars of the fight against this disease [World Cancer Report, 2014].

1.1.2 Cancer onset

Tumorigenesis is a multifactorial process triggered by genetic and/or epigenetic factors. As a matter of fact, both changes in the DNA sequence (genetic) and in the gene expression scheme (epigenetic) can contribute to cancer onset. Cancer can occur in any district of the human body, typically rising from a single cell. The different types of cancer can be classified in several major categories depending on the cell type from which it arises (e.g. carcinoma, sarcoma, lymphoma, blastoma, germ cell tumor). Each class presents peculiar and distinctive features, often very different from each other. However, all types of cancer share common hallmarks at the basis of their onset. In fact, an altered receipt of cell growth and division signals is a fundamental prerequisite for any kind of cancer, as well as the avoidance of programmed cell death. Together, those conditions result in a continuous, uncontrolled and limitless cycle of cell growth and division. A further common feature is the capability to secure a source of nutrition by promoting blood vessel formation within its mass that otherwise would undergo necrosis. Finally, the last shared feature in all cancer types is the potential ability to form metastases and, thus, to invade almost any kind of tissue within the organism. Such ability, known as malignant progression, allows cancer to form new pathological sites in every part of the body through a local

diffusion or adopting lymphatic or hematogenous spread [Hanahan D and Weinberg RA, 2000].

1.1.3 Oncogenes

As mentioned above, one of the major causes of cancer onset is represented by genetic mutations, which are in turn often promoted by environmental factors such as chemicals, radiations, diet and lifestyle. In addition, a small percentage of events is due to bacterial or viral infections rather than genetic inheritance. In most cases, the mutation occurs on a so-called proto-oncogene, or on a sequence that regulates its expression. A proto-oncogene is a gene that encodes for a protein involved in the cell cycle regulation, in the cell growth or in the control of apoptosis. As long as its expression is kept under control, the proto-oncogene performs its function as a normal gene. Nevertheless, a mutation that alters its function, whether up or down regulative depending on the gene function, can turn it into an oncogene, that usually predispose the cell to become cancerous. Indeed, the loss of control on the expression of a proto-oncogene typically results in a loss of control on the cell cycle regulation, thus allowing the cell to increase its replication rate. In addition, an increased and uncontrolled proliferation provides an evolutionary advantage to the cancerous cells with respect to the neighbor cells, allowing a quick overcome of cancer at the expenses of nearby healthy cells [Negrini S *et al.*, 2010].

1.1.4 Regulation of the proto-oncogene *c-KIT*

c-KIT is a well-known proto-oncogene encoding for a type III tyrosine-kinase receptor (KIT or CD117), a mast/stem cell growth factor receptor expressed on the surface of several cell types. In physiological conditions, when the receptor binds to the Stem Cell Factor (SCF), it undergoes dimerization thus activating its kinase activity and transducing a signal of survival and growth to the cell [Blume-Jensen P *et al.*, 1991]. Considering the key role of KIT in regulating critical phases, it follows that any dysregulation of its expression can produce a strong impact on the cell cycle. Indeed, an overexpression of this protein is frequently associated with different forms of cancer, such as mastocytosis, gastrointestinal stromal tumors, lung cancer and some types of leukemia [Liang J *et al.*, 2013].

The control of the *c-KIT* gene expression is largely dependent on its regulatory sequences. Among them, the *c-KIT* proximal promoter, which is located immediately upstream the gene, appears to play a key role in the regulation of KIT expression [Zorzan E *et al.*, 2016]. Notably, the overproduction of CD117 due to a constitutive expression of its gene has been reported to represent the primary pathogenic event in gastrointestinal stromal tumors [Sakurai S *et al.*, 1999]. The structural analysis of the *c-KIT* promoter revealed the presence of 3 distinct G-quadruplexes (G4s) within its sequence, called respectively from 5' kit2 [Fernando H *et al.*, 2006], kit* [Kotar A *et al.*, 2019] and kit1 [Rankin S *et al.*, 2005; Ceschi S and Sissi C, 2020].

1.1.5 G-quadruplexes

G-quadruplexes are single-stranded tetrahelical structures consisting of planar guanine quartets occurring in DNA G-rich regions [Bochman M *et al.*, 2012] (figure 1). The architecture of G4s is largely dependent on the DNA sequence, in particular on the position of the guanines that compose the structure. According to the position and distance of the guanine-guanine interactions, the strand can assume different orientations, thus producing a rich polymorphism of G4s [Lightfoot HL *et al.*, 2019].

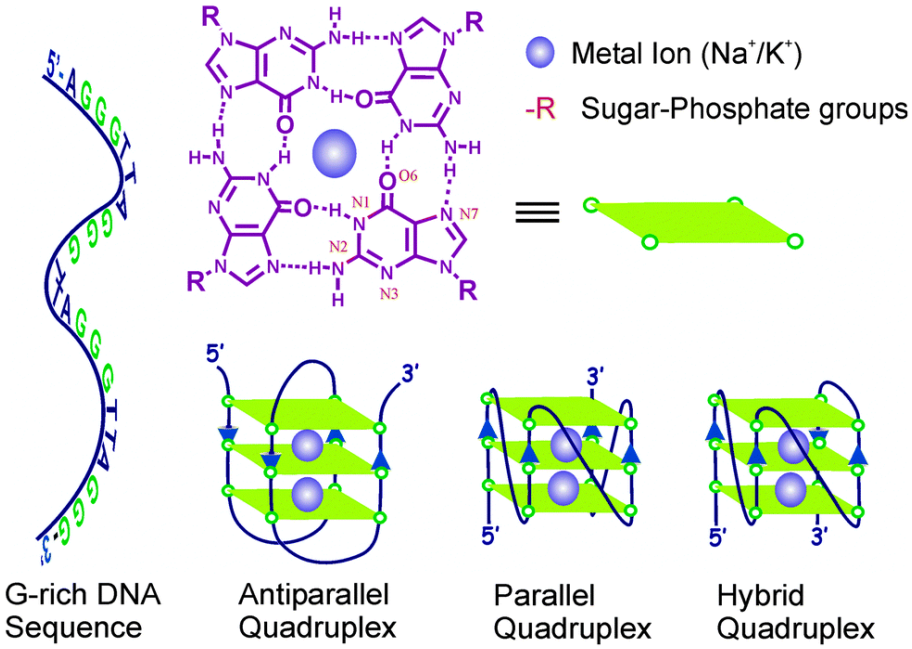

Figure 1. Schematic representation of the three-dimensional structures of G-quadruplexes. Depending on the strand orientation, G4s show several polymorphisms [image taken from Bhasikuttan AC and Mohanty J, 2015].

The complete folding of the structure requires the presence of specific metal ions, which are known to play a role in the coordination of the assembly of the four guanines that take part in the planar structure as well as in the stacking of different plans [Hänsel-Hertsch R *et al.*, 2017]. Not all the metal ions involved in the folding have shown the same affinity to the structure: among them, K^+ is the most effective in coordinating the folding, so its presence raises the G4 formation probability. Na^+ likewise contributes to the folding, although showing lower affinity compared to K^+. Finally, Li^+ ion exhibits the lowest affinity to the quartets, considerably reducing the probability of G4 formation

if administered alone in a controlled system [Bhattacharyya D *et al*., 2016].

A considerable number of G4s was found within the telomeric regions of human chromosomes, where they are known to play a role in the prevention of telomere shortening and thus in the process of senescence [Victorelli S and Passos JF, 2017]. Furthermore, some G4s have been observed within the DNA regulatory regions, in particular among the promoter regions [Du Z *et al.*, 2009]. In this case, they are supposed to take part in the control of the transcription of many genes [Maizels N and Gray LT, 2013]. This is also the case of the *c-KIT* promoter, where the lack of a typical "TATA box" suggests the presence of alternative regulatory paths, as confirmed by an increasing number of studies [Yamamoto K *et al.*, 1993; McLuckie K *et al.*, 2011]. The three G4s enclosed in this sequence presumably have a role in the recognition of the promoter and in the assembly of the transcriptional machinery for the gene expression. In fact, recent works demonstrated that the ubiquitous transcription factor SP1 shows a high affinity to G4 structures, in particular to kit* [Raiber EA *et al.*, 2012; Yamamoto K *et al.*, 1993]. Moreover, the three single-stranded structures are thought to interact each other, resulting in a cooperative effect. This phenomenon has been observed in the case of the kit2-kit* crosstalk, which raises the stability of both structures thus extending their half-life [Rigo R and Sissi C, 2017]. Therefore, the crucial role of G4s in the regulation of this oncogene makes them eligible targets for the study of cancer onset and eventually for the

design of new targeted drugs [Balasubramanian S *et al.*, 2011; Rigo R *et al.*, 2016].

1.1.6 Cancer progression

One of the most deadly and nefarious prerogatives of cancer is represented by its ability to potentially spread throughout the body forming new growing sites. Such a process can follow two different footpaths: the cancer invasion, a simple penetration of tumorous cells across neighboring tissues, and the metastases, a broad spread via the hematogenous or the lymphatic streams.

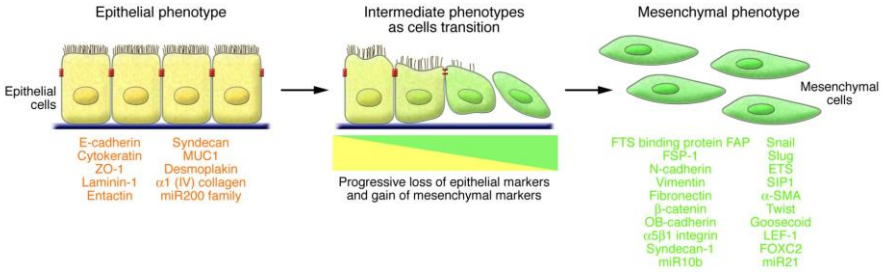

Figure 2. Schematic representation of the Epithelial-Mesenchymal Transition process outlining the loss of polarity and the change in shape of the involved cells. The complete transition may require several days, suggesting that changes produce various stages from the epithelial to the mesenchymal phenotype [image taken from Kalluri R and Weinberg RA, 2009].

The metastasization represents the final stage of cancer progression, characterized by an increased aggressiveness and malignancy of cancer cells. At this stage, cells from primary tumor undergo the so-called Epithelial-Mesenchymal Transition (EMT) (figure 2), a cellular

reprogramming characterized by a change in the morphology, a lack in the cadherin mediated cell-cell adhesion and a loss of polarity [Kalluri R and Weinberg RA, 2009]. The process produces multipotent stromal cells with high invasive potential. Moreover, at this stage cells exhibit a reprogrammed metabolism of glucose, glutamine and fat acids, as well as an altered mitochondrial function, which allow them to survive and proliferate even under stress conditions and starvation [Sivridis E *et al*., 2005].

1.1.7 Chronic Lymphocytic Leukemia

Among all cancer types, Chronic Lymphocytic Leukemia (CLL) is one of the most diffusible and dynamic, characterized by an overproduction of mature monoclonal B lymphocytes. The disease affects about 4-6 over 100,000 people per year, with a five-year survival rate of approximately 83% [Jemal A *et al*., 2007]. Throughout the course of CLL, due to their high number, leukemic B cells progressively accumulate in the bone marrow and in both the blood and lymphatic systems [Davids MS and Burger JA, 2012]. Those cells continuously traffic between peripheral blood and lymph nodes creating spread niches where they interact with the microenvironment that support their survival and proliferation activities [Hacken ET *et al.*, 2013]. Since the process is highly dynamic, B cells are subjected to frequent migrations that require a constant cytoskeletal remodeling in order to migrate from a compartment to another [Scielzo C *et al.*, 2010].

Currently, diagnosis of the disease is mainly based on blood count, blood smear and immunophenotyping. Conversely, in the last few years, CLL treatment has come a long way resulting in the development of new therapeutic approaches that have drastically improved patient outcomes. Among them, new targeted therapies (i.e. PI3K and BCL2 inhibitors) [Freise K *et al.*, 2017; Schiattone L *et al.*, 2019] are taking over on chemoimmunotherapy. More than others, ibrutinib, a selective and irreversible inhibitor of the Bruton's Tyrosine Kinase (BTK), has shown to be more effective compared to other small molecules [Deeks ED, 2017].

1.1.8 BTK signaling

BTK is upstream the B Cell Receptor (BCR) signalling, where it plays a crucial role in the B cell development as well as in the activation of several cell survival pathways such as Akt [Craxton A *et al.*, 1999], Extracellular signal-Regulated Kinase (ERK) [Tomlinson MG *et al.*, 2001] and Nuclear Factor k light-chain enhancer of activated B cells (NF-kB) [Petro JB and Khan WN, 2001] (figure 3). BTK is also involved in the B cell chemokine-mediated homing and adhesion processes [Spaargaren M *et al.*, 2003]. Because of its pivotal role in the survival and differentiation of B cells, the inhibition of BTK is known to induce apoptosis in CLL cells [Khan WN, 2001].

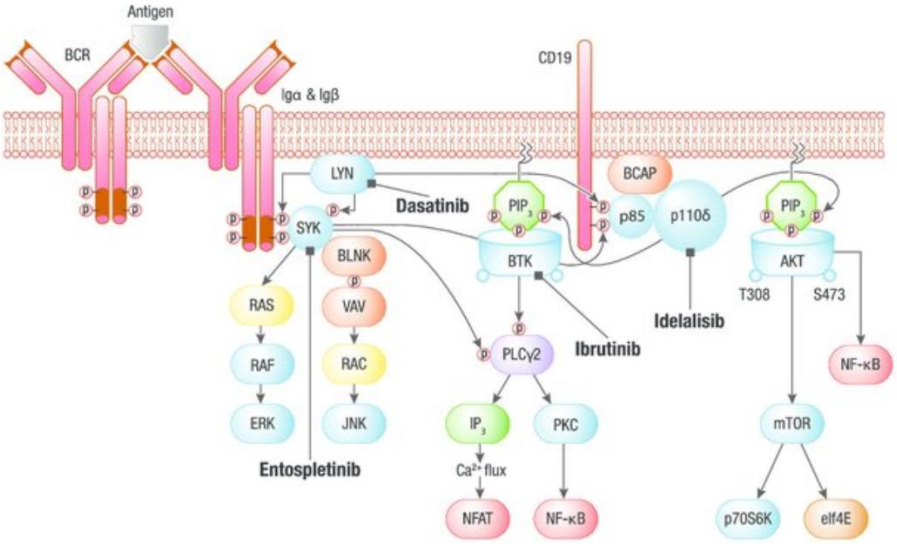

Figure 3. Schematic representation of the BCR signaling pathway reporting the targets of the most used drugs for B cell malignancy treatment [image taken from Sharman J and Di Paolo J, 2016].

1.1.9 BTK inhibitors

The fundamental role of BTK in the BCR signaling pathway has aroused the interest of many researchers as a target for the treatment of B cell disorders. To date, only few drugs have successfully inhibited the signaling and passed the clinical trials. From a clinical point of view, the most promising among those is ibrutinib (Imbruvica), a small organic molecule containing two benzene rings linked to each other through an ether group and, thus, belonging to the class of diphenylethers (figure 4). It was approved in 2014 by the US Food and Drug Administration (FDA) as a monotherapy for the treatment of a variety of B cell malignancies [Novero A *et al*., 2014] such as relapsed and

refractory Mantle Cell Lymphoma (MCL), Waldenstrom's Macroglobulinemia (WM) and CLL [Advani RH *et al*., 2013; Wang ML *et al*., 2013; Byrd JC *et al*., 2013].

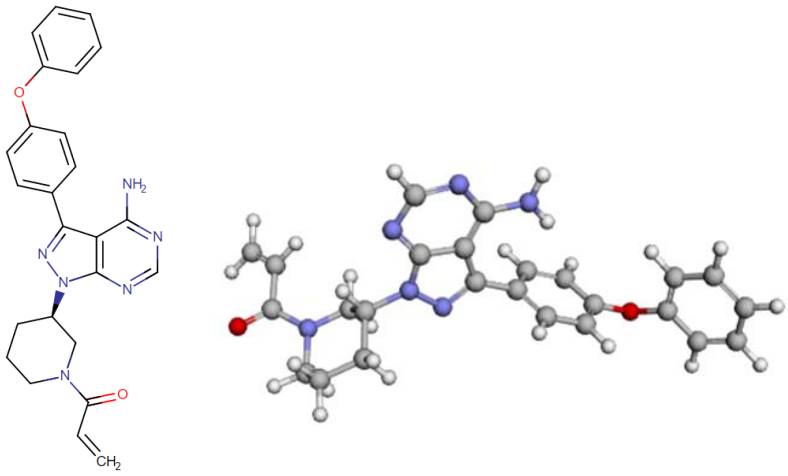

Figure 4. Ibrutinib chemical and 3-dimensional structures.

In particular, ibrutinib forms a covalent bond with BTK cysteine 481 resulting in an inactive adduct that irreversibly blocks the BCR signaling and thus promotes apoptosis [Roskoski R, 2016]. In addition, the ibrutinib inhibitory effect promotes the leukemic B cell mobilization from the tissues to the peripheral blood. Here, the cells lose the protective effect exerted by the tissue microenvironment thus enhancing the probability of apoptosis [Herman SEM *et al*., 2011]. However, the effect of ibrutinib on the properties of B lymphocytes still needs to be fully elucidated, especially from a mechanical point of

view, along with the acquisition of resistance and relapse of this drug displayed by some patients [Burger JA and Wiestner A, 2018].

1.2 Physics of cancer

1.2.1 Cells in motion

Beyond the chemical signaling that triggers the onset and progression of cancer, each cell involved in the processes undergoes many physical contacts with other cells and with the surrounding microenvironment. This holds in particular for the processes involved in the malignant progression. As a matter of fact, the metastasis is a long and complex multistep process involving a huge number of different physical interactions. Cells detach from the primary tumor mass, quitting their original niche, and penetrate the surrounding tissue until the nearest blood vessel, where they intravasate. After floating into the bloodstream, some of these cells eventually adhere to a blood vessel wall and manage to extravasate. After reaching a new site, cells can migrate in the local tissues, where they can finally form a new tumor mass [Wirtz D *et al.*, 2011].

From a mechanical point of view, a migration between two compartments with different densities (i.e. the blood and the vessel walls) requires profound changes in the cytoskeleton and, consequently, in the overall rigidity of the migrating cell (figure 5) [Burdick MM *et al.*, 2012; Gimbrone MA *et al.*, 1999].

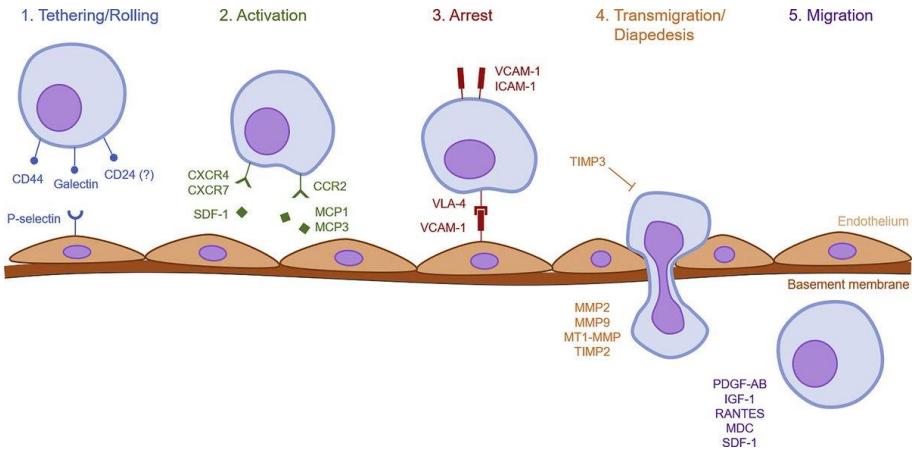

Figure 5. Schematic representation of the homing process of a healthy B lymphocyte migrating from the bloodstream through a vessel. The sketch illustrates how the shape and accordingly the stiffness of the cell change along the path, suggesting a continuously remodeling of its cytoskeleton [image taken from Ullah M *et al.*, 2019].

1.2.2 Moving from the inside

The cytoplasm is a complex system that behaves differently depending on the deformation rate. At high deformation rates, it reacts as an elastic material (e.g. rubber), while at low deformation rates it behaves like a viscous material (e.g. ketchup) [Wirtz D, 2009]. Such features lend different properties to the cell: the elasticity reflects the ability to rebound following the application of a force, while the viscosity allows to sustain flow under external shear [Wirtz D, 2009]. Besides these characteristics, the cytoplasm is responsible also for the numerous phenotypical transformations occurring during the cancer progression. Indeed, the detachment from the primary tumor mass requires the activation of the EMT process during which the cell undergoes morphological changes (from cuboidal epithelial to

mesenchymal shape) and acquires a motile phenotype [Polyak K and Weinbenrg RA, 2009]. In addition, the travel of the cell across a three-dimensional space requires its polarization (usually achieved through the formation of clustered multiple filopodia protrusions) and a constant physical contact with the surrounding environment through the formation of various structures such as focal adhesions, stress fibers, lamella and wide lamellipodia [Sabeh F *et al.*, 2009; Fraley SI *et al.*, 2010]. All those assets result in two primary movements: pushing and pulling. By combining them through a complex mechanocoupling response, cells can adapt their shape and actively migrate [Van Helvert S *et al.*, 2018]. Both basic movements are mediated by the actin cytoskeleton. On one hand, the polymerization of actin filaments, which is under the control of Rho GTPases, allows to protrude the membrane and consequently to achieve the pushing asset [Ridley AJ, 2006]. On the other hand, Rho-associated protein kinases enhance the myosin motors that crosslink, bundle and contract the actin filaments, transmitting force to the substrate [Elosegui-Artola A *et al.*, 2016]. Such transmission takes place at the adhesion sites, where the integrin adhesion receptors on the membrane produce molecular bridges predominantly made of talin and vinculin [Case LB and Waterman CM, 2015]. The bridges form transient connections with the extracellular integrins working as a molecular clutch that translates retrograde actin flow into traction force towards the substrate [Mitchison T and Kirschner M, 1988].

1.2.3 Pressure modification

If we consider the cell as a single physical solid object, any intracellular activity can be observed from the outside as an intra- or extra-flexion of the cell membrane. Such movements are driven by the cytoskeletal polymerization flow, that produces a change in the internal hydrostatic pressure of the cell, resulting in a membrane deformation and relative increased or decreased tension [Houk AR *et al*., 2012]. The local membrane tension also depends on the net amount of the available membrane in a specific area. It follows that any movement (e.g. extension-retraction cycle) of the cell causes and depends on the membrane tension [Mueller J *et al.*, 2017]. Thus, the internal hydrostatic pressure is an important tool for driving cell movements and migration. The cell can sense the internal hydrostatic pressure through mechanosensitive channels and can modify it on a wide range, from 20-100 Pa during the static phase until 400-450 Pa during cytokinesis [Fisher-Friedrich E *et al.*, 2014].

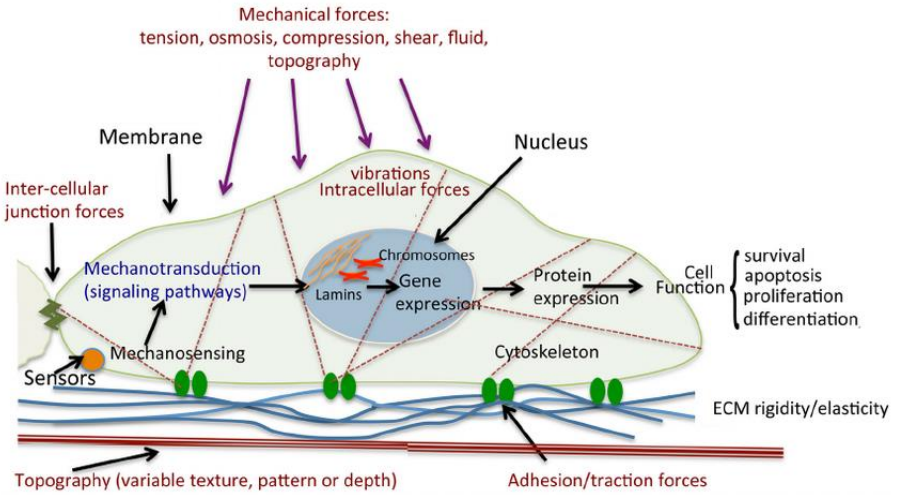

Figure 6. Schematic representation of the cellular mechanisms and forces involved in the process of mechanotransduction [image taken from Tsimbouri PM, 2015].

The modification of the internal pressure is strictly localized in the cell. On one hand, the increased pressure in a particular cytoplasmic region pushes the near plasma membrane outward, facilitating the formation of protrusions. On the other hand, it produces a depression in the adjacent regions, resulting in a reduced stiffness of the area surrounding the protrusion [Stroka KM *et al.*, 2014]. The global rigidity of the cell is thereby uneven and, above all, in constant change (figure 6).

All the processes described so far need to be coordinated in order to produce an effective movement in a specific direction.

1.2.4 Mechanoreciprocity

Along with the intracellular mechanisms that modifies the shape of the cell, the external stroma also contributes to produce forces that drive the growth and progression of the tumor. Thanks to the receptors dedicated to the detection of the external environment, the membrane acts as an interplay between the cytoskeletal dynamics and the substrates that the cell interacts with. The information from the environment are thereby integrated with the possible self-movements to produce an effective and coordinated displacement [Lee J *et al.*, 1999].

In a broader context, the physical interactions that drive the entire process of cancer arise from a constant interplay between internal and external forces [Kumar S and Weaver VM, 2009]. It follows that both the cell and the environment should be "aware" of what is around them. In other words, both the cell and the stroma that surrounds it need to "sense" each other and to respond to a wide variety of stimuli that ultimately favor the cancer growth. This bi-directional relationship of cell-tissue interactions is known as *mechanoreciprocity* and represents a cornerstone for the development of cancer [Van Helvert S *et al.*, 2018]. During this adaptive process, both participants (the cell and the extracellular matrix) modify each other and respond to mutual changes. During the movement, the cell pushes the extracellular matrix favoring its compression and densification. The hardening of the external matrix is felt as an obstacle from the cellular receptors, that, in turn, promote the relaxation of the protrusion. The

resulting release of the pressure exerted on the extracellular matrix favors a viscoelastic relaxation of the substrate [Storm C *et al.*, 2005]. This is a cyclic process in which the cell continuously modifies its behavior in response to the organization and elastic properties of the environment [Paszek MJ and Weaver VM, 2004].

1.2.5 Mechanoreciprocity in cancer

Mechanoreciprocity plays a pivotal role in each dynamic process of the cells. It is therefore reasonable to assume its relevance in the context of cancer, in particular for the processes of invasion and metastasis. Indeed, a migrating cell stiffens the extracellular matrix that surrounds it, both physically [Stroka KM *et al.*, 2014] and biochemically [Odenthal J *et al.*, 2016]. In turn, the stiffening of the stromal matrix and the increase of the degree of orientation of matrix fibers near a primary tumor are sufficient, alone, to greatly enhance cell proliferation and motility [Levental KR *et al.*, 2009; Provenzano PP *et al.*, 2008]. In addition, a stiff matrix enhances the differentiation, plasticity and mobilization of cancer cells, thus favoring single cell dissemination [Odenthal J *et al.*, 2016].

Along with the regulation of migration and tissue remodeling, also other intracellular activities are affected by mechanical stimuli, as it has been demonstrated for metabolism, gene transcription and cell differentiation [Miroshnikova YA *et al.*, 2017]. Such hypothesis paves the way to the idea of a wide cooperation between

mechanoreciprocity processes and other primary functions that could lead to a more complex scenario, where mechanical stresses activate generalized responses including gene transcription and cell cycle adaptation [Mendez MG and Janmey PA, 2012; Meyer CJ *et al.*, 2000].

1.2.6 The stiffness in cellular biophysics

The rigidity of cells depends, as discussed above, on a complex network of intracellular pathways, and on cell-cell and cell-microenvironment interactions. In this vein, an increasing number of findings in the field of cancer mechanics reported a nearly ubiquitous trend: on one side, the stiffening of the extracellular matrix surrounding a tumor [Levental KR *et al.*, 2009; Provenzano PP *et al.*, 2008], on the other, the softening process of the cancer cells [Anderson KW *et al.*, 1991; Cross SE *et al.*, 2007]. Such features have been demonstrated both *in vitro* and *in vivo* [Swaminathan V *et al.*, 2011]. Furthermore, the degree of the stiffening reduction in cancer cells has been correlated to an increase in the malignant potential [Ward KA *et al.*, 1991]. More recently, research in this field has found reasonable explanations to this phenomenon. In fact, a reduced stiffness can promote cell survival [Sun Q *et al.*, 2014] ensuring an evolutive advantage on the surrounding cells [Szabò A and Merks RMH, 2013]. In addition, a soft phenotype strongly facilitates migrations during metastasis [Xu W *et al.*, 2012].

The stiffness is a physical parameter that quantifies the resistance to the deformation of a solid material in response to an applied force and it is expressed as a pressure. Nevertheless, when applied to Biology, it becomes a much more complicated parameter. Indeed, a cell is a complex object in which several different compartments with different physical properties contribute to define its stiffness. Consequently, the calculation of the stiffness of a cell requires the introduction of a different parameter, the elasticity or the elastic modulus. Depending on the direction of the applied force and on the stress measurement method, different moduli can be distinguished. The most used in biology is the Young's Modulus (YM), which is defined as the tensile stress/tensile strain ratio and calculated in Pascal (Pa). As a measure of the resistance to deformation, it follows that the higher the YM of an object, the lower its elasticity, and vice versa.

1.3 Nanomechanics

1.3.1 Origins, history and achievements of nanomechanics

Nanomechanics is a branch of the wide nanotechnology field that encompasses several areas such as biophysics and solid-state physics, classical and statistical mechanics, classical and molecular biology, and material science at the nanoscale.

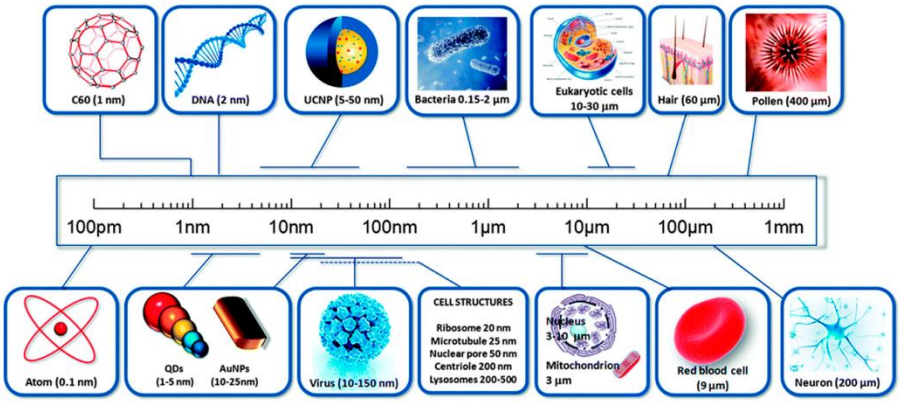

Figure 7. Schematic representation of the size scale under the investigation of nanotechnology [image taken from Gnach A *et al.*, 2015].

The roots of nanotechnology date back to 1959, with the talk of the physicist Richard Feynman *"There's plenty of room at the bottom"*, even if the word "nano-technology" was first coined by Norio Toniguchi in 1974. Then, nanotechnology became an independent field only in the 1980s, with the invention of the scanning tunneling microscope, that allowed an unprecedented visualization of single atoms and bonds. As its name suggests, the purpose of

nanotechnology is to manipulate matter at atomic, molecular and supramolecular scales (figure 7) looking for potential applications in many different areas, ranging from medicine to pharmaceutical, materials, agriculture, and food safety. Nowadays, nanotechnology numbers many branches which may also differ widely [Meyer M and Persson O, 1998; Dasgupta N *et al.*, 2015; Krishnaa VD *et al*., 2018].

One of these branches is nanomechanics, whose purpose is to explore the mechanical properties of materials and biological systems at the single molecule level in order to better understand their functioning with potential applications in health, pharmacological and biomedical sectors, among many others. To date, nanomechanics played an important role in unravelling and manipulating biological systems such as cells, tissues, proteins, nucleic acids and molecular motors, paving the way for deeper knowledge and superior technologies for healthcare [Liu WK *et al.*, 2006; Nautiyal P *et al*., 2018; Craighead HG, 2000].

1.3.2 Nanomechanical techniques

As a science focused on nanoscale, nanomechanics requires highly accurate instruments capable of observing and measuring variations of few nanometers. Classical bulk techniques measure millions of cells or even billions of molecules, returning an average value that may hide rare or secondary features of a small and peculiar subpopulation. On the other hand, the remarkable precision of nanomechanical

techniques allows focusing on single objects, characterizing their features and behavior. This approach is very useful, for instance, to observe the physical modification of a specific cell induced by a stimulus, or to track a particular conformation that a molecule assumes in a reduced percentage of cases.

Nowadays there are few available instruments for nanomechanical research, namely nanoindentation and nanotribology sensors, Atomic Force Microscopy (AFM), Optical Tweezers (OT) and other hybrid techniques. However, many of them are adaptable to different purposes [Nautiyal P *et al.*, 2018].

1.3.3 Magnetic Tweezers

The Magnetic Tweezers (MT) technique was born in the 1950s with the idea of manipulating cells that had phagocytized tiny magnetic particles using a magnetic field [Crick FHC and Hughes AFW, 1950]. A step forward was made in the 1990s, by modifying an optical tweezers setup and by chemically linking a single DNA molecule to a surface (a glass slide) on one side, and to a magnetic bead on the other. A couple of magnets is used to modify the force exerted on the molecule by moving them on the z axis, and to apply a torque by rotating them (figure 8). An inverted microscope coupled with a CCD camera allows a real-time tracking of the bead [Vilfan ID *et al.*, 2009].

The high precision of the instrument in measuring the DNA and protein extension is achieved by using a parallel light (superlumen) that

illuminates the beads, producing concentric diffraction rings whose pattern changes depending on the bead vertical position. The camera collects the images of the bead and a software compares them with a library of images obtained from the reference beads, attached on the substrate. It is thereby possible to extract the distance between the bead and the substrate and consequently the molecule extension. In particular, this configuration allows to measure the DNA vertical extension (L_0) as a function of the applied force (F) with an accuracy of approximately 10 nm in the z axis [Gosse C and Croquette V, 2002].

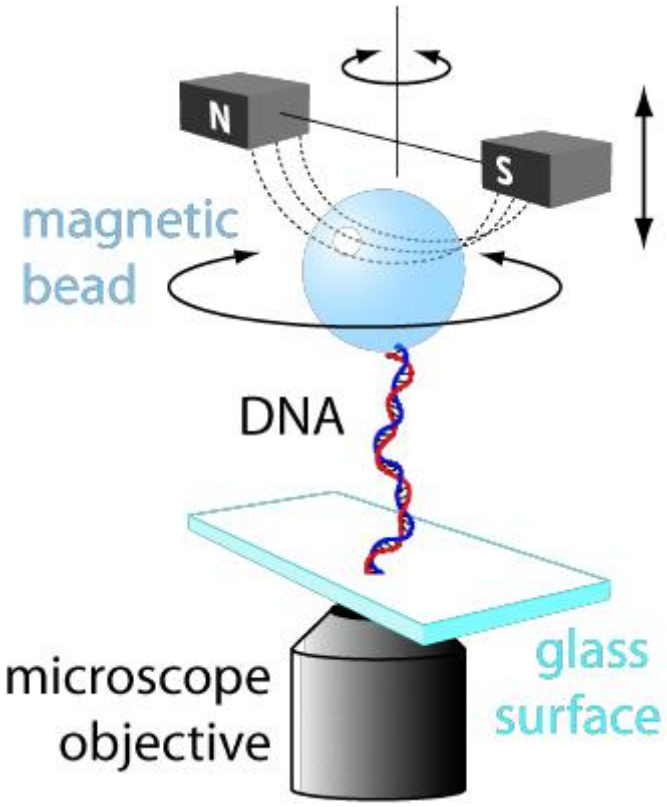

Figure 8. Schematic representation of the Magnetic Tweezers setup. A DNA molecule is covalently bound to a glass surface on one hand, and to a micron-sized magnetic bead on the other. A couple of permanent magnets can be moved up and down, in

order to pull the DNA, and can rotate, in order to uncoil or supercoil the molecule. An inverted microscope at the bottom of the glass tracks the movements of the bead [image taken from Manosas M *et al.*, 2010].

To date, MT has been applied in surprisingly diverse biological applications. The capability of moving and tracking solid particles within a cell makes it a valuable tool to study cellular properties such as rheology and cytoplasm rearrangement [Tanase M *et al.*, 2007]. The application of force and torque to a DNA or RNA filament (both single- and double-stranded) allows to study their mechanical properties [Fabian R *et al.*, 2018]. Nucleic acids *in vivo* perform different functions depending on their structure. By way of example, while dsDNA is responsible for the storage of genetic information, ssDNA represents an intermediate in biological processes such as replication and transcription. The rotation of the magnets allows to uncoil the molecule producing a denaturation bubble that enables to study its function at a single molecule level. Moreover, thanks to the mechanical denaturation it is possible to observe the self-interaction of nucleic acids such as alternative forms to the double helix (e.g. hairpins, G4s and holliday junctions), or their interaction with proteins (e.g. topoisomerases and histones). Even single proteins can be fixed to a magnetic bead and pulled in order to study their structural properties and their interactions. Finally, MT is dealing with the promising field of the so-called single-complex study: using the DNA as a tether, it is possible to set up a complex system consisting of different active domains of proteins separated by a strand of nucleic acid on the

same macro complex. This strategy allows to observe the behavior of the proteins, thus unravelling the mechanics of their interaction and their reciprocal affinity [Sarkar R and Rybenkov VV, 2016].

1.3.4 Atomic Force Microscopy

Among nanomechanical techniques, AFM is the most adaptable and versatile one. The first version, called Scanning Tunneling Microscope (STM), dates back to the early 80s, ensuring the Nobel Prize for physics to its inventors. Few years later STM was implemented to AFM, which was first marketed in 1989.

AFM consists of a flexible cantilever that ends with a nanometric probe which is brought in contact to the sample. Any force acting on the probe leads to a deflection of the cantilever, which is recorded by a laser focused on the cantilever and reflected on a photodetector (figure 9).

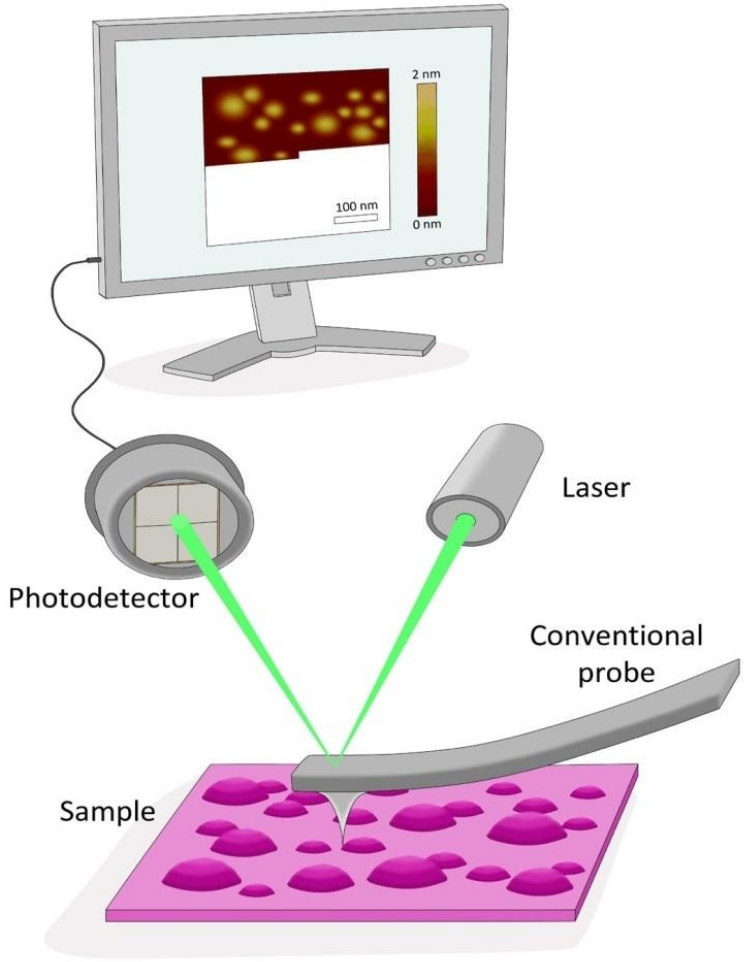

Figure 9. Schematic representation of the AFM setup. The probe scans the sample producing a three-dimensional image (topography) of the surface of the sample [image adapted from Frewin C, 2012].

AFM was initially conceived as a topographic imaging tool able to scan samples producing three-dimensional maps with a vertical precision of less than 1 nm. The instrument has three different operation modes depending on the nature of the tip movement, i.e. contact mode, tapping mode and non-contact mode. The first mode, as its name

suggests, is based on the sliding of the tip on the sample, so it requires a direct contact between the probe and the sample [Binnig G *et al.*, 1986]. The tapping mode, instead, is based on the oscillation of the cantilever around its resonance frequency. When close to a surface, several secondary forces (e.g. dipole-dipole interactions, Van der Waals forces, etc.) interfere with the cantilever's oscillation changing its amplitude, which is recorded by the instrument and processed to produce a detailed image [Zhong Q *et al.*, 1993]. Similarly, the non-contact mode is based on the change in the amplitude of the cantilever frequency when approaching the sample, but without getting in contact with it [Gross L *et al.*, 2009].

In contrast to electron microscopes, AFM works both in air and in liquid, and the sample does not require any particular treatment that could affect its integrity. Moreover, the tip can be easily replaced, choosing between a broad variety of shapes and sizes. Those features allow to extend the operativity of AFM to a wide variety of applications. One of the main, beside imaging, is the force spectroscopy mode. In this configuration, the tip is vertically brought in contact with the sample. During the retraction of the tip, the instrument can measure the interactions between the tip and the sample. Force spectroscopy mode has several applications in biology, allowing to measure the mechanical properties of macromolecules (e.g. mechanical unfolding of proteins, protein-protein and ligand-receptor interactions, etc.), of cells and tissues [Krieg M *et al.*, 2018]. In particular, the force spectroscopy mode allows performing

nanoindentation experiments on living cells, measuring their elasticity via the Hertz model [Carl P and Schillers H, 2008; Sirghi L *et al.*, 2008]. This model represents a powerful tool to assess the elasticity of biological structures by using the YM [Radmacher M, 2007] and it shows a wide potential in the biomedical field, in particular when applied to the research in cancer. An increasing number of studies is actually focusing on the peculiar mechanical signature of cancer cells, which seems to indicate an overall reduction of the cancerous cellular stiffness [Cross SE *et al.*, 2007]. In this context, AFM represents a valid and powerful tool to characterize the mechanical feature of cancer [Neuman K *et al.*, 2008].

1.3.5 Real-time deformability cytometry

Real-Time Deformability Cytometry (RT-DC) is a novel high-throughput method for the mechanical characterization of single cells. It works as a classical flow cytometry, flowing one cell at a time within a narrow channel. In this case, the laser beam is replaced by a fast camera that acquires a real-time image of each cell. After a few milliseconds, the pressure exerted by the constant flow rate through the channel deforms the cell up to a steady state (figure 10) [Herbig M *et al.*, 2018]. Then, a dedicated software identifies the contours of every cell evaluating the degree of its hydrodynamic deformation. For each cell, several nanomechanical parameters can be extracted and gated for the derivation of material properties [Mokbel M *et al.*, 2017].

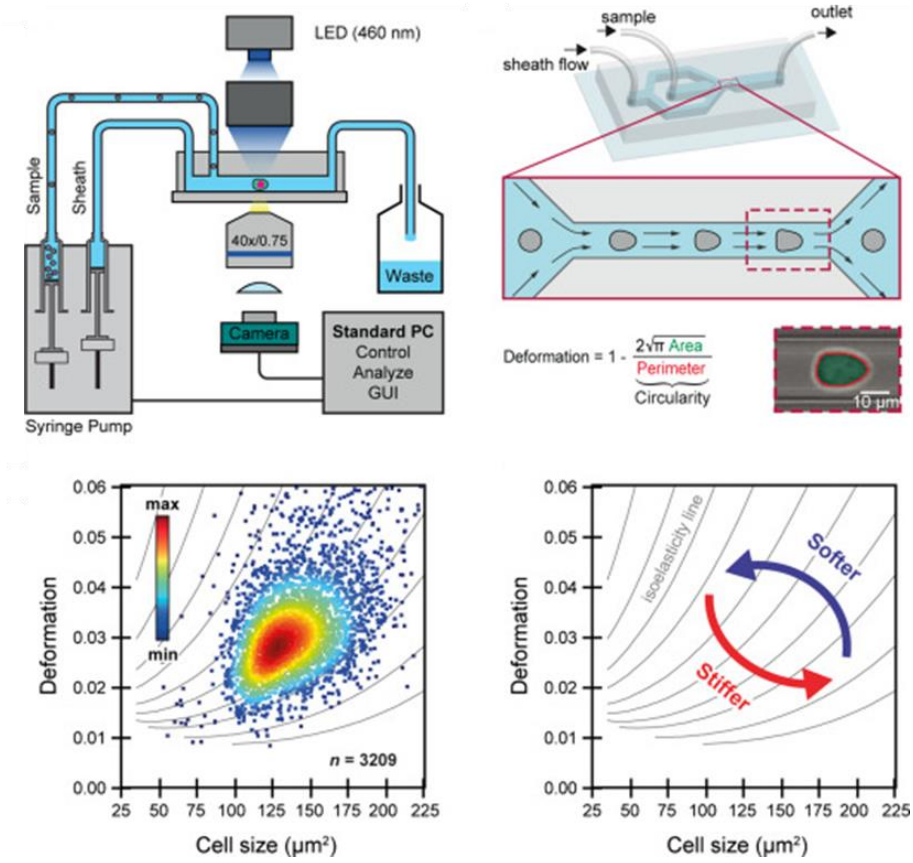

Figure 10. Schematic representation of the RT-DC setup. A flow of single cells passes through a microfluidic channel under a constant flow rate, and the deformation is recorded at the end of the channel. Data may be plotted and gated based on many variables [image taken from Herbig M *et al.*, 2018].

Recently, real-time deformability cytometry has been coupled with fluorescence detection (RT-FDC) allowing to simultaneously gather information on mechanical properties and fluorescence intensity of single cells [Rosendahl P *et al.*, 2018].

RT-DC has many relevant applications in the biomedical field, in particular for the characterization of blood cells. In fact, the

instrument can process a whole blood sample in a few seconds clearly distinguishing each subpopulation and measuring their mechanical properties.

1.3.6 Nanomechanical application in cancer research

One of the most promising aspects of nanomechanics is represented by the possibility of mechanically phenotyping single cells. Such potential allows to study in detail the contribution of mechanical stimuli in a broad variety of diseases, and in particular for cancer. Recently, the relation between the metastatic potential of cancer cells and their mechanical compliances has been outlined as a promising prognostic marker [Park S, 2016]. Nanomechanics has therefore laid the foundation of new targeted strategies in the fight against cancer.

All the aforementioned instruments allow investigating different aspects of the mechanical properties of single cells. However, if RT-DC is specifically conceived for the study of cells, AFM and MT can also deal with smaller objects, as in the case of cellular compartments, proteins and nucleic acids. The structural characterization of such elements favors the insight of their functioning and interactions. Moreover, the ability to manipulate matter at a micro- or even nanoscale enables the observation of biological systems such as protein-protein [Casuso I *et al.*, 2010; Bonazza K *et al.*, 2014] or DNA-protein interactions [Heller I *et al.*, 2014]. In concrete terms, the nanomechanical tools provide the ability to observe if a particular drug

increases or decreases the affinity of a ligand-receptor complex, or to monitor whether a small molecule interferes with the transcriptional activity of a polymerase complex. Such information can support the production of new therapies, especially the targeted ones, improving the knowledge of their mechanism of action.

1.4 Scope of the thesis

Cancer is an extremely complex, diverse and dynamic disease and it represents a major health issue worldwide. Due to its heterogeneity and complexity, many critical aspects of oncogenesis, from cancer onset to metastatization, are still poorly understood, and in some cases even completely unknown. The structural modification of cellular architecture and the misregulation of gene expression, which are strictly connected to these processes, represent key features to deepen the knowledge of cancer. In this context, the field of nanomechanics provides a significant two-pronged contribution. Indeed, it represents one of the few tools we can use (i) to analyze the structural contribution of DNA secondary structures in the misregulation of oncogene expression, and (ii) to investigate the complex mechanisms that drive the movements of the cell and their interactions with the microenvironment.

The *c-KIT* proto-oncogene has a strategic role in regulating the replication rate of many cell types, and therefore is crucial in the onset of several types of cancer (mastocytosis, gastrointestinal stromal tumors, lung cancer and some types of leukemia). As for many genes, its regulation is mainly controlled by its proximal promoter. The regulatory mechanisms of the *c-KIT* promoter seem to be related to the formation of three G4s present along its sequence. Anyway, the contribution of these three non-canonical DNA secondary structures to the regulation of the proto-oncogene expression still needs to be elucidated. One of the major problems in the study of G4s is that their

formation requires the opening of the DNA double strand, an event that is compulsorily investigated in non-physiological conditions (i.e. high temperature or low pH) by classical bulk techniques. Moreover, their probabilistic nature makes the detection of G4s formation almost impossible without exploiting SM-techniques. The MT allows the mechanical denaturation of single molecules of dsDNA in controlled conditions of pH, temperature and ionic strength, a peculiarity that elects this SM-technique as one of the most powerful tools to study the mechanical properties of DNA secondary structures. The work presented in Chapter 2 aims specifically to characterize the mechanical properties of the *c-KIT* promoter with a particular focus on the folding of the G4s. This is a first step to elucidate the contribution of G4s in the regulation of the proto-oncogene *c-KIT*.

Metastasis is responsible for the greatest number of cancer-related deaths, thus representing the most studied and the less known phase of cancer. This phenomenon is caused by at least one travelling cell that is continuously subjected to physical contacts with the extracellular matrix and with neighbour cells. Those interactions will ultimately determine the faith of the metastatic cell and the course of its travel. Within the framework of CLL, both leukemic and healthy cells have native dynamic properties, and are subjected to frequent migrations. However, if healthy B lymphocytes have to keep moving between the blood and the lymph nodes, migration of leukemic cells can lead to the formation of metastasis. The administration of BTK inhibitors (e.g. ibrutinib) mobilizes leukemic cells settled in the tissues

without affecting the migratory pattern of healthy lymphocytes. This effect induces a mechanical remodeling which is still poorly known. Once again, SM-techniques allow exerting different kind of mechanical stimuli on single cells, thus enabling to measure their response in a wide variety of conditions. AFM can measure the resistance of a still cell to the pressure in a point-shaped area, while RT-DC can calculate the resistance of suspended cells to a hydrodynamic pressure that deforms the whole area. Both techniques provide an accurate measure of the mechanical properties of single cells in conditions similar to those that occur in CLL: a cell floating in the bloodstream or a migrating cell through a solid tissue. The work presented in Chapter 3 aims (i) to observe the mechanical properties of malignant B cells isolated from CLL patients in comparison with healthy B lymphocytes, (ii) to evaluate the *in vitro* effect of the BTK inhibitor ibrutinib treatment on the rigidity of CLL and healthy cells, and (iii) to monitor the trend of this parameter on cells isolated from CLL patients under treatment at different time points.

1.5 Bibliography

- Hanahan D and Weinberg RA. Hallmarks of cancer: the next generation. *Cell*. **2011**, 144, 646-74.
- Haidong W, Naghavi M, Allen C, Barber RM, Bhutta ZA, Carter A, *et al*. Global, regional, and national life expectancy, all-cause mortality, and cause-specific mortality for 249 causes of death, 1980-2015: a systematic analysis for the Global Burden of Disease Study 2015. *Lancet.* **2015**, 388, 1459-1544.
- World Cancer Report 2014. *World Health Organization*. **2014**, 1, 22.
- Hanahan D. and Weinberg RA. The hallmarks of cancer. *Nat. Rev. Mol. Cell. Biol.* **2010**, 11, 220-228.
- Blume-Jensen P, Claesson-Welsh L, Siegbahn A, Zsebo KM, Westermark B, Heldin CH. Activation of the human c-kit product by ligand-induced dimerization mediates circular actin reorganization and chemotaxis. *EMBO J.* **1991**, 10, 4121-4128.
- Liang J, Wu YL, Chen BJ, Zhang W, Tanaka Y, Sugiyama H. The c-kit receptor-mediated signal transduction and tumor-Related Diseases. *Int. J. Biol. Sci.* **2013**, 9, 435-443.
- Zorzan E, Da Ros S, Musetti C, Shahidian LZ, Coelho NF, Bonsembiante F. Screening of candidate G-quadruplex ligands for the human c-KIT promotorial region and their effects in multiple in vitro models. *Oncotarget.* **2016**, 7, 21658-21675.
- Sakurai S, Fukasawa T, Chong JM, Tanaka A, Fukayama M. C-kit gene abnormalities in gastrointestinal stromal tumors (tumors of interstitial cells of Cajal. *J. Cancer Res*. **1999**, 90, 1321-1328.
- Fernando H, Reszka AP, Huppert J, Ladame S, Rankin S, Venkitaraman AR, *et al*. A conserved quadruplex motif located in a transcription activation site of the human c-kit oncogene. *Biochemistry*. **2006**, 45, 7854-7860.
- Kotar A, Rigo R, Sissi C, Plavec J. Two-quartet kit* G-quadruplex is formed via double-stranded pre-folded structure. *Nucleic Acids Res*. **2019**, 47, 2641-2653.
- Rankin S, Reszka AP, Huppert J, Zloh M, Parkinson GN, Todd AK, *et al*. Putative DNA quadruplex formation within the human c-kit oncogene. *J. Am. Chem. Soc*. **2005**, 127, 10584-10589.
- Ceschi S and Sissi C. KIT Promoter: structure, function and targeting. "Quadruplex nucleic acid as targets for medicinal chemistry", *Ed. S. Neidle, Elsevier*. **2020**, online ahead of print.

- Bochman ML, Paeschke K, Zakian VA. DNA secondary structures: stability and function of G-quadruplex structures. *Nat. Rev. Genet.* **2012**, 13, 770-780.
- Lightfoot HL, Hagen T, Tatum NJ, Hall J. The diverse structural landscape of quadruplexes. *FEBS Lett.* **2019**, 593, 2083-2102.
- Bhasikuttan AC and Mohanty J. Targeting G-quadruplex structures with extrinsic fluorogenic dyes: promising fluorescence sensors. *Chem. Commun.* **2015**, 51, 7581-7597.
- Hänsel-Hertsch R, Di Antonio M, Balasubramanian S. DNA G-quadruplexes in the human genome: detection, functions and therapeutic potential. *Nat. Rev. Mol. Cell Biol*. **2017**, 18, 279-284.
- Bhattacharyya D, Mirihana Arachchilage G, Basu S. Metal cations in G-quadruplex folding and stability. *Front. Chem*. **2016**, 4, 38.
- Victorelli S and Passos JF. Telomeres and Cell Senescence - Size Matters Not. *E. Bio. Med*. **2017**, 21, 14-20.
- Du Z, Zhao Y, Li N. Genome-wide analysis reveals regulatory role of G4 DNA in gene transcription. *Genome Res*. **2008**, 18, 233-241.
- Maizels N and Gray LT. The G4 genome. *PLoS Genet.* **2013**, 9, e1003468.
- Yamamoto K, Tojo A, Aoki N, Shibuya M. Characterization of the promoter region of the human c-kit proto-oncogene. *J. Cancer Res.* **1993**, 84, 1136-1144.
- McLuckie KI, Waller ZA, Sanders DA, Alves D, Rodriguez R, Dash J, *et al*. G-quadruplex-binding benzo phenoxazines down-regulate c-KIT expression in human gastric carcinoma cells. *J. Am. Chem. Soc.* **2011**, 133, 2658-2663.
- Raiber EA, Kranaster R, Lam E, Nikan M, Balasubramanian S. A non-canonical DNA structure is a binding motif for the transcription factor SP1 *in vitro*. *Nucleic Acids Res*. **2012**, 40, 1499-1508.
- Rigo R and Sissi C. Characterization of G4-G4 crosstalk in the c-KIT promoter region. *Biochem*. **2017**, 56, 4309-4312.
- Balasubramanian S, Hurley LH, Neidle S. Targeting G-quadruplexes in gene promoters: a novel anticancer strategy? *Nat. Rev. Drug Discov*. **2011**, 10, 261-275.
- Rigo R, Palumbo M, Sissi C. G-quadruplexes in human promoters: A challenge for therapeutic applications. *Biochim. Biophys. Acta. Gen. Subj*. **2017**, 1861, 1399-1413.

- Kalluri R and Weinberg RA. The basics of epithelial-mesenchymal transition. *J. Clin. Invest*. **2009**, 119, 1420-1428.
- Sivridis E, Giatromanolaki A, Koukourakis MI. Proliferating fibroblasts at the invading tumour edge of colorectal adenocarcinomas are associated with endogenous markers of hypoxia, acidity, and oxidative stress. *J. Clin. Pathol.* **2005**, 58, 1033-1038.
- Jemal A, Siegel R, Ward E, Murray T, Xu J, Thun MJ. Cancer statistics. *CA Cancer J. Clin.* **2007**, 57, 43-66.
- Davids MS and Burger JA. Cell trafficking in chronic lymphocytic leukemia. *Open J. Hematol.* **2012**, 3, 3.
- Hacken ET, Scielzo C, Wierda WG, Keating MJ, O'Brien S, Ghia P, *et al*. Ibrutinib differentially interferes with surface IgM and IgD BCR signaling kinetics in chronic lymphocytic leukemia. *Blood* **2013**, 122, 4143.
- Scielzo C, Hacken ET, Bertilaccio MT, Muzio M, Calissano C, Ghia P, *et al*. How the microenvironment shapes chronic lymphocytic leukemia: the cytoskeleton connection. *Leuk. Lymphoma* **2010**, 51, 1371-1374.
- Freise KJ, Jones AK, Eckert D, Mensing S, Wong SL, Humerickhouse RA, *et al*. Impact of venetoclax exposure on clinical efficacy and safety in patients with relapsed or refractory chronic lymphocytic leukemia. *Clin. Pharmacokinet.* **2017**, 56, 515-523.
- Schiattone L, Ghia P, Scarfò L. The evolving treatment landscape of chronic lymphocytic leukemia. *Curr. Opin. Oncol*. **2019**, 31, 568-573.
- Deeks ED. Ibrutinib: a review in Chronic Lymphocytic Leukemia. *Drugs* **2017**, 77, 225-236.
- Craxton A, Jiang A, Kurosaki T, Clark EA. Syk and Bruton's tyrosine kinase are required for B cell antigen receptor-mediated activation of the kinase Akt. *J. Biol. Chem*. **1999**, 274, 30644-30650.
- Tomlinson MG, Woods DB, McMahon M, Wahl MI, Witte ON, Kurosaki T, *et al*. A conditional form of Bruton's tyrosine kinase is sufficient to activate multiple downstream signaling pathways via PLC Gamma 2 in B cells. *BMC Immunol*. **2001**, 2, 4.
- Petro JB and Khan WN. Phospholipase C-gamma 2 couples Bruton's tyrosine kinase to the NF-kappaB signaling pathway in B lymphocytes. *J. Biol. Chem*. **2001**, 276, 1715-1719.

- Spaargaren M, Beuling EA, Rurup ML, Meijer HP, Klok MD, Middendorp S, *et al*. The B Cell Antigen Receptor Controls Integrin Activity through Btk and PLCγ2. *J. Exp. Med.* **2003**, 198, 1539-1550.
- Khan WN. Regulation of B lymphocyte development and activation by Bruton's tyrosine kinase. *Immunol. Res*. **2001**, 23, 147-156.
- Sharman J and Di Paolo J. Targeting B-cell receptor signaling kinases in chronic lymphocytic leukemia: the promise of entospletinib. *Ther. Adv. Hematol.* **2016**, 7, 157-70.
- Novero A, Ravella PM, Chen Y, Dous G, Liu D. Ibrutinib for B cell malignancies. *Exp. Hematol. Oncol*. **2014**, 3, 4.
- Advani RH, Buggy JJ, Sharman JP, Smith SM, Boyd TE, Grant B, *et al*. Bruton tyrosine kinase inhibitor ibrutinib (PCI-32765) has significant activity in patients with relapsed/refractory B-cell malignancies. *J. Clin. Oncol*. **2013**, 31, 88-94.
- Wang ML, Rule S, Martin P, Goy A, Auer R, Kahl BS, *et al*. Targeting BTK with ibrutinib in relapsed or refractory mantle-cell lymphoma. *N. Engl. J. Med.* **2013**, 369, 507-516.
- Byrd JC, Furman RR, Coutre SE, Flinn IW, Burger JA, Blum KA, *et al*. Targeting BTK with Ibrutinib in Relapsed Chronic Lymphocytic Leukemia. *N. Engl. J. Med.* **2013**, 369, 32-42.
- Roskoski R. Ibrutinib inhibition of Bruton protein-tyrosine kinase (BTK) in the treatment of B cell neoplasms. *Pharmacol. Res*. **2016**, 113, 395-408.
- Herman SEM, Gordon AL, Hertlein E, Ramanunni A, Zhang X, Jaglowski S, *et al*. Bruton tyrosine kinase represents a promising therapeutic target for treatment of chronic lymphocytic leukemia and is effectively targeted by PCI-32765. *Blood* **2011**, 117, 6287-6296.
- Burger JA and Wiestner A. Targeting B cell receptor signalling in cancer: preclinical and clinical advances. *Nat. Rev. Cancer*. **2018**, 18, 148-167.
- Wirtz D, Konstantopoulos K, Searson PC. The physics of cancer: the role of physical interactions and mechanical forces in metastasis. *Nat. Rev. Cancer*. **2011**, 11, 512-522.
- Burdick MM, Henson KA, Delgadillo LF, Choi YE, Goetz DJ, Tees DF, *et al*. Expression of E-selectin ligands on circulating tumor cells: cross-regulation with cancer stem cell regulatory pathways? *Front. Oncol.* **2012**, 2, 103.

- Gimbrone MA, Anderson KR, Topper JN. The Critical Role of Mechanical Forces in Blood Vessel Development, Physiology and Pathology. *J. Vasc. Surg.* **1999**, 29, 1104-1151.
- Ullah M, Liu DD, Thakor AS. Mesenchymal stromal cell homing: mechanisms and strategies for improvement. *iScience*. **2019**, 15, 421-438.
- Wirtz D. Particle-tracking microrheology of living cells: principles and applications. *Annu. Rev. Biophys*. **2009**, 38, 301-326.
- Polyak K and Weinberg RA. Transitions between epithelial and mesenchymal states: acquisition of malignant and stem cell traits. *Nat. Rev. Cancer*. **2009**, 9, 265-273.
- Sabeh F, Shimizu-Hirota R, Weiss SJ. Protease-dependent versus -independent cancer cell invasion programs: three-dimensional amoeboid movement revisited. *J. Cell. Biol*. **2009**, 185, 11-19.
- Fraley SI, Feng Y, Krishnamurthy R, Kim DH, Celedon A, Longmore GD, Wirtz D. A distinctive role for focal adhesion proteins in three-dimensional cell motility. *Nat. Cell. Biol*. **2010**, 12, 598-604.
- Van Helvert S, Storm C, Friedl P. Mechanoreciprocity in cell migration. *Nat. Cell. Biol*. **2018**, 20, 8-20.
- Ridley AJ. Rho GTPases and actin dynamics in membrane protrusions and vesicle trafficking. *Trends Cell Biol*. **2006**, 16, 522-529.
- Elosegui-Artola A, Oria R, Chen Y, Kosmalska A, Pérez-González C, Castro N, *et al*. Mechanical regulation of a molecular clutch defines force transmission and transduction in response to matrix rigidity. *Nat. Cell. Biol*. **2016**, 18, 540-548.
- Case LB and Waterman CM. Integration of actin dynamics and cell adhesion by a three-dimensional, mechanosensitive molecular clutch. *Nat. Cell Biol*. **2015**, 17, 955-963.
- Mitchison T and Kirschner M. Cytoskeletal dynamics and nerve growth. *Neuron*. **1988**, 1, 761-772.
- Houk AR, Jilkine A, Mejean CO, Boltyanskiy R, Dufresne ER, Angenent SB, *et al*. Membrane tension maintains cell polarity by confining signals to the leading edge during neutrophil migration. *Cell*. **2012**, 148, 175-188.
- Mueller J, Szep G, Nemethova M, de Vries I, Lieber AD, Winkler C, *et al*. Load Adaptation of Lamellipodial Actin Networks. *Cell*. **2017**, 171, 188-200.

- Fischer-Friedrich E, Hyman AA, Jülicher F, Müller DJ, Helenius J. Quantification of surface tension and internal pressure generated by single mitotic cells. *Sci. Rep*. **2014**, 4, 6213.
- Tsimbouri PM. Adult stem cell responses to nanostimuli. *J Funct Biomater.* **2015**, 6, 598-622.
- Stroka KM, Jiang H, Chen SH, Tong Z, Wirtz D, Sun SX, Konstantopoulos K. Water permeation drives tumor cell migration in confined microenvironments. *Cell*. **2014**, 157, 611-623.
- Lee J, Ishihara A, Oxford G, Johnson B, Jacobson K. Regulation of cell movement is mediated by stretch-activated calcium channels. *Nature*. **1999**, 400, 382-386.
- Kumar S and Weaver VM. Mechanics, malignancy, and metastasis: the force journey of a tumor cell. *Cancer Metast. Rev*. **2009**, 28, 113-127.
- Storm C, Pastore JJ, MacKintosh FC, Lubensky TC, Janmey PA. Nonlinear elasticity in biological gels. *Nature.* **2005**, 435, 191-194.
- Paszek MJ and Weaver VM. The tension mounts: mechanics meets morphogenesis and malignancy. *J. Mamm. Gland Biol. Neoplasia*. **2004**, 9, 325-342.
- Odenthal J, Takes R, Friedl P. Plasticity of tumor cell invasion: governance by growth factors and cytokines. *Carcinogenesis*. **2016**, 37, 1117-1128.
- Levental KR, Yu H, Kass L, Lakins JN, Egeblad M, Erler JT *et al*. Matrix crosslinking forces tumor progression by enhancing integrin signaling. *Cell*. **2009**, 139, 891-906.
- Provenzano PP, Inman DR, Eliceiri KW, Trier SM, Keely PJ. Contact guidance mediated three-dimensional cell migration is regulated by Rho/ROCK dependent matrix reorganization. *Biophys. J*. **2008**, 95, 5374-5384.
- Miroshnikova YA, Nava MM, Wickstrom SA. Emerging roles of mechanical forces in chromatin regulation. *J. Cell Sci*. **2017**, 130, 2243-2250.
- Mendez MG and Janmey PA. Transcription factor regulation by mechanical stress. *J. Biochem. Cell Biol*. **2012**, 44, 728-732.
- Meyer CJ, Alenghat FJ, Rim P, Fong, Fabry B, Ingber DE. Mechanical control of cyclic AMP signalling and gene transcription through integrins. *Nat. Cell Biol*. **2000**, 2, 666-668.

- Anderson K, Li WI, Cezeaux J, Zimmer S. In vitro studies of deformation and adhesion properties of transformed cells. *Cell Biophys*. **1991**, 18, 81-97.
- Cross S, Jin Y, Rao J, Gimzewski JK. Nanomechanical analysis of cells from cancer patients. *Nature Nanotech*. **2007**, 2, 780-783.
- Swaminathan V, Mythreye K, O'Brien ET, Berchuck A, Blobe GC, Superfine R. Mechanical stiffness grades metastatic potential in patient tumor cells and in cancer cell lines. *Cancer Res.* **2011**, 71, 5075-5080.
- Ward KA, Li WI, Zimmer S, Davis T. Viscoelastic properties of transformed cells: role in tumor cell progression and metastasis formation. *Biorheol*. **1991**, 28, 301-313.
- Sun Q, Luo T, Ren Y, Florey O, Shirasawa S, Sasazuki T, *et al*. Competition between human cells by entosis. *Cell Res*. **2014**, 24, 1299-1310.
- Szabò A and Merks RMH. Cellular Potts modeling of tumor growth, tumor invasion, and tumor evolution. *Front. Oncol.* **2013**, 3, 87.
- Xu W, Mezencev R, Kim B, Wang L, McDonald J, Sulchek T. Cell stiffness is a biomarker of the metastatic potential of ovarian cancer cells. *PLoS ONE*. **2012**, 7, e46609.
- Gnach A, Lipinski T, Bednarkiewicz A, Rybka J, Capobianco JA. Upconverting nanoparticles: Assessing the toxicity. *Chem. Soc. Rev.* **2015**, 44, 1561-1584.
- Meyer M and Persson O. Nanotechnology interdisciplinarity, patterns of collaboration and differences in application. *Ed. Sci. Elsevier*. **1998**, 42, 195-205.
- Dasgupta N, Ranjan S, Mundekkad D, Ramalingam C, Shanker R, Kumar A. Nanotechnology in agro-food: from field to plate. *Int. J. Food Res*. **2015**, 69, 381-400.
- Krishnaa VD, Wu K, Cheerana MCJ, Wang JP, Perez A. Nanotechnology: Review of concepts and potential application of sensing platforms in food safety. *Food Microbiol*. **2018**, 75, 47-54.
- Liu WK, Karpov EG, Park HS. Nano mechanics and materials: Theory, multiscale methods and applications. *Ed. Wiley*. **2006**.
- Nautiyal P, Alam F, Balani K, Agarwal A. The role of nanomechanics in healthcare. *Adv. Healthc. Mater*. **2018**, 7, 10.
- Craighead HG. Nanoelectromechanical systems. *Science*. **2000**, 290, 1532-1536.

- Nautiyal P, Alam F, Balani K, Agarwal A. The role of nanomechanics in healthcare. *Adv. Healthc. Mater*. **2018**, 7.
- Crick FHC and Hughes AFW. The physical properties of cytoplasm: A study by means of the magnetic particle method Part I – Experimental. *Exp. Cell Res*. **1950**, 1, 37-80.
- Vilfan ID, Lipfert J, Koster DA, Lemay SG, Dekker NH. Magnetic tweezers for single-molecule experiments. *Handbook of Single-Molecule Biophysics, Springer*. **2009**, 371.
- Gosse C and Croquette V. Magnetic tweezers: micromanipulation and force measurement at the molecular level. *Biophys J.* **2002**, 82, 3314-3329.
- Manosas M, Lionnet T, Praly E, Fangyuan D, Allemand JF, Bensimon D, Croquette V. Studies of DNA-replication at the single molecule level using magnetic tweezers. *Biol. Phys. – Progress in Mathematical Physics vol 60, Springer*. **2010**, 60, 89-122.
- Tanase M, BiaisN, Sheetz M. Magnetic tweezers in cell biology. *Met. Cell Biol.* **2007**, 83, 473-493.
- Fabian R, Tyson C, Tuma PL, Pegg I, Sarkar A. A horizontal magnetic tweezers and its use for studying single DNA molecules. *Micromach.* **2018**, 9, 188.
- Sarkar R and Rybenkov VV. A guide to magnetic tweezers and their applications. *Front. Phys*. **2016**.
- Frewin CL. Atomic force microscopy investigations into biology: from cell to protein. *Intech Open Ed*. **2012**, 372.
- Binnig G, Quate CF, Gerber C. Atomic Force Microscope. Phys. Rev. Lett. **1986**, 56, 930-933.
- Zhong Q, Inniss D, Kjoller K, Elings V. Fractured polymer/silica fiber surface studied by tapping mode atomic force microscopy". *Surf. Sci. Lett*. **1993**, 290, L688.
- Gross L, Mohn F, Moll N, Liljeroth P, Meyer G. The chemical structure of a molecule resolved by Atomic Force Microscopy. *Science*. **2009**, 325, 1110-1114.
- Krieg M, Fläschner G, Alsteens D, Gaub BM, Roos WH, Wuite GJL, *et al*. Atomic force microscopy-based mechanobiology. Nat. Rev. Phys. **2018**, 1, 41-57.
- Carl P and Schillers H. Elasticity measurement of living cells with an atomic force microscope: data acquisition and processing. *Pflugers Arch*. **2008**, 457, 551-559.
- Sirghi L, Ponti J, Broggi F, Rossi F. Probing elasticity and adhesion of live cells by atomic force microscopy indentation. *Eur. Biophys. J*. **2008**, 37, 935-945.

- Radmacher M. Studying the mechanics of cellular processes by atomic force microscopy. *Met. Cell Biol*. **2007**, 83, 347-372.
- Cross SE, Jin YS, Rao J, Gimzewski JK. Nanomechanical analysis of cells from cancer patients. *Nat. Nanotechnol*. **2007**, 2, 780-783.
- Neuman K and Nagy A. Single-molecule force spectroscopy: optical tweezers, magnetic tweezers and atomic force microscopy. *Nat. Methods.* **2008**, 5, 491-505.
- Herbig M, Kräter M, Plak K, Müller P, Guck J, Otto O. Real-time deformability cytometry: label-free functional characterization of cells. *Met. Mol. Biol*. **2018**, 1678, 347-369.
- Mokbel M, Mokbel D, Mietke A, Träber N, Girardo S, Otto O, Guck J, Aland S. Numerical simulation of Real-time deformability cytometry to extract cell mechanical properties. *ACS Biomater. Sci. Eng*. **2017**, 11, 2962-2973.
- Rosendahl P, Plak K, Jacobi A, Kraeter M, Toepfner N, Otto O, *et al*. Real-time fluorescence and deformability cytometry. *Nat. Met*. **2018**, 15, 355-358.
- Park S. Nano-mechanical phenotype as a promising biomarker to evaluate cancer development, progression, and anti-cancer drug efficacy. *J. Cancer. Prev.* **2016**, 21, 73-80.
- Casuso I, Sens P, Rico F, Scheuring S. Experimental evidence for membrane-mediated protein-protein interaction. *Biophys. J.* **2010**, 99, 47-49.
- Bonazza K, Rottensteiner H, Seyfried BK, Schrenk G, Allmaier G, Turecek PL, *et al*. Visualization of a protein-protein interaction at a single-molecule level by atomic force microscopy. *Anal. Bioanal. Chem*. **2014**, 406, 1411-1421.
- Heller I, Hoekstra TP, King GA, Peterman EJG, Wuite GJL. Optical tweezers analysis of DNA-protein complexes. *Am. Chem. Soc. Rev.* **2014**, 114, 3087-3119.

Chapter 2

Nanomechanics of G-quadruplexes within the promoter of the c-kit oncogene

Enrico Buglione, Domenico Salerno, Claudia Adriana Marrano, Valeria Cassina, Guglielmo Vesco, Luca Nardo, Mauro Dacasto, Riccardo Rigo, Claudia Sissi and Francesco Mantegazza.

Submitted

2.1 Abstract

G-quadruplexes (G4s) are tetrahelical DNA structures stabilized by four guanines paired via Hoogsteen hydrogen bonds into quartets. While their presence within eukaryotic DNA is known to play a key role in regulatory processes, their functional mechanisms are still under investigation. In the present work, we analyzed the nanomechanical properties of three G4s present within the promoter of the *c-kit* proto-oncogene from a single-molecule point of view through the use of Magnetic Tweezers (MTs). The study of DNA extension fluctuations under negative supercoiling allowed us to identify a characteristic fingerprint of G4 folding. We further analyzed the energetic contribution of G4 to the double-strand denaturation process in the presence of negative supercoiling, and we observed a reduction in the energy required for strands separation.

2.2 Introduction

G-quadruplexes (G4s) are three-dimensional tetrahelical DNA structures consisting of stacks of planar guanine quartets occurring in G-rich regions of nucleic acid sequences [1]. Different numbers of stacked quartets, the relative strand orientation and the loop composition are responsible for the polymorphism of G4s [2]. A considerable number of such structures occur at the ends of chromosomes, where they are known to impair correct telomere maintenance [3,4]. Moreover, a large number of G4s have been found at different genomic sites, where they play regulatory roles [5,6]. Among these functions, a regulatory role of G4s in the transcriptional activity of several genes has been widely confirmed [7,8].

Recently, single-molecule (SM) techniques have been employed in the study of G4 conformations and nanomechanics [9-13]. The advantage of the SM approach is that it allows a more specific analysis of the complex behavior of G4s, which can be largely obscured by ensemble techniques. In particular, force spectroscopy techniques allow the investigation of sample behaviors under mechanical stress conditions [14,15]. Independent of the employed method, the majority of the currently available SM studies are focused on the analysis of G4 unfolding in a single-stranded DNA context [16-22]. The study of the nanomechanical properties of G4 embedded in ssDNA regions is appropriate for mimicking the biological situation of telomeric G4s, where there is a significant occurrence of G-rich DNA in a single-stranded form. However, in promoter regions, G4-forming sequences

are inserted within the double helix, so the G4 structures can fold only upon bubble formation induced by enzymatic processes and/or torsional stress [22].

From an energetic point of view, the correlation between the presence of G4-forming sequences at certain genomic loci and the probability of bubble formation at those sites is still an open question. Indeed, it is not easy to answer this question via the application of standard ensemble techniques. In particular, in solution, mechanical stress cannot be maintained during thermal melting experiments, and factors such as the application of torque to dsDNA can considerably affect denaturation [23-25].

Among the available SM techniques, Magnetic Tweezers (MTs) allow the application of nanomechanical force and torque to single torsionally constrained dsDNA molecules to induce nanomechanical denaturation, which is a condition that can be considered similar to what is experienced by DNA during replication/transcription [26-31]. Indeed, by imposing a specific twist to a torsionally constrained DNA and simultaneously applying a pulling force to the filament, it is possible to induce the opening of denaturation bubbles [32,33]. If this nanomechanical denaturation involves a DNA region encompassing a G4-forming sequence, it will be feasible to explore the dsDNA-to-G4 transition. For the above reasons, MTs represents a powerful tool for studying the dynamics and nanomechanical characteristics of G4 formation in a context that mimics the nontelomeric configuration.

The usefulness of nanomechanics for studying G4 unfolding within dsDNA was first demonstrated by Selvam *et al.* [17], who applied magneto-optical tweezers to simultaneously impose a controlled twist and a pulling force in the tenths to hundreds of pN range on dsDNA. Similar to previous SM studies on ssDNA, experiments of Selvam *et al.* were based on the detection of the increase in DNA extension resulting from G4 unfolding events. Accordingly, by monitoring the impact of DNA torsional stress on G4 formation, the authors indirectly derived an increase in the G4 folding probability as a consequence of the application of negative supercoiling to the DNA [17].

The promoter of the *c-kit* proto-oncogene, also known as CD117, encodes the mast/stem cell growth factor receptor c-KIT. An increase in the expression of this gene is frequently associated with many forms of cancer, such as mastocytosis, gastrointestinal stromal tumors, lung cancer and leukemia [34]. The regulation of c-KIT transcription levels appears to be largely dependent on the formation of three distinct G4 structures within the proximal promoter of the gene: kit2, kit* and kit1 [35,36]. Accumulating evidence indicates that there is a reduction in *c-kit* expression upon G4 formation at these sites [37]. However, the molecular mechanisms leading to this result have not yet been fully elucidated. Indeed, whereas G4 formation might support the opening of the transcription bubble, the presence of G4s in the promoter might interfere with the proper recruitment of the transcriptional machinery [38]. For this reason, it is extremely important to understand how G4s form and their role in the modulation of DNA architecture.

In the present study, we analyzed the G-quadruplex folding of the dsDNA domain of the *c-kit* promoter, which comprises three G-rich sites, through the use of MTs, through the use of MTs under a low pulling force regime (< 3 pN) over a large range of negative supercoiling. Under these conditions, the separation of the two DNA strands does not require the application of high force (> 65 pN) [39], which would prevent G4 folding [23,32]. The nanomechanical response of the c-*kit* G4-forming domain (*c-kit-wt*) is compared to the behavior of a dsDNA construct in which point mutations have been inserted to prevent the folding of the three G4s (*c-kit-mut*). See the Sequencing outputs section and the Figure S1 in the supplementary material for details on both constructs and the. In this context, we propose a new nanomechanical method for the detection of G4 formation that allows the simultaneous monitoring of G4 folding and quantification of the energy gain due to G4 formation for DNA bubble opening in the presence of the three G4s. MTs results indicate that, despite the higher GC content within the promoter region, the formation of G4s significantly decreases the double-strand helix stability; therefore, the total energy necessary for bubble formation is considerably lower in the presence of G4-forming sequences. This suggests a higher probability of G4 formation from ds-tracts than expected from the sequence composition and fits with the reported observation of G4s in cells during DNA processing [6].

2.3 Results

The investigated construct and the rationale for the MTs experiments are schematically represented in Figure 1, which illustrates how the formation of plectonemes (Figure 1C), DNA denaturation (Figure 1D), and G4 folding (Figure 1E) can affect the extension of DNA (L_e) and its standard deviation (σL_e) (see the Materials and Methods section for details about the constructs and the experimental setup). First, we tested whether the presence of G4s influences the response of the dsDNA filaments to nanomechanical stress by performing MTs force extension experiments with both the *c-kit-wt* and *c-kit-mut* constructs in different buffers (containing KCl, NaCl, or LiCl at 150 mM, which promotes, has a neutral effect on or inhibits G4 folding, respectively). Some representative measurements recorded in 150 mM KCl are shown in Figure 2 for both the wt and the mutant constructs. As shown in Figure 2A, at n_t=0, there were no relevant differences in DNA extension (L_e) measured as a function of the applied force between the two constructs. Namely, at n_t=0, the L_e vs F data were well characterized by the WLC model (continuous lines in Figure 2A) with the same fitting parameters, independently of the presence of G4-forming sequences. Indeed, the resulting fit contour lengths were L_0=2 μm ± 0.12 μm for *c-kit-wt* and L_0=1.97 μm ± 0.14 μm for *c-kit-mut*, which are compatible with the number of base pairs (6680 bp excluding the functionalized tails) in the tethered DNA. The resulting fit persistence lengths provided similar results for *c-kit-wt* and *c-kit-mut* (L_P= 46 nm ± 4 nm and L_P=51 nm ± 5 nm, respectively), in

agreement with data reported for several DNA sequences (see Supplementary materials for similar measurements in different buffers or different conditions) [40-42].

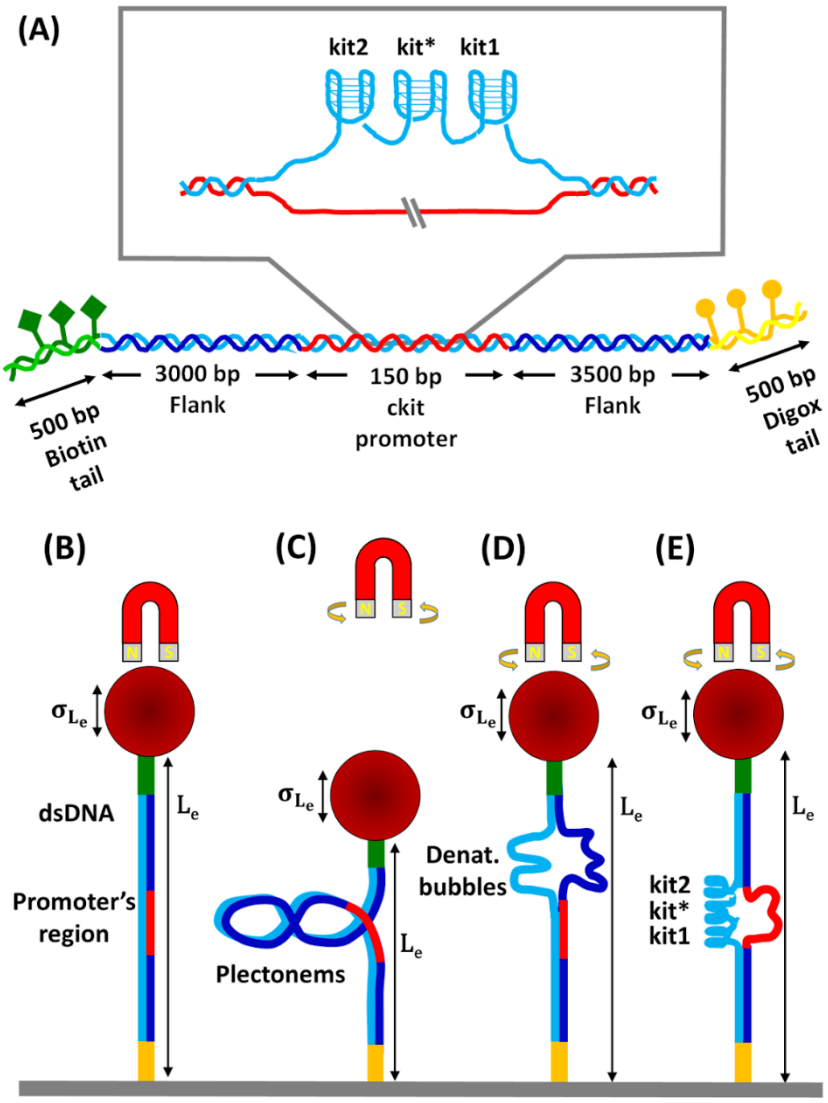

Figure 1. Simplified sketches of the investigated c-kit-wt construct and the MTs experiment strategy. (A): In the central core fragment (red and light blue filaments) containing the human c-kit proximal promoter, three distinct G4s are embedded: kit2, kit* and kit1. This core fragment was flanked by two ~3 kbp flanking regions (dark and light blue filaments), which were enclosed by 5' biotin- and 3' digoxigenin-modified tails (green diamonds and yellow circles, respectively) to bind streptavidin-coated beads and an anti-digoxigenin functionalized microfluidic cell, respectively. (B), (C), (D), (E): A paramagnetic bead (red sphere) is connected via dsDNA to the inner part of a microfluidic cell (gray stripe). By raising the magnets (C), the force

applied to the DNA through the bead decreases, since the magnetic field decreases with the distance. In this condition, the formation of plectonemes instead of denaturation bubbles is favored and the extension is reduced. By rotating the magnets, torque is applied to the DNA. In different states of torsion and force, the initial (B) DNA extension (L_e) and its standard deviation (σL_e) are modified as a consequence of plectonema formation (C), the presence of denaturation bubbles (D), and G4 folding (E).

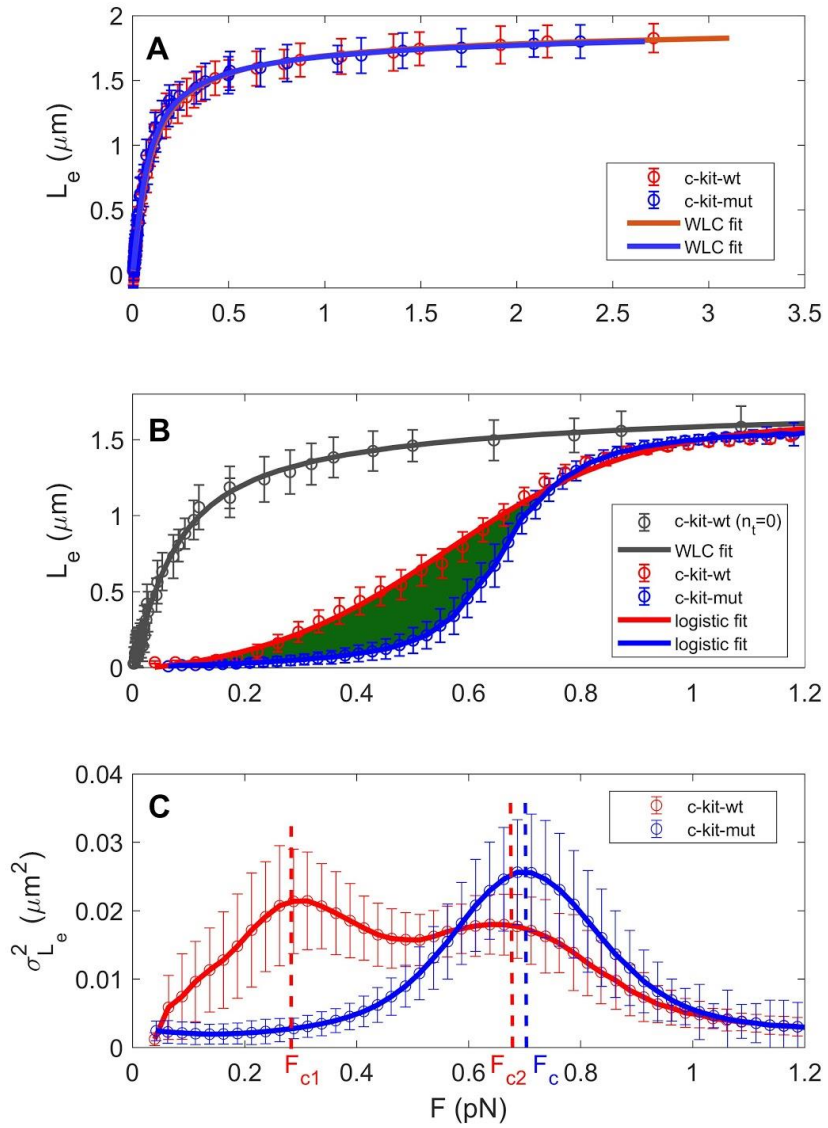

Figure 2. MTs-based nanomechanical characterization of the c-kit-wt (red) and c-kit-mut (blue) constructs at zero or negative supercoiling in 150 mM KCl. (A): Average force extension curves at n_t=0, the standard deviations corresponding to every measurement are also reported. The continuous lines represent the best fit of the data to the WLC model (resulting free parameters: L_0=2 ± 0.12μm, L_p=46 ± 4 nm for c-kit-wt and L_0=1.97 ± 0.14μm, L_p=51 ± 5 nm for c-kit-mut). (B): Average force

extension curves at n_t=-40. The error bars represent the standard deviations measured in hundreds of different force extension curves. The continuous blue and red lines represent a fit to the logistic curve (Equation 1) of the data with fitting parameter values of S_0=0.52 for c-kit-wt and S_0=0.64 for c-kit-mut. The green area between the two curves corresponds to the energy difference between the two extension paths. (C): $\sigma^2 L_e$ variance of DNA extension measured as a function of the applied force (F) for a representative force extension curve at n_t=-40. The vertical dashed lines indicate the maximum value of $\sigma^2 L_e$ and the corresponding characteristic forces (F_C in the case of a single peak or F_{C1} and F_{C2} in the case of a double peak.

To identify nanomechanical fingerprints of G4 folding, we performed force extension experiments while imposing fixed negative torsional stress (n_t=-40, or supercoiling density σ=-40/(N_b /10.4)=-0.070, where N_b is the number of base pairs) on the DNA molecule. Under these conditions, it is possible to explore the phase transition between the plectonemic and denatured states and to analyze the corresponding fluctuations in DNA extension [23-25]. Representative force extension curves acquired for *c-kit-wt* and *c-kit-mut* under negative supercoiling (n_t=-40) in the presence of 150 mM K^+ ions are reported in Figure 2B. The value of n_t=-40 is within a range in which the imposed supercoiling allows the easy evaluation of the corresponding characteristic force. Under this torsional regime, in a relevant statistical ensemble, the force extension curves of *c-kit-wt* show less *steep* behavior than those of *c-kit-mut*. Indeed, as is apparent from Figure 2B, low force (F ≈ 0.3 pN) is sufficient to extend *c-kit-wt*, while the same force did not increase the DNA extension of *c-kit-mut*, which remained negligible until a force F ≈ 0.5 pN. We also observed that at forces higher than 1 pN, the curves of *c-kit-wt* and *c-kit-mut* were superimposable, and

they reached a common asymptotic value (L_0) of DNA extension; the same L_0 was obtained by applying the WLC model to the untwisted filaments (Figure 2A).

It is worth noting that analogous measurements of L_e and $\sigma^2 L_e$ were performed at positive turns in the same range of forces. In the various samples, no relevant differences were found between the condition in which the G4 structures are induced or prevented to form (see Figure S8). In addition, for every condition tested, we never recorded any double peak in the $\sigma^2 L_e$ vs F plot. These data confirm what already observed by Marko and colleagues: in the positive supercoiling regimen, for $n_t>0$ the DNA phase transitions does not involve the dsDNA opening necessary for the G4 folding.

The observed nanomechanical difference between *c-kit-wt* and *c-kit-mut* is more evident considering the variance ($\sigma^2 L_e$) of the instantaneous DNA extension measured as a function of the applied force for $n_t=-40$. As illustrated in Figure 2C, under both the low force (< 0.2 pN) and high force (> 0.9 pN) regimes, where the DNA extension was almost zero or asymptotically L_0 (respectively), the fluctuations of $\sigma^2 L_e$ were negligible. In contrast, under the intermediate regime of forces, the increment of DNA end-to-end extension was associated with an increase in $\sigma^2 L_e$. Precisely, the $\sigma^2 L_e$ vs F plots showed a single or double maximum. In particular, we observed that the majority of *c-kit-mut* molecules exhibited a single maximum of $\sigma^2 L_e$ at a characteristic force $F_C \approx 0.65$ pN (see the representative blue curve in Figure 2C) as expected from previously reported experiments [23-25].

In contrast, a relevant percentage of the *c-kit-wt* molecules show a double peak in the fluctuation of DNA extension under forces of F_{C1} and F_{C2}, as shown by the representative red curve in Figure 2C. We studied the dependence of the variance of the measured DNA extension as a function of the time window of acquisition or as a function of the applied force, on *c-kit-wt* in the presence of K^+, used as reference (Supplementary material, Figure S7). As shown in the figure, after a specific interval of time of about 3 seconds, $\sigma^2 L_e$ reaches an asymptotic value for all the forces explored. Accordingly, to ensure reliable results in the regimen of forces explored, all the measurements presented were acquired in a temporal window larger than 4 seconds.

In Figure 3, we provide a detailed analysis of the statistical distribution of the presence of double peaks in the fluctuations of DNA extension. Specifically, on the first bar in Figure 3, we present the statistical percentage of double peak observations for *c-kit-wt*, as reported in the representative curves in Figure 2C. Here, the measurements were performed in the presence of K^+ ions, a condition that promotes G4 folding due to the coordination of the cations with the stacked G-tetrads. To study whether the double peaks could be considered a nanomechanical *fingerprint* of G4 folding, the presence of single or double peaks in the fluctuations of $\sigma^2 L_e$ was investigated in three control samples: the *c-kit-mut* construct and *c-kit-wt* in different buffers (Figure 3) (see Supplementary material for $\sigma^2 L_e$ vs F data in other buffers).

In principle not only the variance, but also the DNA extension should be affected by the folding of the c-kit G4s. However, this implies a modification of a few nm in the extension, which is difficult to be detected in the low force regimen. On the contrary, in case of negatively imposed torsion, the opening of few bases leads to a large variance of the DNA extension due to the transition between the plectoneme formation and the opening of a denaturation bubble that completely changes the DNA arrangement. The G4s folding results detectable, since it significantly lowers the force of this transition.

In the presence of negative supercoiling, the DNA is under a stress condition, which needs to be relaxed. At low forces, the relaxation occurs by forming plectonemes, while at high forces, it occurs by forming denaturation bubbles (44). The formation of plectonemes reduces the DNA extension, on the contrary, the formation of denaturation bubbles does not severely influence the DNA extension. At intermediate forces, an increase in the fluctuations of DNA extension is observed. These fluctuations reach their maximum at a specific force value FC, which is interpreted, within our theoretical frame, as the equilibrium force between plectonemic and denaturation bubble conditions. Typically, a single peak in the L_e^2 vs F plot is observed. The presence of a sequence able to form G4s in the conditions allowing its folding (i.e. the presence of K^+) opens the probability for a partial denaturation of the DNA aimed to reach this G4s state of single-strand folding. As a result, the presence of a sequence able to fold into G4s would decrease the energy necessary

for opening the DNA. This transition should occur at a force lower than the F_C. In the variance vs F plot, a second peak appears (at a $F<F_C$), corresponding to the G4s formation, associated with the typical peak at F_C ascribable to the plectonemes-to-denaturation bubbles transition, necessary to relax the overall torsion and reach the equilibrium.

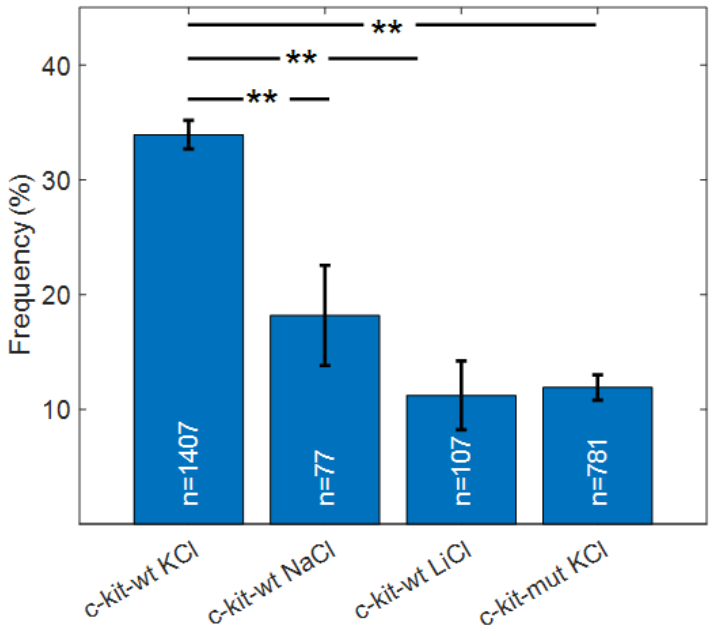

Figure 3. Percentage of double peaks in the $\sigma^2 L_e$ vs F curves obtained at n_t=-40 under different buffer conditions with two constructs: *c-kit-wt* in 150 mM KCl, 150 mM NaCl, and 150 mM LiCl (first three columns); and *c-kit-mut* in 150 mM KCl (last column). The numbers (n) on the histogram bars indicate the total number of measurements acquired under the specific conditions. The error bars represent the corresponding standard deviations calculated assuming pure stochastic behavior and considering the column height as the expected value and n as the sample size. The statistical analysis was performed with the ANOVA test. ** P<0.001.

As shown in Figure 3, the statistical percentage of double-peak observations depends on the presence of both the G4-forming sequence and the ions inducing G4 folding. Indeed, the experimental conditions known to promote G4 formation resulted in a double peak in the fluctuations of $\sigma^2 L_e$ more frequently than the conditions in which G4 formation was inhibited. In particular, among an ensemble of more than 2000 curves, double peaks were observed in approximately 35% of the measurements of *c-kit-wt* in the presence of 150 mM KCl, which was the most efficient stabilizer of the G4 structure. This percentage decreased to approximately 18% for measurements performed on *c-kit-wt* in the presence of the same concentration of NaCl, approximately 11% for *c-kit-wt* in the presence of LiCl and approximately 12% in the case of *c-kit-mut* in KCl buffer.

To analyze whether the statistical distribution of double peaks was also influenced by the specific value of the imposed supercoiling, we studied the fluctuations in DNA extension at various n_t values. As shown in Figure 4, the percentage of the observed double peaks for *c-kit-wt* in 150 mM KCl reached a maximum at n_t=-30, while it decreased to less than 3% under a greater negative supercoiling regime (n_t=-100).

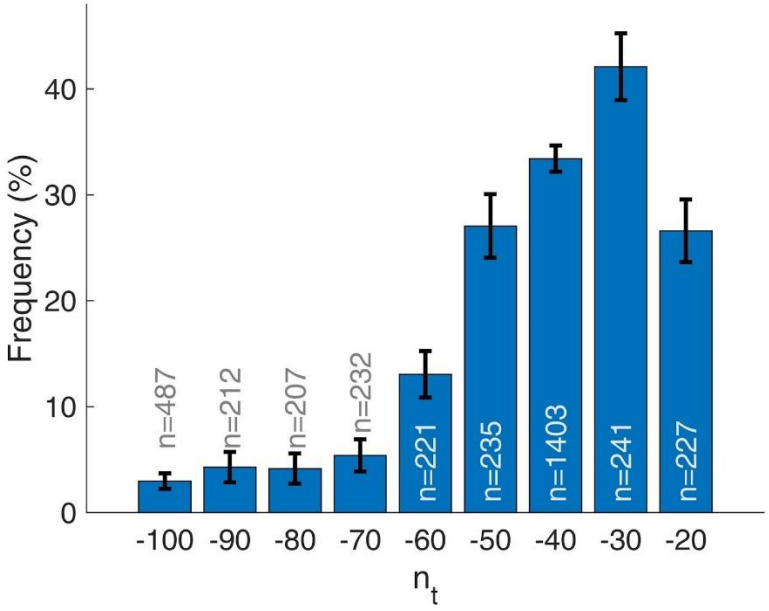

Figure 4. Percentage of double peaks in the fluctuations of DNA extension as a function of the imposed turns. Data acquired for c-kit-wt in 150 mM KCl buffer for different numbers of imposed turns (n_t). For each n_t, the reported percentage was calculated for a number (n) of measurements, as indicated by the labels on the histogram columns. The error bars represent the corresponding standard deviations, calculated assuming purely stochastic behavior and considering the column height as the expected value and n as the sample size.

In Figure 5, we report the statistical distribution of the characteristic force values measured for nt=-40 i.e. for supercoiling density σ=-0.070, in the case of both a single peak (F_C) and a double peak (F_{C1} and F_{C2}). In the latter case, G4 folding induces a local maximum in the fluctuations at a lower force value (F_{C1}=0.37 pN ± 0.14 pN), while a higher characteristic force (F_{C2}=0.69 pN ± 0.15 pN) coincides with the characteristic force observed in the curves with a single peak (F_C=0.69 pN ± 0.11 pN). In the inset of Figure 5, the statistical distribution of

ΔF_{double} (i.e., the difference between F_{C1} and the corresponding F_{C2} ($\Delta F_{double}=F_{C2}–F_{C1}$)) confirms the systematic difference between the two characteristic force values.

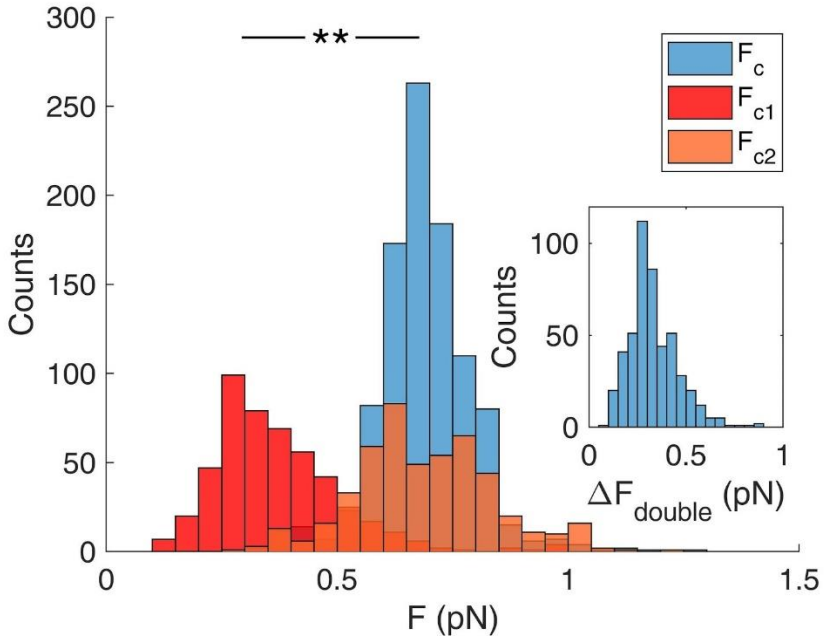

Figure 5. Characteristic force analysis. Statistical distribution of the measured values of the characteristic forces (F_C, F_{C1}, F_{C2}) for c-kit-wt in 150 mM KCl. Single-peak characteristic force (F_C) is indicated in blue, double peak characteristic forces in red (F_{C1}) and orange (F_{C2}). Inset: statistical distribution of the force difference, ΔF_{double}= F_{C1} - F_{C2}. The statistical analysis was performed with the T test. ** P<0.001.

Finally, since the L_e vs F curves corresponding to $\sigma^2 L_e$ vs F curves exhibit a single peak present on average a higher *steepness* compared to those measured for double-peaked $\sigma^2 L_e$ vs F curves, we quantified this

feature by fitting the data with a phenomenological logistic function given by the following expression:

$$L_e = A + \frac{B}{1+e^{\frac{F-F_1}{S_0}}} \qquad \text{(Equation 1)}$$

where A and B are two normalization constants, S_0 is a parameter that represents the curve *steepness*, and F_1 is the symmetric point of the logistic function. The statistical distributions of the S_0 parameter for *c-kit-wt* and *c-kit-mut* were significantly different, as verified by the Wilcoxon text, ($P<0.001$ data shown in Figure 6).

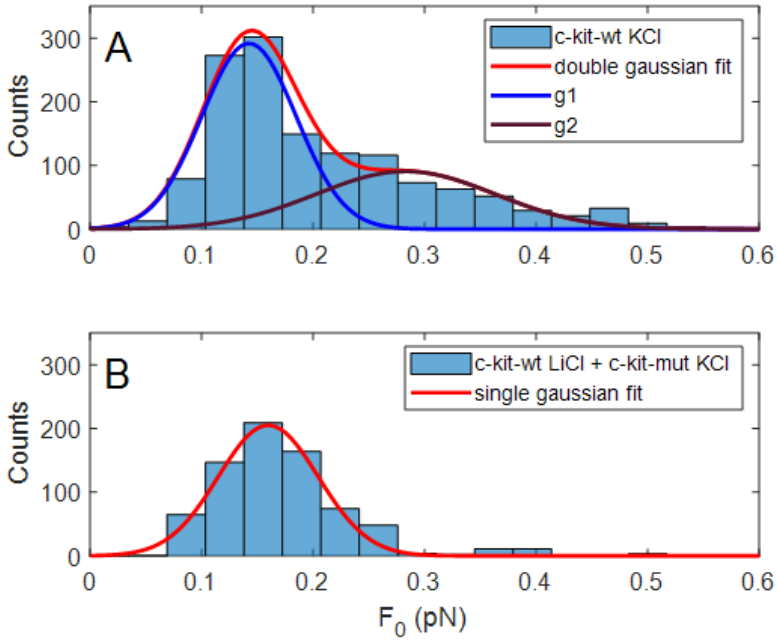

Figure 6. Statistical distribution of the steepness parameter (S_0) derived from the fitting of the L_e vs F curves with the logistic function (Equation 1). Data acquired n_t=-40 for c-kit-wt in KCl (A) and for c-kit-wt in LiCl and c-kit-mut in KCl (B). The continuous lines represent the fit of the reported data to a single Gaussian (red line in panel (B)) or to a double Gaussian (red line of panel (A) resulting from the sum of the single Gaussians described by curves blue (g1) and purple (g2)). The Wilcoxon test shows P<0.001, confirming the significant difference between the two distributions described in panels (A) and (B).

It is worth noting that analogous measurements of Le and L_e^2 were performed at positive turns in the same range of forces. In the various samples, no relevant differences were found between the condition in which the G4 structures are induced or prevented to form (see Figure S5 in Supplementary Material). In addition, for every condition tested, we never recorded any double peak in the L_e^2 vs F plot. These data confirm what already observed by Marko and Neukirch: in the positive

supercoiling regimen, for n_t>0 the DNA phase transitions does not involve the dsDNA opening necessary for the G4 folding.

2.4 Discussion

In this work, the MTs technique was applied to analyze the nanomechanical characteristics of a domain of the proximal promoter of the *c-kit* proto-oncogene that contains three G4-forming sites. We observed that, in the absence of supercoiling, the presence of these G4-forming sequences did not alter the nanomechanical properties of the double-stranded DNA filament. Indeed, the measured standard nanomechanical parameters, such as contour and persistence lengths, were not affected by the presence of the G4 sequences. These results appear reasonable, given that such parameters are normally weakly dependent on the specific DNA sequence composition [43]. Furthermore, the number of bases involved in the three distinct G4s within the *c-kit* promoter represents approximately 2% of the total number of bases in the DNA filament. However, the presence of these few bases in the *c-kit* promoter sequence were revealed when the DNA filament was under the effect of negative torsion.

In general, the folding of a G4 structure in a dsDNA filament needs to be preceded by the separation of the two strands. *In vitro*, strand opening can be obtained in the absence of negative torsion by applying force exceeding 65 pN [39]. However, the DNA extension imposed by such high forces would prevent G4 folding. In contrast, in the presence of negative supercoiling, nanomechanical denaturation can be obtained at forces below 1 pN [23,32], under which a G4 structure can easily fold.

In this negative supercoiling regime, peculiar nanomechanical behavior of the DNA sequence under investigation was observed; i.e., a double peak occurred in the $\sigma^2 L_e$ versus F curve. In the presence of K^+, which is an ion favoring G4 folding, we observed a statistically significant increase in the percentage of double peaks for the DNA containing the *c-kit-wt* promoter with respect to the controls, in which either mutations or different ions prevent G4 folding. In addition, we observed that the occurrence of the double peak recapitulated the efficacy of the different ions in coordinating and stabilizing G4 structures as described in the literature: $K^+ > Na^+ > Li^+$ [44,45]. Indeed, the percentage of double peaks, which was 35% in association with K^+, was almost halved, to 18%, in the presence of Na^+ and was further reduced to 11% in association with Li^+. The statistical correlation between the appearance of a double peak in the $\sigma^2 L_e$ versus F curve and conditions favoring or inhibiting G4 folding suggests that the occurrence of the double peak might be considered a fingerprint of G4 formation. Moreover, the statistical distribution of double peaks observed under the different experimental conditions was in qualitative agreement with the probability distribution of G4 formation at the single-molecule level, measured by monitoring the unfolding events occurring under high tension (approximately 40 pN) by Selvam and colleagues [17]. Since we studied a different promoter, only a qualitative comparison with their work can be performed. Nevertheless, the discrepancy between the occurrence of G4s in *c-kit-mut* in K^+ (12%) and *c-kit-wt* in Li^+ (11%) indicated by our data and the corresponding values (3% and 4%, respectively) presented in Selvam's

work deserves comment. Regarding the data obtained in the presence of K^+, this discrepancy could be reasonably due to the different characteristics of the control samples. In Selvam's paper, the sequence used as a control did not contain the G4 sequence, while in our case, the *c-kit-mut* contained only a few mutated residues; thus, despite the inserted point mutations, some weakly folded states may still occur [46-48]. Furthermore, as highlighted above, the promoter sequence analyzed in our experiments differed from that considered in Selvam's work. In particular, we studied a longer sequence containing three distinct subregions that could fold into G4s either independently or through G4-G4 crosstalk [49,50]. Such a long sequence is more prone to present alternative single-strand structures (i.e., hairpins or incompletely paired domains, which may interfere with G4 folding recognition).

We cannot exclude that the residual double peaks observed in the negative controls (about 12% instead of 0%) can be related to the formation of alternative secondary structures (e.g. hairpin or cruciform extrusions) able to relax the negative turns imposed to the DNA, with an energy gain comparable to the one we attribute to the G4s. Anyway, a statistically significant increment in this percentage is observed in the conditions favouring the G4s formation. On the other side, the probability of double peaks occurrence (about 35%) could depend on the denaturation bubble opening, which is a random event: in all the cases in which plectonemes hide the c-kit promoter region, the G4s formation is prevented, reducing the probability of double

peaks occurrence. Moreover, the DNA geometry in negative supercoiling could also contribute by partially preventing G4s formation.

Our results suggest that the presence of a G4-forming sequence alters the energetic balance between plectonemes formation and bubble opening. Indeed, for $n_t<0$, the presence of a low-force secondary peak at F_{C1}=0.35 pN in the $\sigma^2 L_e$ vs F curves suggests that the transition between bubble and plectonemes formation is anticipated at lower force values. In addition, it was possible to quantify the energetic contribution of the G4 structure by using the following equation, which expresses the energy cost of relaxing a single turn by opening the double strand in terms of the characteristic force (F_C) and bending constant (B) [23,25]:

$$\alpha = \pi * \sqrt{8 * B * F_C} \qquad \text{(Equation 2)}$$

If we ascribe a characteristic force of F_{C1}=0.35 pN to the DNA transition between double-strand and G4 folded structures and a characteristic force of F_{C2}=0.65 pN to the transition between the double-strand and denaturation bubble structures, we can calculate the ratio between the two transition energies by using the following formula:

$$\sqrt{\frac{Fc1}{Fc2}} = 0.73 \qquad \text{(Equation 3)}$$

Considering the whole G4-forming sequence present in the DNA construct (see Supplementary Materials), we expect an energy cost of approximately 120 kcal/mol will be incurred in opening the G4-

forming sequence [43,51]. This value, multiplied by the calculated factor of 0.73, results in a cost of 88 kcal/mol in the case of G4 formation, with a net energy gain of 32 kcal/mol. This result is close to the expected energy gain calculated by assuming a value of 10 kcal/mol, predicted for each G4 formation [43,52], and by considering the presence of three G4s in the investigated sequence.

Since the melting of the double strand corresponds to an increase in filament extension, the occurrence of partial denaturation of *c-kit-wt* in K^+ under low force indicates early destabilization of the double helix, which is also observed in the force extension curve as a decrease in the steepness of the L_e vs F curves under negative supercoiling. These data show that the DNA filament in the presence of G4 sequences is more easily extended under lower forces; i.e. the plectonemic structure is less probable than denaturation bubbles. As a result, the statistical distribution of the S_0 parameter obtained from the logistic fit, which describes the *steepness* of the force extension curve, is considerably different for *c-kit-wt* in K^+ (high probability of G4 folding) than for *c-kit-mut* in K^+ and *c-kit-wt* in Li^+ (low probability of G4 folding). Even though the superposition area of the two Gaussian distributions shown in Figure 6A is too large to clearly identify a single G4 folding event by using only the *steepness* parameter (S_0), a difference in the shape of the two distributions can be observed. In particular, for the control sequences, a single Gaussian fit describes the S_0 distribution well. In contrast, the statistics for *c-kit-wt* in K^+ are described by a double Gaussian distribution, and the calculated

relative Gaussian areas are 63% for the high-steepness Gaussian (lower S_0) and 37% for the low-steepness Gaussian (high S_0), in good agreement with the relative abundance of the double peak (35%, as shown in Figure 3).

The analysis of the force extension curves in the presence of negative supercoiling confirmed the ability of the MTs technique to reveal G4 folding events. It also provided additional information, since it enabled the quantification of the energetic contribution in the destabilization of the double helix due to the presence of the *c-kit* promoter sequence. A comparison between the mean force extension curves related to the double-peak cohort and the single-peak cohort revealed a significant difference in the work of the magnetic pulling force exerted to extend the DNA. In fact, the work applied to extend the DNA in the case of the curves showing a double peak of $\sigma^2 L_e$ was significantly lower than the work applied in the case of a single peak. This difference could be easily calculated by measuring the area between the two curves (green area in Fig 2B), resulting in a value of 24 kcal/mol ± 6 kcal/mol, which is in reasonable agreement with the value calculated using the formula extracted from a published mechanical model (see Equation 2) [23] and compatible with the expected energy gain due to G4 formation [43,52]. These three converging estimates suggest that the proposed approach is valuable and can provide reliable quantification of the energetic change in double-strand stability induced by the presence of G4 sequences

under realistic conditions of a negative torque and pulling force close to physiological conditions.

A further indication of the correlation between G4 formation and double-peak occurrence emerges from Figure 5, where the dependence of the statistical distribution of the double peak is reported as a function of the applied supercoiling. Indeed, the data suggest the existence of specific negative torsion that is more efficient in promoting G4 folding. This negative value of n_t around 30 turns implies the opening of approximately 100 bp region of a DNA sequence of 6680 bp [23], compatible with the length of the *c-kit* promoter sequence, which is 72 bp long.

In principle, it would be possible to identify different substructures (folding of single or double G4s only) that could be folded within the promoter sequence. Actually, the histogram relative to the distribution of forces reported in Figure 5 shows a large single peak distribution (red histogram) in the low force regime, which can be supposed to be due to the presence of multiple peaks summed up. Unfortunately, this hypothesis cannot be verified by the analysis of our data, since the intrinsic noise due to the Brownian motion of the bead limits the experimental resolution, hindering the discrimination between a single wide peak and an ensemble of close multiple narrow peaks.

2.5 Conclusions

Overall, we can conclude that the presence of G4-forming sequences induces a counterintuitive alteration of nanomechanical DNA behavior. Indeed, despite the presence of a large number of GC base pairs, characterized by more stable pairing [51], DNA containing G4 sequences is more easily locally denatured under suitable torsion. Indeed, since the local separation of the double strand is necessary before G4 folding, the formation of these DNA secondary structures is energetically facilitated by negative torsion. According to the analysis of the force extension curves, the energy gain in this step derived from the formation of three G4s can be estimated to be approximately 24 kcal/mol.

Thus, our findings suggest that the G4-forming sequences within the *c-kit* promoter are crucial in determining the overall architecture of the promoter itself and, thus, contribute to the dynamic fine regulation of gene expression. Therefore, our results further suggest that the G4s within the *c-kit* promoter could represent successful candidates for targeted therapy in the case of the misregulation of this proto-oncogene.

2.6 Methods

Preparation of DNA constructs

DNA tethers were constructed from five components: a 148 bp core fragment containing the *c-kit* promoter region and two identical handles of 2881 bp, each flanking one side of the core fragment bookended by 3' biotin- and 5' digoxigenin-modified tails (see Fig. 1A). In the case of the *c-kit-wt* construct, the G4-forming sequence corresponds to the portion between positions -158 and -87 upstream of the transcription starting site (TSS), which includes the three G4-forming sequences (in order from the 5' end: kit2, kit* and kit1). A mutated form of the same sequence, referred to as *c-kit-mut*, in which each G4-forming sequence was subjected to point mutation to prevent G4 formation, was used as a negative control construct (see Supplementary materials for sequence details). The sequence of either *c-kit-wt* or *c-kit-mut* was inserted into the pGAL4.1 plasmid between the XmaI and NheI restriction sites.

The two flanking regions were obtained via mutagenic PCR amplification performed with LongAmp DNA polymerase (NEB) using Lambda DNA N6-methyladenine-free (Sigma-Aldrich, st. Louis, MO) as a template and the following forward primer: 5'-AAA**GGTAC*CTC*GAG**TGCGACAGGTTTGATG-3', and reverse primer: 5'-TTT**GGTAC*CTC*GAG**CGAAATTAACTCTCAGG-3'. Each primer contains both XhoI (italic) and KpnI (underlined) restriction sites; the mutagenic regions are indicated in bold. The DNA sequence used as a template

for the flanking region was chosen with online software because it was devoid of non-B DNA sequences [17,53].

Subsequently, the flanking regions were cloned into each plasmid upstream and downstream of the core sequence by taking advantage of the 3' KpnI and the 5' XhoI restriction sites, respectively. To obtain a sufficient amount of the "flanking_core_flanking" sequence, competent DH5α *E. coli* strain cells were transformed with the plasmid containing either *wt* or *mut* insert. Plasmid DNA was extracted starting from a 50 ml cell culture that was grown overnight at 37°C using a Qiagen Midi Prep Kit. The purified DNA was then enzymatically digested with the ApaI and SacII restriction enzymes (NEB) by taking advantage of the two restriction sites already present in the pGAL4.1 plasmid and purified with a QIAquick PCR Purification Kit (Qiagen, Germantown, MD). The total length of the flanking core flanking sequence was 6680 bp. At the end of the two cloning steps, the 72 bp region encompassing the three G4-forming sequences was verified by a sequencing analysis, both in the case of the *c-kit-wt* and *c-kit-mut* plasmid (see Supplementary Material for details).

The two functionalized tails were amplified by mutagenic PCR starting from the pBR322 plasmid (Roche, Basel, Switzerland) using Taq DNA polymerase (Euroclone, Italy). PCR was carried out in the presence of 20% biotin-16-dUTP- or 20% digoxigenin-11-dUTP-labeled nucleotides (Roche) using the forward mutagenic primers 5'-AAA**CCGCGGC**CAGAACATTTCTCTGGCCT-3' and 5'-GCTT**GGGCCC**CAGAGTTCTTGAAGTGGTGG-3', containing the SacII and

ApaI restriction sites, respectively (underlined), and the same reverse primer: 5'-GGTCCAGTCGTCGGGTCTCGCGGTAT-3'.

The samples were purified by using the QIAquick PCR Purification Kit (Qiagen, Germantown, MD) and subsequently digested for 16 h using the appropriate restriction enzyme and subjected to further purification. Ligation between the two flanking-core-flanking sequences and the tails was carried out by taking advantage of the nick-joining activity of the T4 DNA ligase (NEB) at 16°C for 72 h. The final construct length was ~7.5 kbp. The presence of the final constructs was confirmed by 0.8% agarose gel electrophoresis.

Magnetic tweezers setup and measurements

In this work, we used a custom MTs setup [54], essentially consisting of an inverted optical microscope (Nikon 60X, 1.49NA oil immersion with a 20-cm-focal-length tube lens) coupled with a system in which permanent neodymium magnets were located over a microfluidic flux cell (custom Hybriwell3, Grace BioLabs, USA) for DNA incubation. Illumination was provided by an infrared (840 nm) superlumen diode (Superlum SLD-34-MP, UK) producing light endowed with high spatial coherence and low temporal coherence, allowing the focalization of the beam and achieving high intensity in the focal plane while avoiding out-of-focus interference. The images were acquired with a fast Cmos camera (Eosens 3CL Mikrotron) operating at 300 Hz with 1 MP of resolution and a 100 µs exposure time. The real-time image analysis allowed the simultaneous tracking of up to 40 beads over 3 d with a resolution of 60 nm in the x-y plane and 10 nm in the Z direction.

The magnets could be translated along and rotated around the optical axis to control the tension and supercoiling of the DNA tethers. The inner surface of the microfluidic cell was functionalized overnight at 4°C with an anti-digoxigenin antibody at 20 µg/µl (Roche, Italy). The functionalized surface was then passivated overnight at 4°C with 10 mg/ml bovine serum albumin (Roche) in 150 mM phosphate-buffered saline, pH 7.4 (PBS).Streptavidin-coated superparamagnetic beads with a 1 µm diameter (Dynabeads MyOne Streptavidin C1, Dynal, Invitrogen, Milan, Italy) were tethered to the DNA filaments upon incubation at room temperature for 30 min. Finally, the bead-labeled DNA suspension was incubated in the microfluidic cell for 1 h before washing out the excess unbound tethers.

MTs measurements were carried out in Tris-HCl buffer supplemented with 0.1% Tween-20 and 0.1 mM EDTA added with KCl to promote G4 formation, or LiCl to inhibit G4 formation, or NaCl as control buffer. In all subsequent measurements, the KCl, LiCl, and NaCl concentrations were maintained at 150 mM.

Force-extension curve and characteristic force.

The outputs of a standard MTs experiment are the force extension and turn-extension curves, where the DNA end-to-end extension (L_e) is measured as a function of either the applied force (F) or the number of imposed turns (n_t), respectively [55-57]. In a force extension curve, when no torsion is applied to the DNA (i.e., n_t=0), L_e increases with F, reaching an asymptotic value. In this case, the curve is well described by the Worm-Like-Chain (WLC) model [56,58] through the use of two

fitting parameters: the DNA contour length (L_0) and the DNA persistence length (L_P) [59-61]. When n_t is different from zero, the force extension curve exhibits a different shape with respect to the n_t=0 situation [33]. Under negative supercoiling (n_t<0), the force extension curve presents two distinct regions: a low-force region, where the DNA extension is negligible, and a high-force asymptotic region, where the force extension curve is similar to that obtained in untwisted conditions (n_t=0) and follows the WLC model. In the low-force regime, the filament is in a collapsed plectonemic state, while with increasing force, the imposed turns in the DNA are relaxed by opening denaturation bubbles, involving a number of base pairs proportional to the supercoil magnitude. These two regions are separated by a small range of forces at which the DNA extension value increases steeply between the collapsed and extended states, suggesting coexistence between plectonemes and denaturation bubbles [23,25]. This DNA extension jump occurs at a characteristic force value (F_C) depending on the DNA persistence length and base pairs melting energy [62]. As a consequence of the coexistence of the two states, the fluctuations in DNA extension (evaluated on the basis of the variance ($\sigma^2 L_e$) of the DNA extension) increase greatly in the transition region, and the F vs $\sigma^2 L_e$ plot clearly exhibits a bell-like shape, which allows the F_C at which $\sigma^2 L_e$ reaches its maximum value to be easily identified [24,63].

Operatively, the detection of the characteristic force, F_C, is obtained by performing several force-extension measurements at fixed

imposed turns. The force ramp is performed by using an interval of 0.01 pN. For each force value, we considered the corresponding variance of DNA extension. F_C is the force at which reaches its maximum value.

2.7 Supplementary data

Figure S1. DNA sequences of the two core constructs comprised between position -158 and -87 upstream the Transcription Starting Site (TSS) of the c-kit proximal promoter. Above, the 72 bases of c-kit-wt are reported, the sequence of kit2, kit* and kit1 are highlighted in yellow, cyan and green respectively. Below, the G to T point mutations present in c-kit-mut, which impair the folding of the three G4, are indicated in red.

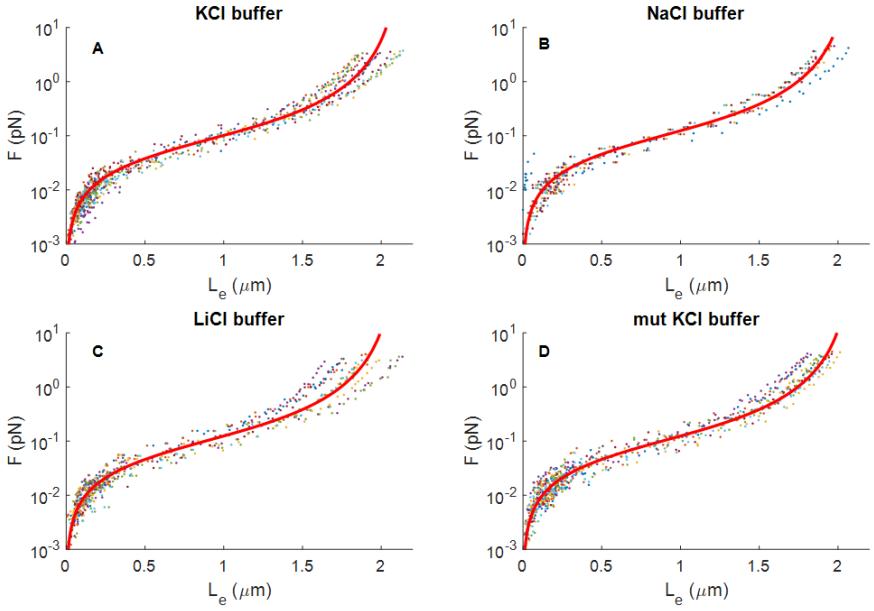

Figure S2. Representative force-extension data obtained with MTs techniques at n_t=0 for the c-kit-wt construct in 150 mM KCl (A), NaCl (B) and LiCl (C) buffers and for the c-kit-mut construct in 150 mM KCl buffer (D). The colored dots represent the

experimental data and the red line represents the WLC fit. The corresponding fitting parameters are reported in Table S1.

	c-kit-wt 150mM KCl	*c-kit-wt* 150mM NaCl	*c-kit-wt* 150mM LiCl	*c-kit-mut* 150mM KCl
L_0 (μm)	2.00 ± 0.12	1.97 ± 0.14	2.10 ± 0.17	2.10 ± 0.11
L_p (nm)	46 ± 4	51 ± 5	46 ± 6	46 ± 3

Tab S1. End-to-end length L_0 and persistence length L_P parameters resulting from fitting of the force-extension data acquired for the specified construct to the WLC model in different buffers.

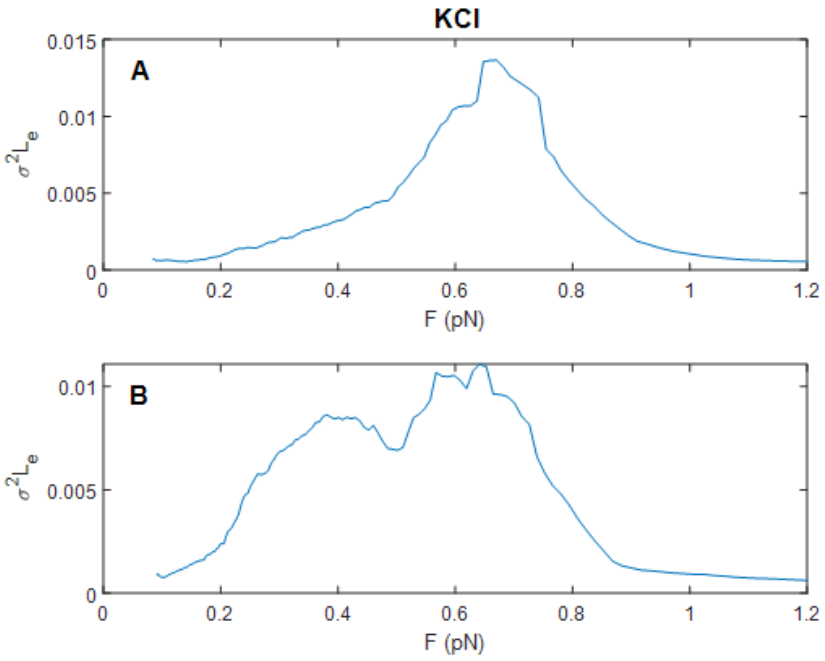

Figure S3. Variance $\sigma^2 L_e$ of the DNA extension data measured as a function of the applied force F for a representative force-extension curve at n_t=-40. Data taken for c-kit-wt construct in 150 mM KCl. (A) single peak representative data, (B) double peak representative data.

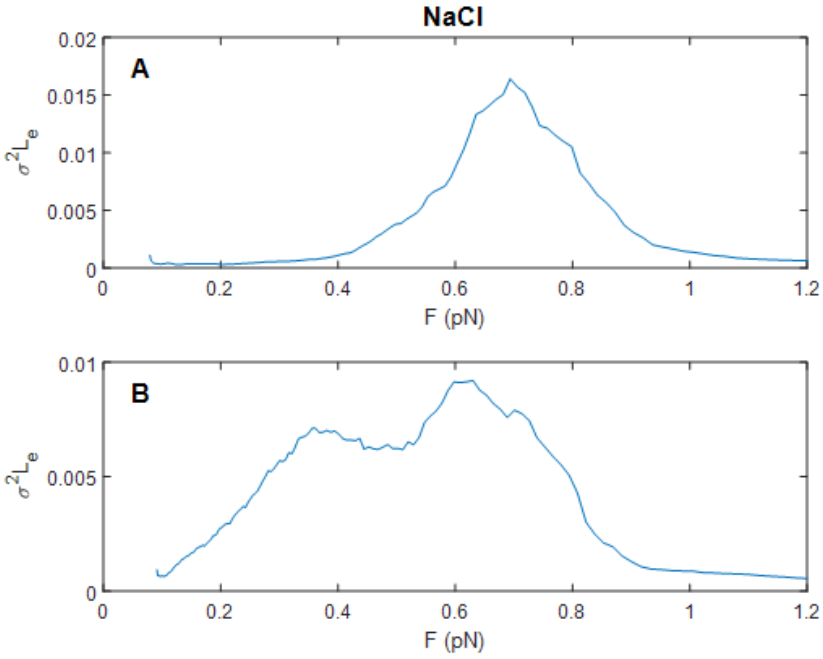

Figure S4. Variance $\sigma^2 L_e$ of the DNA extension data measured as a function of the applied force F for a representative force-extension curve at n_t=-40. Data taken for c-kit-wt construct in 150 mM NaCl. (A) single peak representative data, (B) double peak representative data.

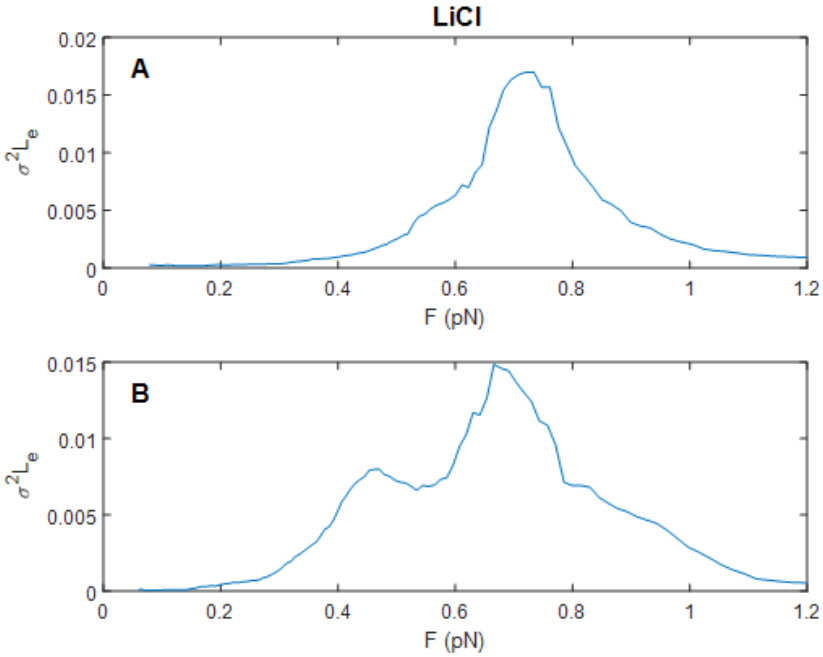

Figure S5. Variance $\sigma^2 L_e$ of the DNA extension data measured as a function of the applied force F for a representative force-extension curve at n_t=-40. Data taken for c-kit-wt construct in 150 mM LiCl. (A) single peak representative data, (B) double peak representative data.

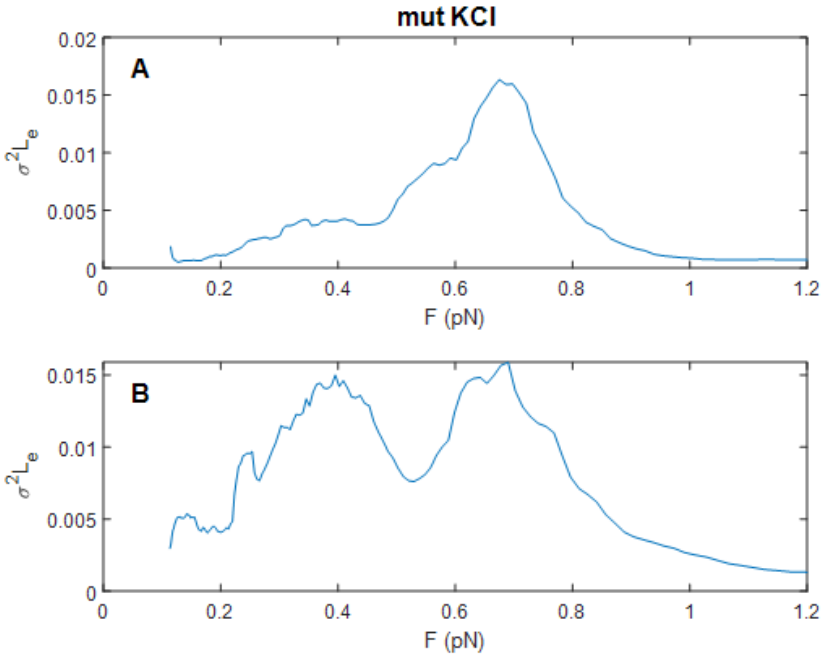

Figure S6. Variance $\sigma^2 L_e$ of the DNA extension data measured as a function of the applied force F for a representative force-extension curve at n_t=-40. Data taken for c-kit-mut construct in 150 mM KCl. (A) single peak representative data, (B) double peak representative data.

Sequencing outputs

>c-kit-wt FW

AGGCGAGGAGGGGCGTGGCCGGCGCGCAGAGGGAGGGCGCTGGGAGGAGGG
GCTGCTGCTCGCCGCTCGCGGCTCTGGGGGCTCGGCTTTGCCGCGCTAGCC
TCGAGCGAAATTAACTCTCAGGCACTGCGTGAAGCGGCAGAGCAGGCAATG
CATGACGACTGGGGATTTGACGCAGACCTTTTCCATGAATTGGTAACACCA
TCGATTGTGCTGGAACTGCTGGATGAACGGGAAAGAAACCAGCAATACATC
AAACGCCGCGACCAGGAGAACGAGGATATTGCGCTAACAGTAGGGAAACTG
CGTGTTGAGCTTGAAACAGCAAAATCAAAACTCAACGAGCAGCGTGAGTAT
TACGAAGGTGTTATCTCGGATGGGAGTAAGCGTATTGCTAAACTGGAAAGC
AACGAAGTCCGTGAAGACGGAAACCAGTTTCTTGTTGTTCGCCATCCTGGG
AAGACTCCTGTTATCAAGCACTGCACTGGTGACCTGGAAGAGTTTCTGCGG
CAGTTAATCGAACAAGACCCGTTAGTAACTATCGACATCATTACGCATCGC
TATTACGGGGTTGGAGGTCAATGGGTTCAGGATGCAGGTGAGTATCTGCAT
ATGATGTCTGACGCTGGCATTCGCATCAAAGGAGAGTGAGATCGGTTTTGT
AAGAGATAACGCTTGTGAAAATGCTGAATTTCGCGTCGTCTTCACAGCGAT
GCCAGAGTCTGTAGTGTCAGATGATGACCGTACTCAAACATCGGGTTGAGT
ATTATCTTACTGTTTCTTTACATAAACATTGCTGATACCGTTTAGCTGAAA
CGACATACATTGCAAGGAGTTTATAAATGAGTATCAATGAGTTAGAGTCTG
AGCAAAAAGATTGGGCGTTATCAATGTTGTGCAGATCCGGTGTCTTGTCTC
CATGCAGACATCACGAAGGTGTTTATGTAGATGAAGGTATAGATATAGAGT
CGGCATACAA

>c-kit-wt REV COMP

CGAGCAGCAGCCCCTCCTCCCAGCGCCCTCCCTCTGCGCGCCGGCCACGCC
CCTCCTCGCCTCCCCTCCCTCGCGCCCGCCCGGGTCTCGCTTCTTCCCGGC
GGCGTCTGGTACCTCGAGTGCGACAGGTTTGATGACAAAAAATTAGCGCAA
GAAGACAAAAATCACCTTGCGCTAATGCTCTGTTACAGGTCACTAATACCA
TCTAAGTAGTTGATTCATAGTGACTGCATATGTTGTGTTTTACAGTATTAT
GTAGTCTGTTTTTTATGCAAAATCTAATTTAATATATTGATATTTATATCA
TTTTACGTTTCTCGTTCAGCTTTTTTATACTAAGTTGGCATTATAAAAAGG
CATTGCTTATCAATTTGTTGCAACGAACAGGTCACTATCAGTCAAAATAAA
ATCATTATTTGATTTCAATTTTGTCCCACTCCCTGCCTCTGTCATCACGAT
ACTGTGATGCCATGGTGTCCGACTTATGCCCGAGAAGATGTTGAGCAAACT
TATCGCTTATCTGCCTCTCATAGAGTCTTGCAGACAAACTGCGCAACTCGT
GAAAGGTAGGCGGATCCCCTTCGAAGGAAAGACCTGATGCTTTTCGTGCGC
GCATAAAATACCCTGATACTGTGCCGGATGAAAGCGGTTCGCGACGAGTAG
ATGCAATTATGGTTTCTCCGCCAAGAATCTCTTTGCATTTATCAAGTGTTT
CCTTCATTGATATTCCGAGAGCATCAATATGCAATGCTGTTGGGATGGCAA
TTTTTACGCCTGTTTTGCTTTGCTCGACATAAAGATATCCATCTACGATAT
CAGACCACTTCATTTCGCATAAATCACCAACTCGTTGCCCGGTAACAACAG
CCAGTTCCATTGCAAGTCTGAGCCAACATGGTGATGATTCTGCTGCTTGAT

AAATTTTCAGGTATTCGTCAGCCGTAAGTCTTGATCTCCTTACCTCTGATT
TTGCTGCGCGAG

>c-kit-mut FW

GAGTCGATGAGGGGCGTGGCCGGCGCGCAGAGGGAGTTCGCTGGGAGGAGG
GGCTGCTGCTCGCCGCTCGCGGCTCTGGGGGCTCGGCTTTGCCGCGCTAGC
CTCGAGCGAAATTAACTCTCAGGCACTGCGTGAAGCGGCAGAGCAGGCAAT
GCATGACGACTGGGGATTTGACGCAGACCTTTTCCATGAATTGGTAACACC
ATCGATTGTGCTGGAACTGCTGGATGAACGGGAAAGAAACCAGCAATACAT
CAAACGCCGCGACCAGGAGAACGAGGATATTGCGCTAACAGTAGGGAAACT
GCGTGTTGAGCTTGAAACAGCAAAATCAAAACTCAACGAGCAGCGTGAGTA
TTACGAGGGTGTTATCTCGGATGGGAGTAAGCGTATTGCTAAACTGGAAAG
CAACGAAGTCCGTGAAGACGGAAACCAGTTTCTTGTTGTTCGCCATCCTGG
GAAGACTCCTGTTATCAAGCACTGCACTGGTGACCTGGAAGAGTTTCTGCG
GCAGTTAATCGAACAAGACCCGTTAGTAACTATCGACATCATTACGCATCG
CTATTACGGGGTTGGAGGTCAATGGGTTCAGGATGCAGGTGAGTATCTGCA
TATGATGTCTGACGCTGGCATTCGCATCAAAGGAGAGTGAGATCGGTTTTG
TAAAAGATAACGCTTGTGAAAATGCTGAATTTCGCGTCGTCTTCACAGCGA
TGCCAGAGTCTGTAGTGTCAGATGATGACCGTACTCAAACATCGGGTTGAG
TATTATCTTACTGTTTCTTTACATAAACATTGCTGATACCGTTTAGCTGAA
ACGACATACATTGCAAGGAGTTTATAAATGAGTATCAATGAGTTAGAGTCT
GAGCAAAAAGATTGGGCGTTATCAATGTTGTGCAGATCCGGTGTCTTGTCT
CCATGCAGACATCACGAAGGTGTTTATGTAGATGAAGGTATAGATATAGAG
TCGGCATACAAA

>c-kit-mut REV COMP

CGAGCAGCAGCCCCTCCTCCCAGCGAACTCCCTCTGCGCGCCGGCCACGCC
CCTCATCGACTCCCCTCCCTCGCGCACGCACGGGTCTCGCTTCTTCCCGGC
GGCGTCTGGTACCTCGAGTGCGACAGGTTTGATGACAAAAAATTAGCGCAA
GAAGACAAAAATCACCTTGCGCTAAAGCTCTGTTACAGGTCACTAATACCA
TCTAAGTAGTTGATTCATAGTGACTGCATATGTTGTGTTTTACAGTATTAT
GTAGTCTGTTTTTTATGCAAAATCTAATTTAATATATTGATATTTATATCA
TTTTACGTTTCTCGTTCAGCTTTTTTATACTAAGTTGGCATTATAAAAAAG
CATTGCTTATCAATTTGTTGCAACGAACAGGTCACTATCAGTCAAAATAAA
ATCATTATTTGATTTCAATTTTGTCCCACTCCCTGCCTCTGTCATCACGAT
ACTGTGATGCCATGGTGTCCGACTTATGCCCGAGAAGATGTTGAGCAAACT
TATCGCTTATCTGCTTCTCATAGAGTCTTGCAGACAAACTGCGCAACTCGT
GAAAGGTAGGCGGATCCCCTTCGAAGGAAAGACCTGATGCTTTTCGTGCGC
GCATAAAATACCCTGATACTGTGCCGGATGAAAGCGGTTCGCGACGAGTAG
ATGCAATTATGGTTTCTCCGCCAAGAATCTCTTTGCATTTATCAAGTGTTT
CCTTCATTGATATTCCGAGAGCATCAATATGCAATGCTGTTGGGATGGCAA
TTTTTACGCCTGTTTTGCTTTGCTCGACATAAAAATATCCATCTACGATAT
CAGACCACTTCATTTCGCATAAATCACCAACTCGTTGCCCGGTAACAACAG
CCAGTTCCATTGCAAGTCTGAGCCAACATGGTGATGATTCTGCTGCTTGAT

AAATTTTCAGGTATTCGTCAGCCGTAAGTCTTGATCTCCTTACCTCTGATT
TTGCTGCGCGAG

Multiple sequence alignments

Reverse complement alignment

```
c-kit exp CCCTCCTCCCAGCGCCCTCCCTCTGCGCGCCGGCCACGCCCCTCCTCGCCTCCCCTCCCT
c-kit-wt  CCCTCCTCCCAGCGCCCTCCCTCTGCGCGCCGGCCACGCCCCTCCTCGCCTCCCCTCCCT
c-kit-mut CCCTCCTCCCAGCGAACTCCCTCTGCGCGCCGGCCACGCCCCTCATCGACTCCCCTCCCT
          **************..****************************.***.***********
c-kit exp CGCGCCCGCCCG
c-kit-wt  CGCGCCCGCCCG
c-kit-mut CGCGCACGCACG
          *****.***.**
```

Forward alignment

```
c-kit exp CGGGCGGGCGCGAGGGAGGGGAGGCGAGGAGGGGCGTGGCCGGCGCGCAGAGGGAGGGCG
c-kit-wt  ----------------------AGGCGAGGAGGGGCGTGGCCGGCGCGCAGAGGGAGGGCG
c-kit-mut ----------------------AGTCGATGAGGGGCGTGGCCGGCGCGCAGAGGGAGTTCG
                                **.***.****************************..**
orig      CTGGGAGGAGGG
c-kit-wt  CTGGGAGGAGGG
c-kit-mut CTGGGAGGAGGG
          ************
```

In yellow, the point mutations present in the c-kit-mut construct are highlighted. The forward alignment is a partial additional confirmation of the result obtained with the reverse complement alignment, even if it does not cover all the sequence. The results assure the accuracy of the three G4 sequences in both *c-kit-wt* and *c-kit-mut*.

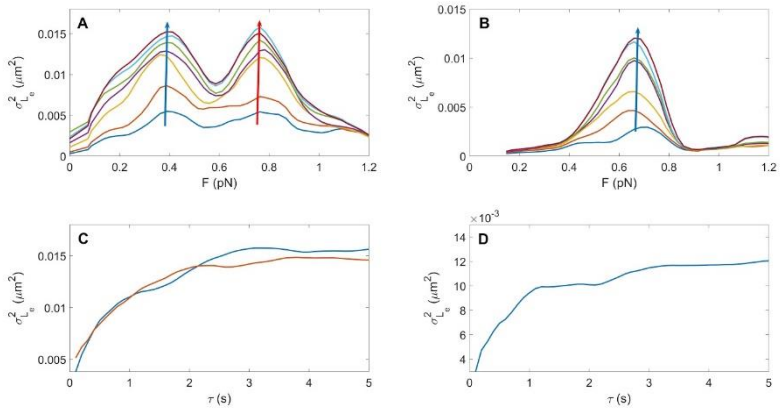

Figure S7. Panels A and B: DNA variance $\sigma^2 L_e$ measured as a function of the applied force F for increasing values of temporal windows τ (τ= 0.1; 0.2; 0.5; 1; 2; 4; 5 (s) from bottom to upper curves) used for data acquisition. Measurements acquired for *c-kit-wt* in KCl and imposed turns n_t=-40 or supercoiling density σ=-0.07. The vertical arrows indicate the force value for the $\sigma^2 L_e$ reported below in panel C and D. Panels C and D: corresponding DNA variance $\sigma^2 L_e$ reported at F= 0.39 pN and 0.75 pN (panel C) and F= 0.67 pN (panel D) as a function of the temporal window τ.

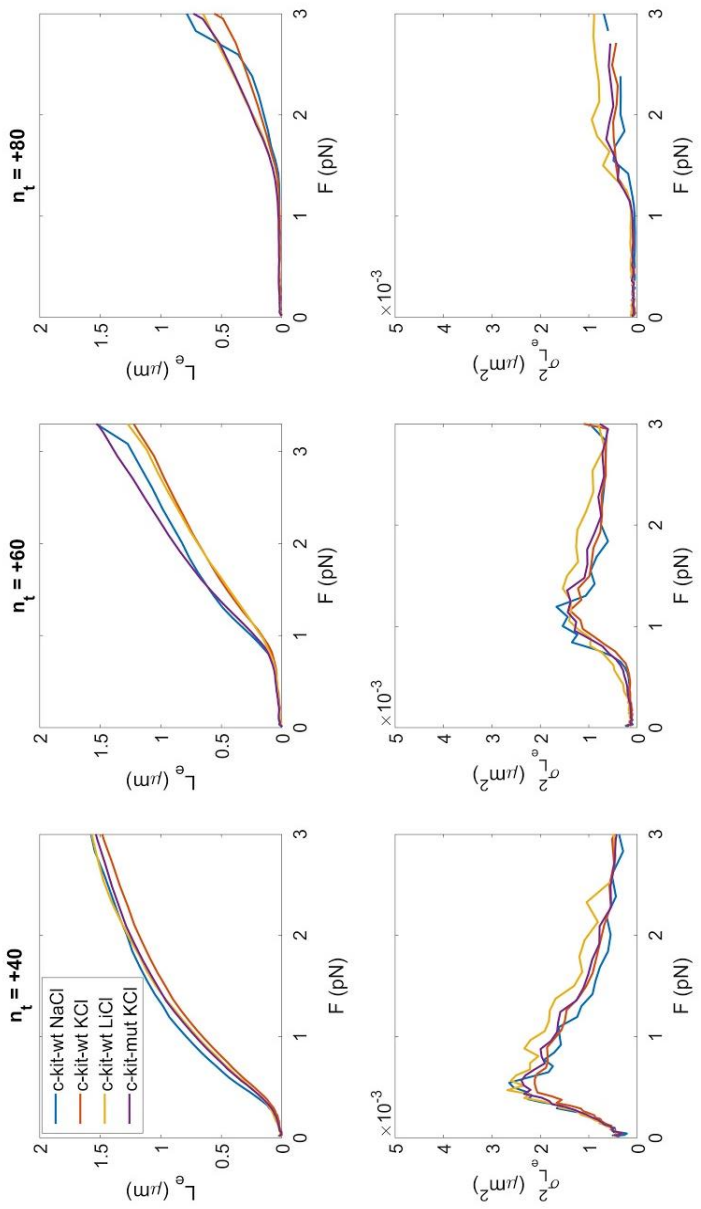

Figure S8. DNA extension (L_e) (upper panels) and corresponding variance ($\sigma^2 L_e$) (lower panels) measured for positive imposed turns, n_t, as a function of the applied force (F). Data obtained for three different positive n_t (n_t=+40, n_t=+60, n_t=+80, first, second and third column, respectively) for *c-kit-wt* and *c-kit-mut* in different conditions different conditions (in the presence of NaCl, KCl or LiCl), as indicated by the color code specified in the upper left inset.

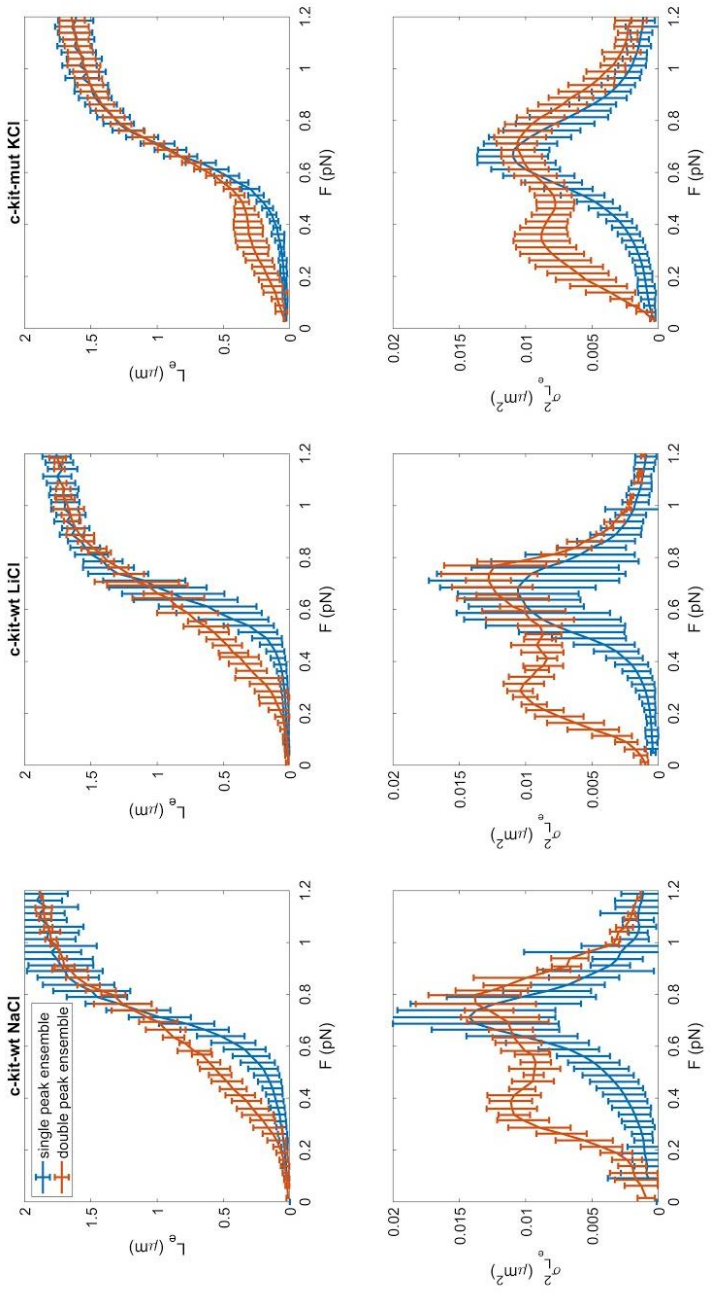

Figure S9. DNA extension (L_e) (upper panels) and corresponding variance ($\sigma^2 L_e$) (lower panels) measured at negative imposed turns, nt=-40, as a function of the applied force (F). Data taken for *c-kit-wt* and *c-kit-mut* in different buffers (NaCl and LiCl) as indicated by the upper labels.

2.8 Bibliography

1. Bochman M, Paeschke K, Zakian V. DNA secondary structures: stability and function of G-Quadruplex structures. *Nat. Rev. Genet.* **2012**, 13, 770-780.
2. Lightfoot HL, Hagen T, Tatum NJ, Hall J. The diverse structural landscape of Quadruplexes. *FEBS Lett.* **2019**, 593, 2083-2102.
3. Rhodes D and Lipps HJ. G-Quadruplexes and their regulatory roles in biology. *Nucl. Acids Res.* **2015**, 43, 8627-8637.
4. Zhang X, Zhang Y, Zhang W. Dynamic topology of double-stranded telomeric DNA studied by single-molecule manipulation in vitro. *Nucl. Acids Res.* **2020**, online ahead of print.
5. Maizels N and Gray LT. The G4 genome. *PLoS Genet.* **2013**, *9*, e1003468.
6. Biffi G, Tannahill D, McCafferty J, Balasubramanian *S.* Quantitative visualization of DNA G-Quadruplex structures in human cells. *Nat. Chem.* **2013**, 5, 182-186.
7. Du Z, Zhao Y, Li N. Genome-wide analysis reveals regulatory role of G4 DNA in gene transcription. *Genome Res.* **2008**, *18*, 233–241.
8. Varshney D, Spiegel J, Zyner K, Tannahill D, Balasubramanian S. The regulation and functions of DNA and RNA G-Quadruplexes. *Nat. Rev. Mol. Cell. Biol.* **2020**, online ahead of print.
9. You H, Guo S, Le S, Tang Q, Yao M, Zhao X, Yan J. Two-state folding energy determination based on transition points in nonequilibrium single-molecule experiments. *J. Phys. Chem. Lett.* **2018**, 9, 811-816.
10. Dhakal S, Yu Z, Konik R, Cui Y, Koirala D, Mao H. G-Quadruplex and I-motif are mutually exclusive in ILPR double-stranded DNA. *Biophys. J.* **2012**, *102*, 2575-2584.
11. Mitra J, Makurath MA, Ngo TTM, Troitskaia A, Chemla YR, Ha T. Extreme mechanical diversity of human telomeric DNA revealed by fluorescence-force spectroscopy. *Proc. Natl. Acad. Sci. USA.* **2019**, 116, 8350-8359.
12. Li W, Hou XM, Wang PY, Xi XG, Li M. Direct measurement of sequential folding pathway and energy landscape of human telomeric G-Quadruplex structures. *J. Am. Chem. Soc.* **2013**, 135, 6423-6426.
13. Koirala D, Dhakal S, Ashbridge B, Sannohe Y, Rodriguez R, Sugiyama H, Balasubramanian S, Mao H. A single-molecule platform for investigation of interactions between G-Quadruplexes and small-molecule ligands. *Nat. Chem.* **2011**, 3, 782-787.

14. Selvam S, Mandal S, Mao H. Quantification of chemical and mechanical effects on the formation of the G-Quadruplex and I-motif in duplex DNA. *Biochemistry* **2017**, 56, 4616-4625.
15. Mitra J and Ha T. Streamlining Effects of extra telomeric repeat on telomeric DNA folding revealed by fluorescence-forcesSpectroscopy. *Nucl. Acids Res.* **2019**, 47, 11044-11056.
16. You H, Wu J, Shao F, Yan J. Stability and kinetics of c-MYC promoter G-Quadruplexes studied by single-molecule manipulation. *J. Am. Chem. Soc.* **2015**, 137, 2424-2427.
17. Selvam S, Koirala D, Yu Z, Mao H. Quantification of topological coupling between DNA superhelicity and G-Quadruplex formation. *J. Am. Chem. Soc.* **2014**, 136, 13967–13970.
18. Wu CG and Spies M. G-Quadruplex recognition and remodeling by the FANCJ helicase. *Nucl. Acids Res.* **2016**, 44, 8742-8753.
19. Hou XM, Wu WQ, Duan XL, Liu NN, Li HH, Fu J, Dou SX, Li M, Xi XG. Molecular mechanism of G-Quadruplex unwinding helicase: sequential and repetitive unfolding of G-Quadruplex by Pif1 helicase. *Biochem. J.* **2015**, 466, 189-99.
20. Cheng Y, Tang Q, Li Y, Zhang Y, Zhao C, Yan J, You HJ. Folding/unfolding kinetics of G-Quadruplexes upstream of the P1 promoter of the human BCL-2 oncogene. *Biol. Chem.* **2019**, 294, 5890-5895.
21. Long X, Parks JW, Bagshaw C, Stone MD. Mechanical unfolding of human telomere G-Quadruplex DNA probed by integrated fluorescence and Magnetic Tweezers spectroscopy. *Nucl. Acids Res.* **2013**, 41, 2746-2755.
22. Mendoza O, Bourdoncle A, Boulé JB, Brosh RM Jr, Mergny JL. G-Quadruplexes and helicases. *Nucl. Acids Res.* **2016**, 44, 1989-2006.
23. Salerno D, Tempestini A, Mai I, Brogioli D, Ziano R, Cassina V, Mantegazza F. Single-molecule study of the DNA denaturation phase transition in the force-space. *Phys. Rev. Lett.* **2012**, 109, 118303.
24. Tempestini A, Cassina V, Brogioli D, Ziano R, Giovannoni R, Cerrito MG, Salerno D, Mantegazza F. Magnetic Tweezers measurements of the nanomechanical stability of DNA against denaturation at various conditions of pH and ionic strength. *Nucl. Acids Res.* **2013**, 41, 2009-2019.
25. Vlijm R, Torre J, Dekker C. Counterintuitive DNA sequence dependence in supercoiling-induced DNA melting. *PloS One* **2015**, 10, e0141576.
26. Neuman KC and Nagy A. Single-molecule force spectroscopy: optical tweezers, magnetic tweezers and atomic force microscopy. *Nat. Met.* **2008**, 5, 491-505.

27. Bai L, Santangelo TJ, Wang MD. Single-molecule analysis of RNA polymerase transcription. *Ann. Rev. Biophys.* **2006**, 35, 343-360.
28. Dulin D, Lipfert J, Moolman MC, Dekker NH. Studying genomic processes at the single-molecule level: introducing the tools and applications. *Nat. Rev. Gen*. **2013**, 14, 9-22.
29. Carrasco C, Pastrana CL, Aicart-Ramos C, Leuba SH, Khan S, Moreno-Herrero F. Dynamics of DNA nicking and unwinding by the RepC-PcrA complex. *Nucl. Acids Res.* **2020**, 48, 2013-2025.
30. Gahlon HL, Romano LJ, Rueda D. Influence of DNA lesions on polymerase-mediated DNA replication at single-molecule resolution. *Chem. Res. Toxicol.* **2017**, 30, 1972-1983.
31. Wang Y, van Merwyk L, Toensing K, Walhorn V, Anselmetti D, Fernàndez-Busquets X. Biophysical characterization of the association of histones with single-stranded DNA. *BBA-Gen. Subjects* **2017**, 1861, 2739-2749.
32. Marko JF and Neukirch S. Global force-torque phase diagram for the DNA double helix: structural transitions, triple points, and collapsed plectonemes. *Phys. Rev. E. Stat. Nonlin. Soft Matter Phys*. **2013**, 88, e062722.
33. Allemand JF, Bensimon D, Lavery R, Croquette V. Stretched and overwound DNA forms a pauling-like structure with exposed bases. *Proc. Natl. Acad. Sci. USA.* **1998**, 95, 14152-14157.
34. Liang J, Wu YL, Chen BJ, Zhang W, Tanaka Y, Sugiyama H. The C-Kit receptor-mediated signal transduction and tumor-related diseases. *Int. J. Biol. Sci.* **2013**, 9, 435-443.
35. Ceschi S and Sissi C. KIT promoter: structure, function and targeting. Quadruplex nucleic acid as targets for medicinal chemistry, *Ed. S. Neidle, Elsevier*, **2020**, online ahead of print.
36. Zorzan E, Da Ros S, Musetti C, Zorro Shahidian L, Nuno FRC, Bonsembiante F, Létard S, Gelain ME, Palumbo M, Dubreuil P, Giantin M, Sissi C, Dacasto M. Screening of candidate G-Quadruplex ligands for the human c-KIT promotorial region and their effects in multiple in vitro models. *Oncotarget* **2016**, 7, 21658-21675.
37. McLuckie KIE, Waller ZAE, Sanders DA, Alves D, Rodriguez R, Dash J, McKenzie GJ, Venkitaraman AR, Balasubramanian S. G-Quadruplex-binding benzo phenoxazines down-regulate c-KIT expression in human gastric carcinoma cells. *J. Am. Chem. Soc.* **2011**, 133, 2658-2663.
38. Rigo R, Palumbo M, Sissi C. G-Quadruplexes in human promoters: a challenge for therapeutic applications. *Biochim. Biophys. Acta* **2017**, 1861, 1399-1413.

39. Graeme AK, Gross P, Bockelmann U, Modesti M, Wuite GJL, Peterman EJG. Revealing the competition between peeled ssDNA, melting bubbles, and S-DNA during DNA overstretching using fluorescence microscopy *Proc. Natl. Acad. Sci. USA.* **2013**, 110, 3859-3864.
40. Baumann CG, Smith SB, Bloomfield VA, Bustamante C. Ionic effects on the elasticity of single DNA molecules. *Proc. Natl. Acad. Sci. USA.* **1997**, 94, 6185-6190.
41. Bouchiat C, Wang MD, Allemand J, Strick T, Block SM, Croquette V. Estimating the persistence length of a worm-like chain molecule from force-extension measurements. *Biophys. J.* **1999**, 76, 409-413.
42. Kriegel F, Ermann N, Lipfert J. Probing the mechanical properties, conformational changes, and interactions of nucleic acids with magnetic tweezers. *J. Struct. Biol.* **2017**, 197, 26-36.
43. Vologodskii A. Biophysics of DNA. *Cambridge: Cambridge University Press* **2015**.
44. Hänsel-Hertsch R, Di Antonio M, Balasubramanian S. DNA G-Quadruplexes in the human genome: detection, functions and therapeutic potential. *Nat. Rev. Mol. Cell Biol.* **2017**, 18, 279-284.
45. Bhattacharyya D, Mirihana Arachchilage G, Basu S. Metal cations in G-Quadruplex folding and stability. *Front. Chem.* **2016**, 4, 38.
46. Wu WQ, Zhang ML, Song CP. A comprehensive evaluation of a typical plant telomeric G-Quadruplex (G4) DNA reveals the dynamics of G4 formation, rearrangement, and unfolding. *J. Biol. Chem.* **2020**, 295, 5461-5469.
47. Bonnat L, Dautriche M, Saidi T, Revol-Cavalier J, Dejeu J, Defrancq E, Lavergne T. Scaffold stabilization of a G-Triplex and study of its interactions with G-Quadruplex targeting ligands. *Org. Biomol.Chem.* **2019**, 17, 8726-8736.
48. Stadlbauer P, Kührová P, Vicherek L, Banáš P, Otyepka M, Trantírek L, Šponer J. Parallel G-triplexes and G-hairpins as potential transitory ensembles in the folding of parallel-stranded DNA G-Quadruplexes. *Nucl. Acids Res.* **2019**, 47, 7276-7293.
49. Rigo R and Sissi C. Characterization of G4-G4 crosstalk in the c-KIT promoter region. *Biochemistry* **2017**, 56, 4309-4312.
50. Salsbury AM, Dean TJ, Lemkul JA. Polarizable molecular dynamics simulations of two c-kit oncogene promoter G-Quadruplexes: effect of primary and secondary structure on loop and ion sampling. *J. Chem. Theory Comput.* **2020**, 16, 3430-3444.
51. SantaLucia J Jr. A unified view of polymer, dumbbell, and oligonucleotide DNA nearest-neighbor thermodynamics. *Proc. Natl. Acad. Sci. USA.* **1998**, 95, 1460-1465.

52. Lane AN, Chaires JB, Gray RD, Trent JO. Stability and kinetics of G-Quadruplex structures. *Nucl. Acids Res.* **2008**, 36, 5482-5515.
53. IDT Oligo Analyzer, https://eu.idtdna.com/pages/tools/oligoanalyzer
54. Salerno D, Brogioli D, Cassina V, Turchi D, Beretta GL, Seruggia D, Ziano R, Zunino F, Mantegazza F. Magnetic tweezers measurements of the nanomechanical properties of the DNA in the presence of drugs. *Nucl. Acids Res.* **2010**, 38, 7089-7099.
55. Strick TR, Allemand JF, Croquette V, Bensimon D. Twisting and stretching single DNA molecules. *Prog. Biophys. Mol. Biol.* **2000**, 74, 115-140.
56. Strick TR, Dessinges MN, Charvin G, Dekker NH, Allemand JF, Bensimon D, Croquette V. Stretching of macromolecules and proteins. *Rep. Prog. Phys.* **2003**, 66, 1-45.
57. De Vlaminck I and Dekker C. Recent advances in magnetic tweezers. *Annu. Rev. Biophys.* **2012**, 41, 453-472.
58. Marko JF and Siggia ED. Stretching DNA. *Macromolecules* **1995**, 28, 8759-8770.
59. Kriegel F, Ermann N, Lipfert J. Probing the mechanical properties, conformational changes, and interactions of nucleic acids with magnetic tweezers. *Struct. Biol*. **2017**, 197, 26-36.
60. Lipfert J, Klijnhout S, Dekker NH. Torsional sensing of small-molecule binding using magnetic tweezers. *Nucl. Acids Res.* **2010**, 38, 7122-7132.
61. Herrero-Galan E, Fuentes-Perez ME, Carrasco C, Valpuesta JM, Carrascosa JL, Moreno-Herrero F, Arias-Gonzalez JR. Mechanical identities of RNA and DNA double helices unveiled at the single-molecule level. *J. Am. Chem. Soc.* **2013**, 135, 122-131.
62. Salerno D, Beretta G, Zanchetta G, Brioschi S, Cristofalo M, Missana N, Nardo L, Cassina V, Tempestini A, Giovannoni R, Cerrito MG, Zaffaroni N, Bellini T, Mantegazza F. Platinum-based drugs and DNA interactions studied by single-molecule and bulk measurements. *Biophys. J.* **2016**, 110, 2151-2161.
63. Cristofalo M, Kovari D, Corti R, Salerno D, Cassina V, Dunlap D, Mantegazza F. Nanomechanics of diaminopurine-substituted DNA. *Biophys. J,* **2019**, 116, 760-771.

Chapter 3

Targeted therapy affects Chronic Lymphocytic Leukemia cells mechanical properties

Enrico Buglione, Valeria Cassina, Federica Barbaglio, Lydia Scarfò, Domenico Salerno, Claudia Adriana Marrano, Doreen Biedenweg, Paolo Ghia, Oliver Otto, Francesco Mantegazza and Cristina Scielzo.

Submitted

3.1 Abstract

Chronic lymphocytic leukaemia (CLL) is an incurable B cell leukemia. CLL cells traffic and home between peripheral blood and tissues where they interact with a supportive microenvironment. These processes are affected by forces and by the capability of the cells to sense them. B lymphocytes need to modify their cytoskeleton and consequently their mechanical properties to migrate between a fluid environment (blood) to a significantly stiffer one (tissues) where they home. We studied B lymphocytes from patients with CLL and healthy donors using Atomic Force Microscopy in Force Spectroscopy mode and Real-Time Deformability Cytometry to measure the stiffness of the cells. A significant difference was found in CLL cells compared to healthy ones with or without the addition of the kinase inhibitor ibrutinib. Both methods showed that the drug can reverse the phenotype of CLL cells restoring the stiffness value to the one of healthy B cells which, on the contrary, are unaffected by ibrutinib. These results suggest that CLL cells are more prone to modify their mechanical properties depending on external cues. Furthermore, they show that the currently used targeted therapies have a striking effect on the mechanical properties of CLL cells, reverting them back to a healthy phenotype.

3.2 Introduction

Chronic Lymphocytic Leukaemia (CLL) is the most common leukemia in the Western world, affecting from 4 to 6 people out of 100,000 per year [1]. CLL is characterized by the progressive accumulation of mature monoclonal B lymphocytes in the Peripheral Blood (PB), Bone Marrow (BM) and secondary lymphoid organs [2]. The traffic of CLL cells between the PB and lymphoid organs is thought to be an active process involving a dynamic cytoskeletal remodelling [3] that contributes to disease maintenance and progression, creating niches where CLL cells can survive and proliferate. Once settled in the tissues, leukemic B cells form peculiar structures defined as "proliferation centers". Here they interact with the microenvironment that supports their survival and proliferation [4]. These mechanisms represent a small part of a complex scenario outlining a dynamic and heterogeneous disease, a complexity which probably is the reason why CLL still remains incurable. Deeper understanding of CLL has resulted in the development of new therapeutic approaches that have drastically improved patient outcomes. Among them, new targeted therapies (i.e. kinase and BCL2 inhibitors) [5,6] are taking over chemoimmunotherapy. Among others, the Bruton's Tyrosine Kinase (BTK) inhibitor ibrutinib [7,8] has been demonstrated to be an effective therapy leading to sustained responses. Ibrutinib promotes CLL cells mobilization from the tissues [9] to the PB where they lose the protective effect exerted by the microenvironment and eventually undergo apoptosis. However, the mechanism of action of the drug still

needs to be fully elucidated, along with the acquisition of resistance and relapse displayed by some patients [10].

It has become evident that intrinsic and extrinsic mechanical properties regulate cellular activities, such as cell morphology, proliferation, adhesion, migration, and trafficking. In the tissues, cells are continuously exposed to physical forces (i.e. shear stress and compression) and they adapt to those forces by modifying their behaviour and remodelling themselves and their microenvironment [11,12]. Cells are also able to "sense" [13-15] these forces through mechanoreceptors and to respond to them by exerting reciprocal actomyosin and cytoskeletal dependent generated forces through a process termed "mechanoreciprocity" [16]. Loss of mechanoreciprocity was shown to promote cancer progression in solid tumors; indeed, recent studies have demonstrated that solid tumor cells with higher migratory and invasive potential are softer than cells with lower migration and invasive potential [17,18]. However, how cell intrinsic mechanical properties might affect haematological cancer development and progression remains unclear. Just few reports studied the mechanical properties of leukemic cells [19,20], but none of these explored the CLL mechanical behaviour in relation to a targeted therapy.

Nowadays, many tools are used to study the stiffness of cells [21]. Although designed as an imaging tool [22-24], Atomic Force Microscopy in Force Spectroscopy (AFM-FS) mode represents a specific and accurate technique capable of measuring cellular elastic

modulus directly on living cells [25,26]. Due to its operating mechanism, AFM-FS is designed to study the stiffness of objects that are fixed on a substrate. However, it has also been applied to the study of circulating cells, by introducing experimental subtleties in the procedure (e.g. by coating the substrate or by employing a surface with microwells for housing the cells) [27-30]. In this configuration, AFM-FS measures the indentation of a microlever within the membrane of a cell as a function of applied force, obtaining the Young's Modulus (YM), which is expressed in Pascal (Pa), and quantifies the cell stiffness: the harder the sample, the larger the YM value recorded. On the other hand, it is possible to investigate the cell mechanical properties by means of Real-Time Deformability Cytometry (RT-DC), a novel high-throughput method for the mechanical characterization of single cells [31,32]. The technique is based on the hydrodynamic deformation of cells translocating through a microfluidic channel in a contact-free manner [33,34].

In the present work, we studied the mechanical properties of primary B lymphocytes isolated from 13 patients with CLL and 6 healthy donors by means of AFM-FS and RT-DC. We observed that the characteristic mechanical response of CLL cells differs significantly from the one of healthy B (HB) cells. Furthermore, both techniques were employed to investigate the effect of ibrutinib on the mechanical properties of B cells. We observed that *in vitro* the ibrutinib administration restores the mechanical values of elasticity, size and deformability of CLL cells to the measured values of HB lymphocytes. Finally, we followed up 3

patients during ibrutinib therapy to evaluate the mechanical behaviour of their leukemic cells under treatment. The results obtained were similar to the *in vitro* observations: the elastic YM of CLL cells was restored to values close to HB cells. All these data suggest that the mechanical properties of CLL cells are strongly associated with their malignant behaviour and the benefits of ibrutinib administration may also include the restoration of physiological cell stiffness.

3.3 Methods

Human Ethics Statement

Patients with CLL were diagnosed according to the updated National Cancer Institute Working Group (NCIWG) guidelines [35]. Peripheral blood (PB) samples were obtained after informed consent from patients who were either (i) untreated or off treatment for at least 6 months; or (ii) under Ibrutinib treatment. The study was approved by the Ospedale San Raffaele (OSR) ethics committee under the protocol VIVI-CLL entitled: "*In vivo* and *in vitro* characterization on CLL". The buffy coats study was approved by the Ospedale San Raffaele (OSR) ethics committee under the protocol Leu-Buffy_coat entitled: "Characterization of leukocyte subpopulations from buffy coats". Clinical and biological characteristics of CLL patients used for the experiments are reported in the Supplementary material (Table TS1).

Human primary sample purification

CD19 cells were negatively selected from fresh PB, BM and tonsils from patients or healthy donors using the RosetteSep B-lymphocyte enrichment kit (StemCell Technologies). HB cells were further negatively selected using B-lymphocyte enrichment kit (StemCell Technologies). The purity of all preparations was always higher than 99%, and the cells co-expressed CD19 and CD5 on their surface as assayed by flow cytometry (FC500; Beckman Coulter); preparations were virtually devoid of natural killer cells, T lymphocytes, and monocytes. After purification, cells were immediately plated on

coated (details are reported in Supplementary material) plates for measurements or frozen for further measures (fresh samples: n=6 patients and 6 HB; frozen samples: n=13 patients and 6 HB).

AFM-FS measurements

AFM-FS measurements were performed with a Nanowizard II (JPK Instruments, Berlin) equipped with a square-based pyramid probe (MLCT-BIO, cantilever E, 0.1 N/m nominal spring constant). All measures were done at room temperature in PBS with a standard cantilever holder for operation in liquid. The calibration of each cantilever spring constant was performed by thermal noise method [36,37] both in air and in PBS just before the measurements on every petri dish. For each patient and healthy donor, a minimum of 10 cells (1 plate) for fresh samples and a minimum of 45 cells (3 plates) for frozen samples was measured. Force-indentation curves were acquired with a maximum applied force of 1 nN, a 4 µm ramp length and a constant tip speed of 2 µm/s on a grid of 1x1 μm^2 with 4x4 points. The force-distance curves were corrected for the bending of the cantilever in order to obtain the force-indentation curves. The evaluation of cells elastic properties, described quantitatively through the YM, was obtained by force-indentation curves analysis with the Hertz-Sneddon contact mechanics, taking account the shape of the tip [38-41] (see Supplementary material). Each force-indentation curve was fitted by JPK data processing software (JPK Instruments) up to about 500 nm of indentation depth. To prevent significant changes in morphology or biochemistry of living cells, each petri dish was

measured within 2 hours. After measurements, a cell count with Trypan Blue (Merck, C8273) was performed and compared with a control petri dish kept in the incubator in the standard seeding medium. No significant difference in the death count was detected (see Fig. S1).

RT-DC measurements

Cell mechanical measurements have been carried out using an AcCellerator (Zellmechanik Dresden) with fluorescence module. Briefly, suspended cells are driven through the 300 µm long constriction with 20x20 μm^2 cross-section of a microfluidic chip and deform by shear and normal stresses [31,32]. Cell deformation is calculated from cell circularity in real-time for up to 1,000 cell/s, an analytical model enables derivation of the elastic modulus [33].

Frozen samples from both patients and healthy donors were centrifuged for 5 minutes at 250 g and re-suspended in CellCarrierB ($PBS^{-/-}$ without Ca^{2+} / Mg^{2+} and with 0.6% (w/v) methyl cellulose) to a final concentration of $5x10^5$ cell/ml. Measurements were performed at a total constant flow rate of 0.06 µl/s. A total of 10,000 cells per sample were captured. Analysis of cell shape was made with ShapeOut software (version 0.9.6) using an area ratio of 1.05 (ratio between raw area and area within contour) to ensure that cell contour represented cell periphery.

3.4 Results

Mechanical properties of lymphocytes measured by AFM-FS

The elastic modulus of single cells was assessed by means of AFM-FS, where a micrometer-sized cantilever was brought into contact with the cell surface. The relationship between force and cell deformation was recorded (force-indentation curve) and analyzed in order to extract cell mechanical properties such as stiffness, which was quantified by the YM value (Fig. 1). We evaluated the uniformity of the response to AFM-FS of the B lymphocytes coming from patients with CLL or healthy donors by comparing fresh cells versus thawed cells in 5 patients and 5 healthy donors (Supplementary material and Fig. S2-S4). No significant differences were observed in cell viability and YM values, therefore we included thawed cells in subsequent analyses. We analyzed a total of 13 patients with CLL and 6 healthy donors, considering both fresh and thawed samples. In Figure 2, we report the YM measures of CLL cells and HB cells. The distributions clearly show that the YM of CLL cells (432 [365-489] Pa) is systematically lower than the YM of HB cells (432 [365-489] Pa), ($p<0.0001$), suggesting that CLL cells have different mechanical properties if compared to HB cells. See Supplementary Information for the details of the statistical analysis.

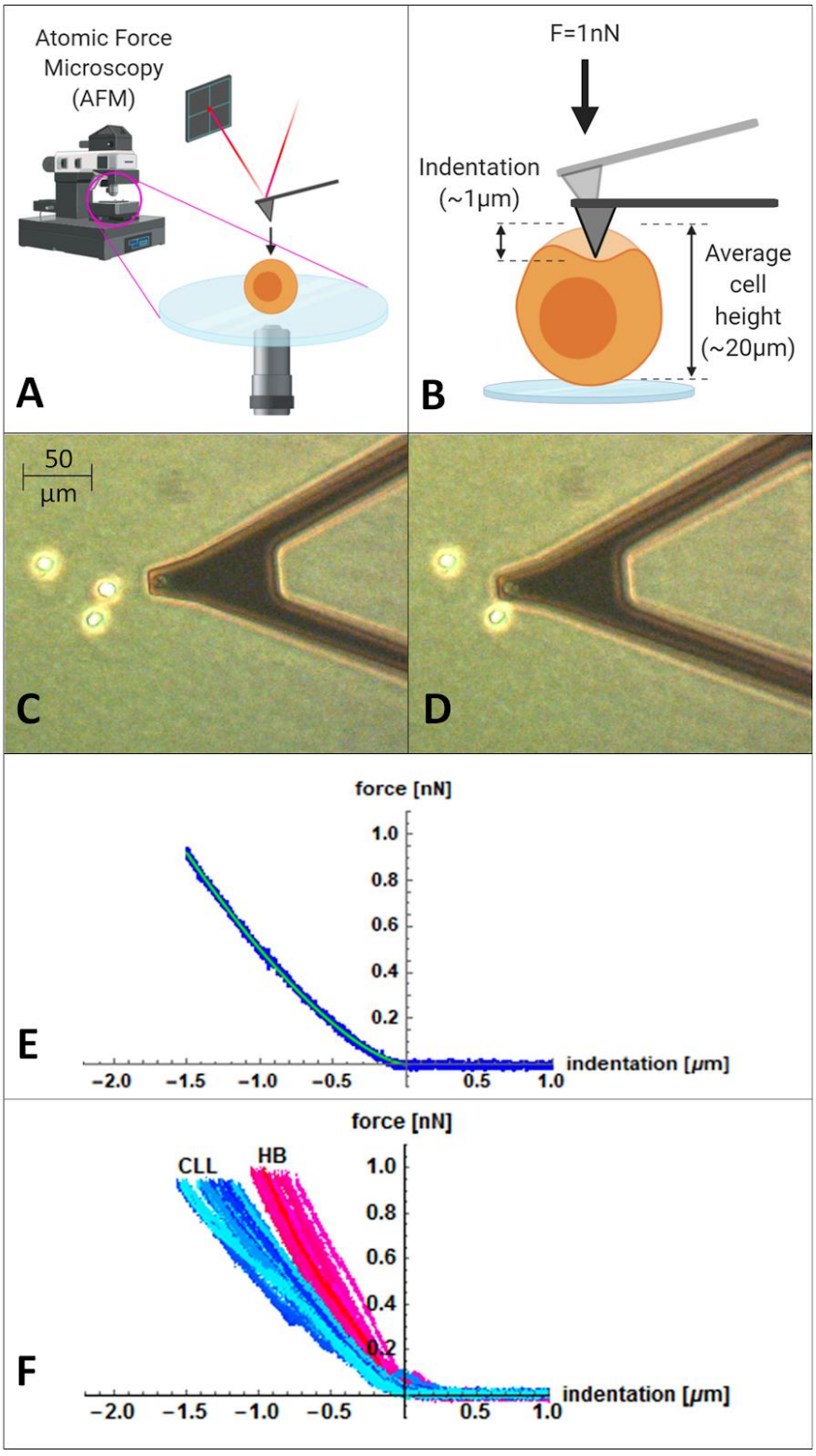
Atomic Force
Microscopy
(AFM)
A
F=1nN
Indentation
(~1µm)
Average
cell
height
(~20µm)
B
50
µm
C
D
force [nN]
1.0
0.8
0.6
0.4
0.2
−2.0
−1.5
−1.0
−0.5
0.5
1.0
indentation [µm]
E
force [nN]
CLL
HB
1.0
0.8
0.6
0.4
0.2
−2.0
−1.5
−1.0
−0.5
0.5
1.0
indentation [µm]
F

Figure 1. Schematic representation of the AFM-FS measurement on B lymphocytes. (A) Schematic representation of a standard AFM setup. (B) A micronmeter-sized cantilever applies a controlled external force on a single cell and the consequent indentation is recorded. Optical images from the AFM field of view (C) of the cantilever approaching a B lymphocyte (D) and of the contact between the cell and the cantilever during a measurement. (E) Representative AFM-FS force-indentation curve of a leukemic cell, where the blue dots represent the experimental data and the yellow line is the best fit of the Hertz-Sneddon model to the data having the YM as free fitting parameter. (F) Representative ensemble of the curves from all the measurements on a single cell from a patient with CLL (blue lines) and a HB (red lines).

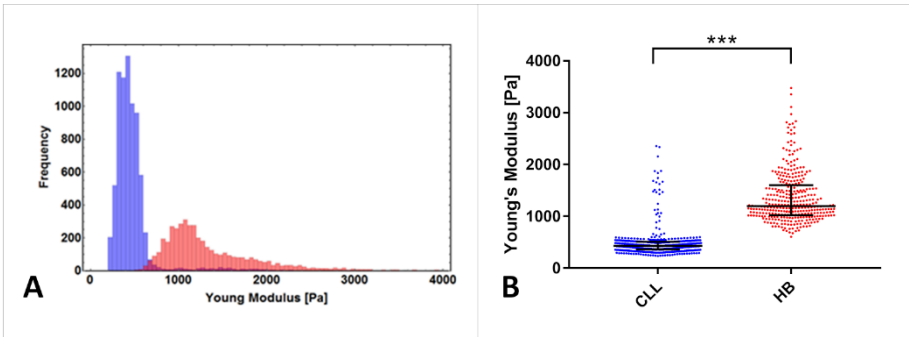

Figure 2. AFM-FS measurements on B lymphocytes isolated from patients with CLL and HB donors. Statistical distributions of YM values acquired by AFM-FS: (A) histograms including all the measurements acquired on the single cells (CLL patients: blue bars; HB donors: red bars); (B) swarm plots of the data reported in panel A: every dot represents the median value measured on a single cell. Data acquired over 599 B lymphocytes from the PB of 11 patients with CLL (blue) and 348 B lymphocytes from 6 HB (red) respectively from both fresh and thawed samples.

Both analyzed populations (CLL or healthy) were isolated from PB, thus they are representative of circulating B lymphocytes. In order to investigate whether there could be a different response in the range of stiffness depending on *in vivo* lymphocyte mobility, we measured the YM of circulating cell types in comparison to resident cell types (i.e. isolated from BM (CLL) or tonsils (healthy)). In detail, via AFM-FS we

measured the stiffness of B lymphocytes isolated from PB or BM (CLLs), B lymphocytes isolated from healthy PB or tonsils, and T lymphocytes (HT) from healthy PB (unrelated individuals). As shown in the histograms (Fig. 3), circulating B lymphocytes (PB) and tissue resident B lymphocytes (BM) obtained from patients with CLL showed comparable median values of YM, 471 [401-522] Pa and 694 [383-1,598] Pa, respectively. The YM values of all lymphocytes isolated from healthy donors exhibited analogous median values: 1,259 [1,169-1,322] Pa (Tonsillar HB), 1,393 [1,126-1,629] Pa (PB HT) and 1,365 [1,048-1,841] Pa (PB HB). We identified an arbitrary threshold (800 Pa) above which we could not find any significant median YM values for CLL cells, and below which the YM of HB cells virtually never drops. These results confirm that a consistent difference exists in the mechanical properties of CLL cells vs. HB cells. Moreover, the data indicate that the difference observed is independent from the anatomical distribution of the lymphocyte.

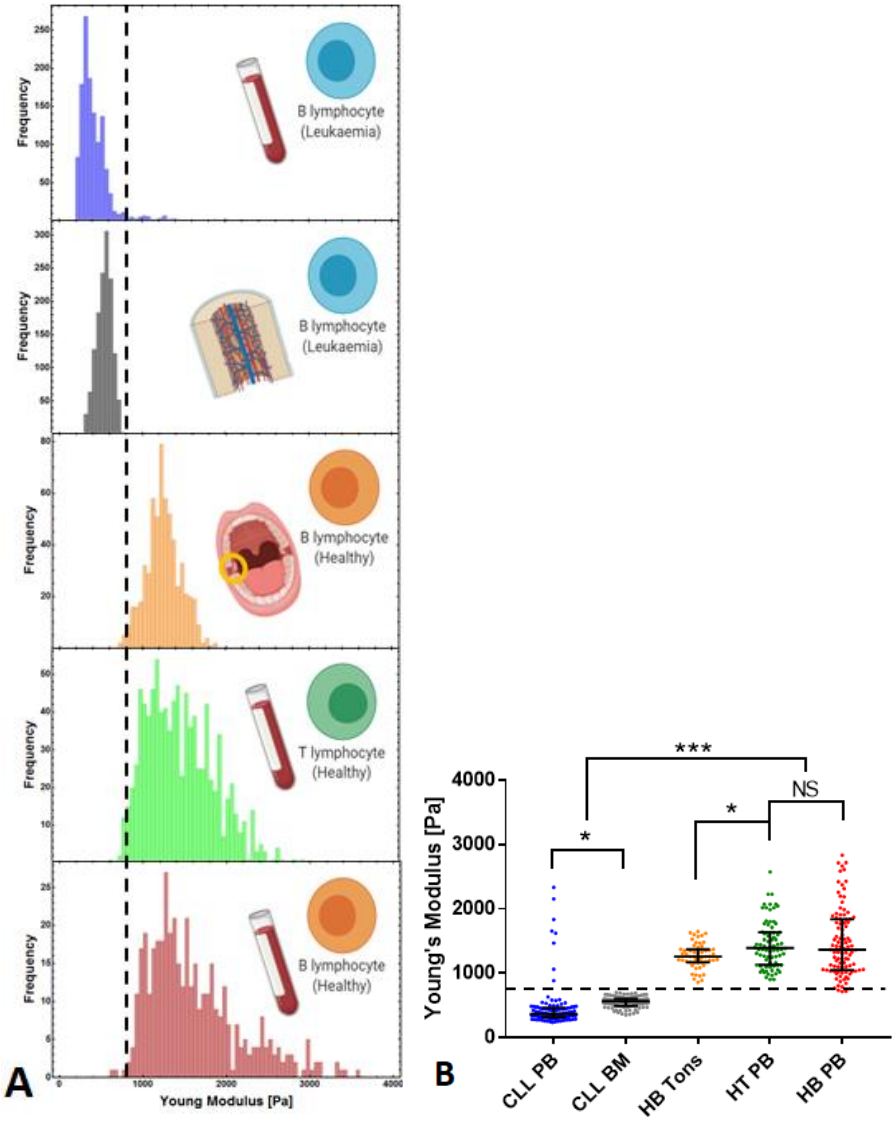

Figure 3. Distributions of YM for different blood cells isolated from distinct compartments. Statistical distribution of YM values acquired by AFM-FS for: B lymphocytes from PB of 2 representative patients with CLL (blue, 107 cells); B lymphocytes from BM of 2 patients with CLL (gray, 106 cells); tonsil-resident B lymphocytes from 2 HB cells (orange, 55 cells); T lymphocytes from PB from 2 HB cells (green, 78 cells); B lymphocytes from PB of 2 representative HB cells (red, 99 cells). (A) The histograms include all the measurements acquired on the single cells. (B) Swarm plots of the data reported in panel A: every dot represents the median value measured on a single cell. The threshold fixed at 800 Pa (black dashed lines) is a discriminating value of the measured YM between healthy and CLL cells.

CLL cells mechanical properties can be tuned by drugs in AFM-FS measurements

In order to further characterize the intrinsic difference in the mechanical properties between CLL cells and HB cells, we checked whether the stiffness of the cells could be modulated by adding *in vitro* specific inhibitors, known to affect cell elasticity in other models.

We first measured the YM in response to fasudil treatment *in vitro.* Fasudil is a Rho-Kinase inhibitor which increases the cellular YM, as shown in oncogene-mediated reprogrammed cells [42]. It impairs phosphorylation of myosin light chain in vascular smooth muscles, resulting *in vivo* in the prevention of muscular contraction [43]. As reported in Figure 4A-right panel, the median YM value observed for HB cells was 1,477 [1,209-1,898] before the treatment and 1,963 [1,630-2,323] Pa after the treatment. In the case of CLL cells, the median YM value measured was 471 [401-522] Pa before the treatment and 694 [383-1,598] Pa after the treatment (Fig. 4A-left panel). The measurements acquired for CLL cells after the treatment revealed a modification effect on the YM exerted by the inhibitor. In particular, the increase of the YM is extended to the 47% of the total number of cells (17 out of 36 cells) that show an elastic modulus value above the threshold (Fig. S6). This tendency explains the great variability reported in the YM measurements in Figure 4A. As expected, the effect of fasudil induced an increase in the overall YM of cells, both for CLL and HB cells.

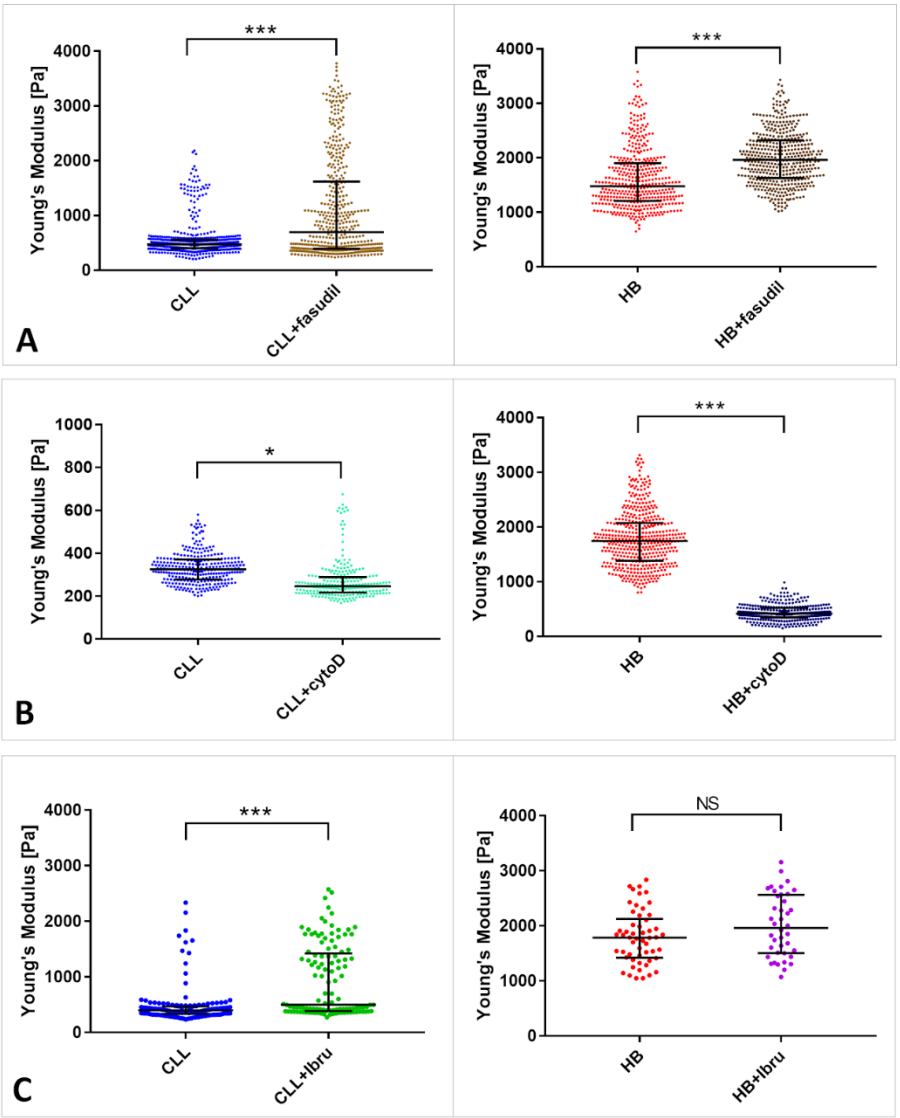

Figure 4. AFM-FS measurements of the in vitro effect of drugs on the YM of CLL cells and HB cells. Statistical distribution of YM values acquired by AFM-FS for B lymphocytes from: (A-left panel) one patient with CLL before (54 cells) and after (36 cells) the treatment with fasudil; (A-right panel) one HB before (43 cells) and after (35 cells) the treatment with fasudil; (B-left panel) one patient with CLL before (22 cells) and after (18 cells) 40 min of treatment with cytochalasin D; (B-right panel) one HB before (26 cells) and after (18 cells) 40 min of treatment with cytochalasin D; (C-left panel) cells from 3 different patients with CLL before (158 cells) and after (121 cells) 4h of treatment with ibrutinib; (C-right panel) cells from 1 HB donor before (54

cells) and after (50 cells) 4h of treatment with ibrutinib. Every dot represents a single measurement acquired on the single cells.

To evaluate the effect of a drug with an opposite behaviour to fasudil, we used mycotoxin cytochalasin D, known to prevent actin monomer polymerisation [44,45] thus decreasing cell YM, as previously observed in other cell types [46,47]. We were able to confirm that the outcome of the treatment with cytochalasin D, monitored on both CLL and HB cells, is strongly dependent on the timing of administration. Thus, cytochalasin D was administered after cell seeding on coated plates and maintained in solution during AFM-FS measurements, allowing the time-evolution observation of the effects (Fig. S7). In Figure 4B, we report the AFM-FS measurements of the YM performed about 40 min after the addition of the drug. The data show for HB cells a median YM value of 1,744 [1,411-2,063] Pa before the treatment and 418 [364-549] Pa after the treatment, and a median value of 325 [265-354] Pa before the treatment and 246 [206-253] Pa after the treatment for CLL cells. Thus, the effect of cytochalasin D is appreciable on HB cells, which display a significant decrease in the YM ($p<0.0001$). On the contrary, the effect of the drug seems to be much more limited on CLL cells YM ($p<0.05$). This different behaviour may depend on the intrinsic elastic modulus of CLL cells, which cannot be further reduced.

Next, we analysed whether the therapeutic effect of the kinase inhibitor ibrutinib [7,8] could have an impact on the mechanical properties of CLL cells. Ibrutinib was administered for 4 hours at concentrations of 1 or 10 µM: no significant differences were observed

on the mechanical properties of CLL cells comparing the two concentrations (see Supplementary material, Fig. S8). Thus, all experiments were performed at a final concentration of 10 μM. As reported in Figure 4C-left panel, we observed an increase of the general YM of the CLL cells, which moved from 399 [282-445] Pa (before treatment) to 497 [393-1,452] Pa (after treatment). The increase in elastic modulus was paralleled by an increase of the percentage of cells characterized by a higher value of YM. In Fig. S9, cumulated in Fig. 4C-left, we report the results relative to cells isolated from 3 different patients with CLL: before treatment, cells with YM above the defined threshold of 800 Pa, discriminating HB cells from CLL cells, accounted for 4%, 11% and 5% for patient #7, #10 and #12 respectively, while after treatment with ibrutinib they became 50%, 38% and 43%. The remaining fraction of the leukemic cells seems not to be affected by the treatment. On the contrary, HB cells were not affected by the drug, showing a YM value of 1,785 [1,425-2,187] Pa (before treatment) and 1,961 [1,458-2,441] Pa (after treatment) ($p>0.1$) (Fig. 4C-right panel).

Mechanical properties of lymphocytes measured by RT-DC

In order to assess the mechanical properties of B lymphocytes under different environmental constraints, we performed RT-DC measurements (Fig. 5), which allows to determine the elastic parameters of cells in suspension, resembling the conditions of circulating lymphocytes.

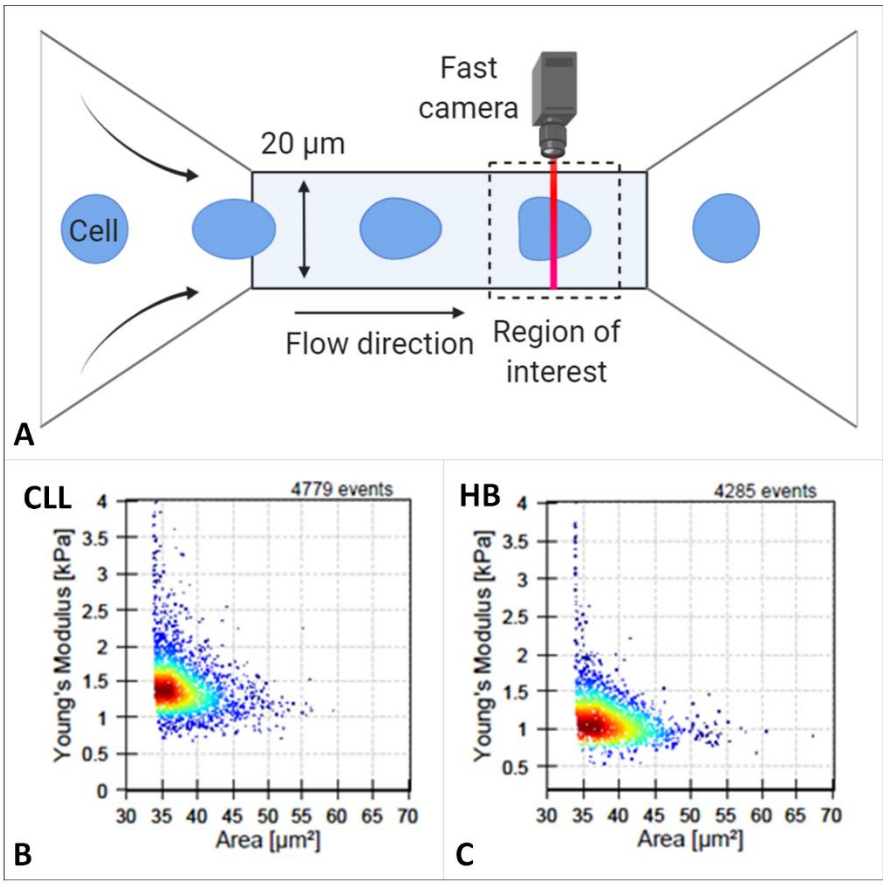

Figure 5. Cell mechanical measurements by RT-DC. (A) The sketch shows a microfluidic channel with a central constriction of 20x20 µm^2 cross-section and 300 µm length. Suspended cells are driven by a syringe pump through the constriction and they are deformed by hydrodynamic interaction only. A software algorithm determines cell perimeter and cell area and calculates in real time its deformation based on its circularity. Representative scatter plots from a CLL (B) and a HB (C) are shown.

In particular, the RT-DC technique evaluates the deformation that a cell undergoes when subjected to the pressure exerted by a constant flow rate inside a 20 µm x 20 µm micrometer-sized channel instead of measuring a cell that is adhering to a solid substrate (Fig. 5) [33,34]. In

contrast to AFM-FS, RT-DC measures the elasticity of a single cell considering its volume deformation as a function of the hydrodynamic stresses acting on the cell surface. We measured the YM and size of B lymphocytes from 6 patients with CLL and 5 HB donors. The median YM value for the HB cells was 999 [938-1,064] Pa, while for CLL cells 1,252 [1,222-1,299] Pa (Fig. 6A-left panel), showing a significantly different YM ($p<0.005$) in both samples. RT-DC shows different results if compared to AFM-FS data (Fig. 2B): we observed a higher YM value in CLL cells when compared to HB cells. However, it is worth noting that HB cells maintain the same range of elasticity with both techniques (from 936 to 1,785 Pa). This could possibly be explained by the increased capacity of CLL cells versus HB cells in modifying their mechanical properties depending on the external environmental cues they are exposed to.

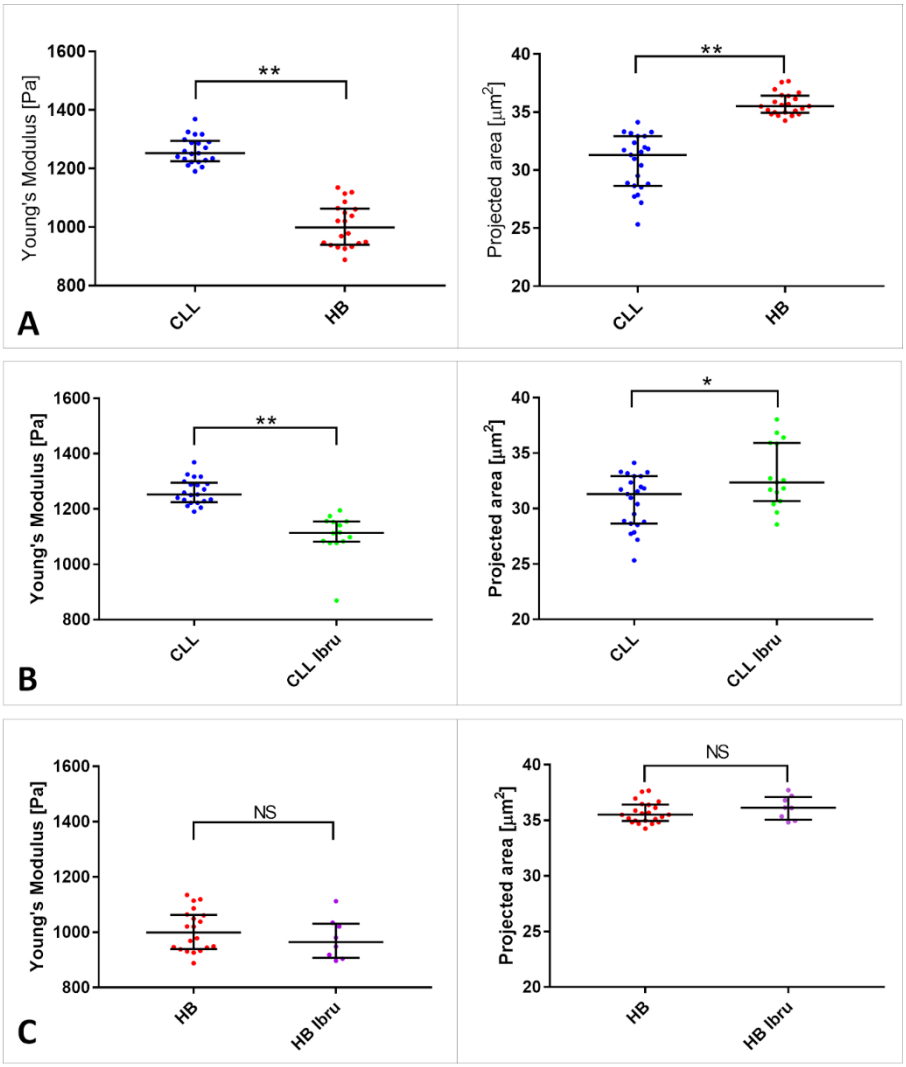

Figure 6. RT-DC measurements on B lymphocytes isolated from patients with CLL and HB donors. Statistical distribution of YM (left column) and projected cell area values (right column) measured by RT-DC for B lymphocytes. (A) Data acquired from 6 patients with CLL (blue) and 5 HB donors (red). (B-C) Measurements acquired before and after 4h of treatment with ibrutinib from 6 patients with CLL (B), and 5 HB donors (C) from the same individuals of panel A. Each dot represents the median of the total number of cells measured for an individual (from 2,000 to 6,000 cells) in a single experiment.

Thanks to RT-DC technique, we were also able to measure and compare the size of the cells analyzed. In Figure 6A-right panel, we report the median projected cell area measured for each patient with CLL or healthy donor. The data shows a reduction of the dimensions of leukemic cells (31 [28-32] μm^2) with respect to healthy B lymphocytes (35 [34-36] μm^2).

Next, we analyzed the effect of ibrutinib also by RT-DC. The results revealed that CLL cells, after a 4 hour-treatment with ibrutinib, exhibit a decrease in YM (Fig. 6B-left panel) and an increase in size (Fig. 6B-right panel) approaching the values of HB cells. Also in this case, both the YM and the dimension of HB cells resulted unaffected by the treatment (Fig. 6C). Indeed, the median YM value of CLL cells decreased from 1,252 [1,222-1,299] to 1,114 [1,077-1,156] Pa upon treatment, while the median value of HB cells substantially remained unchanged at 999 [938-1,064] before treatment and 964 [904-1,034] Pa after treatment. Taking into account the size, the median area of CLL cells was increased by about 1.2 μm^2 upon treatment with respect to untreated cells from the same patients, while HB cells resulted unaffected. Taken together, AFM-FS and RT-DC findings indicate that ibrutinib is able to revert CLL cells phenotype towards the healthy condition though not affecting the mechanical properties of HB lymphocytes.

Ibrutinib affects the mechanical properties of CLL cells *in vivo*

Finally, to investigate the effect of ibrutinib in the clinical settings, we evaluated with AFM-FS the YM of CLL cells obtained from 3 patients

under ibrutinib treatment (4, 8 and 9 weeks respectively). As shown in Figure 7, a significant number of cells (ranging from 30 to 40%) in each patient displayed an increase of the YM, reaching values within the range of HB cells. In particular, for Patient#12 (Fig. 7, panel A) the measurements acquired from the cells isolated before the clinical treatment revealed that only 3/51 cells (5.8%) showed YM values above the defined threshold, and after 4 weeks of treatments their number increased to 22/54 cells (40.7%). A similar trend was observed when monitoring cell stiffness after clinical treatment at later time points. The cells with YM above the threshold were, for Patient #13, 4/56 (7.1%) before treatment, becoming 19/54 (35.2%) after 8 weeks of therapy (panel B); for Patient #2, 0/40 (0%) becoming 14/48 (29.1%) after 9 weeks of treatments (panel C).

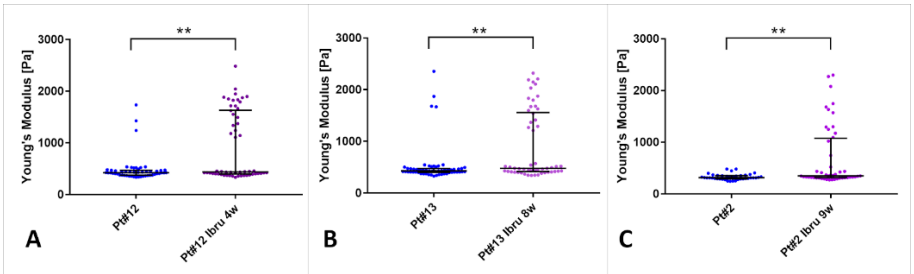

Figure 7. Effect of the clinical treatment with ibrutinib on cellular mechanical properties. YM values acquired by AFM-FS on cells from 3 different CLL patients before (left swarm plots) and after (right swarm plots) the treatment. (A) 4 weeks (Pt#12), (B) 8 weeks (Pt#13) and (C) 9 weeks (Pt#2) of treatment with ibrutinib. Every dot represents the median value of all the measurements acquired on a single cell.

3.5 Discussion

In the present work we studied the mechanical behaviour of leukemic in comparison to healthy lymphocytes, a poorly explored field [19,48]. As CLL is a dynamic disease in which leukemia cells traffic between the bloodstream and the tissues where they home, we hypothesized that CLL cells could rearrange frequently the cytoskeleton to favour cell infiltration and migration into the tissue thus affecting their intrinsic mechanical properties. To this purpose, two different techniques have been employed to study the cell stiffness: AFM-FS and RT-DC. Li and colleagues (2016) [48] showed that AFM-FS allows to measure the stiffness of primary B lymphocytes deposited on a flat surface. The reported YM values are consistent with our results. As for RT-DC, we previously demonstrated to be a proper tool to evaluate the mechanical properties of cells growing in suspension, as in the case of B lymphocytes [49].

By using AFM-FS, we observed that almost all cells from patients with CLL were confined to a range of YM between 375 and 580 Pa. Conversely, HB lymphocytes showed a higher YM value above 1,000 Pa, never dropping below 800 Pa. These results seem to be in contrast to the findings reported by Zheng *et al.* [19]. These authors used AFM-FS to measure the YM of lymphocytes, coming to the conclusion that CLL cells show YM values higher than healthy cells. However, in their case, lymphocytes were studied as a whole population, while we restricted the analysis to only the B lymphocyte population.

The consistent difference between the mechanical behavior of healthy and leukemic cells we observed by AFM, was further investigated on suspended cells using RT-DC. The outcome of RT-DC measurements confirms the clear difference in YM between healthy and leukemic cells (1,000 Pa versus 1,250 Pa respectively), although demonstrating a different behaviour with respect to AFM-FS results. Indeed, the YM of CLL cells measured with RT-DC was higher than the one of HB lymphocytes.

The apparently opposite results obtained with the two different techniques may be explained by the distinct environmental conditions, from a mechanical point of view, tested in the two experimental procedures. In detail, for the AFM-FS measurements the cells adhere to a rigid substrate, a condition which resembles the tissue environment, while for RT-DC experiments the cells are suspended in a flow under a shear stress, a situation which much more closely mimics the bloodstream. In reality, B lymphocytes continuously recirculate between blood and lymphoid tissues, experiencing and adapting to very different external mechanical stimuli [2]. The process of migration from a fluid environment (i.e. blood) to a significantly more viscous one, as the tissue (i.e. BM and LN), induces in the cell a significant structural rearrangement, which can modify both cell stiffness and size. Our findings intriguingly suggest that CLL cells, unlike healthy lymphocytes, drastically modify their mechanical properties depending on the external environmental cues they are exposed to. Moreover, to fully interpret the results, we have to consider also the

role played by the different distribution of force applied by the two techniques, which could lead to different but coherent responses. From a physical point of view, we can describe a cell as a non-Newtonian fluid, which returns YM values that could depend on time and strength of the force-application, when subjected to a mechanical stress [50]. In AFM-FS the force is applied in a point-like fashion every 4 seconds at a specific region of the cell surface, while in RT-DC the hydrodynamic forces are uniformly applied across the whole cell membrane in the time scale of microseconds. Since the cell is a complex and dishomogeneous system, comprising several parts with different viscoelastic characteristics, it is not unexpected that the RT-DC would be more sensitive than AFM-FS to bulk elasticity.

In this work, we studied the effect of the targeted therapy ibrutinib on the elastic modulus of CLL cells considering the known role of the drug in inducing their mobilization from the tissues. Both AFM-FS and RT-DC results indicate that: (i) B cells from healthy donors exhibit an unaltered mechanical fingerprint, suggesting an overall lack of effect in this respect; (ii) leukemic cells recover the intrinsic range of YM values of HBs. The same was observed for the size of leukemic cells, which increased to the dimension of HB cells upon ibrutinib treatment (see schematic representation in Fig. 8). Together the data suggest that the drug is able to restore the native mechanical/structural phenotype of leukemic lymphocytes. This evidence goes in the same direction of previously reported data obtained for two other types of leukemia, namely acute lymphoblastic leukemia and acute myeloid

leukemia [20], where AFM-FS analysis showed that chemotherapy treatments renormalize the stiffness of the malignant cells.

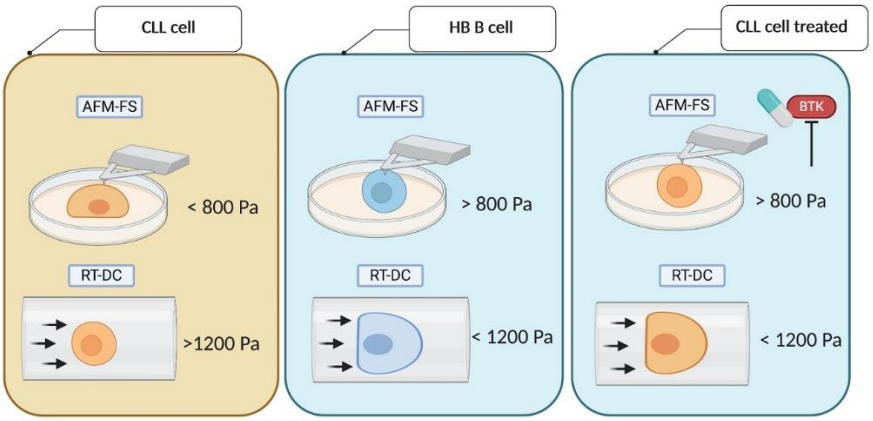

Figure 8. Schematic representation of B lymphocytes mechanical properties.

In order to corroborate our findings, we investigated the effect of the administration of ibrutinib *in vivo*. We observed that the mechanical properties of B cells from patients under treatment are fully comparable with the results obtained *in vitro*, with a substantial increase in the percentage of cells displaying YM values in the range of HB cells. The role played by ibrutinib in the regulation of the cellular mechanical properties could impact the mechanoreciprocity of leukemic cells, limiting their capacity to sense the surrounding environment and its substrates. Of note, the results obtained *in vitro* are far from being a faithful representation of what is occurring *in vivo* as also the modifications of the tissue mechanical properties must be

taken into account. One has to consider that the lymphoid tissues are likely changing their mechanical phenotype during leukemia progression and upon therapy, and this aspect warrants further investigations to fully understand CLL cells extrinsic mechanical properties.

3.6 Conclusions

In conclusion, in this study we demonstrate for the first time that a targeted therapy is able to normalize the mechanical properties of CLL cells while not affecting those of healthy B cells. Our findings suggest that the pathological alteration of the intrinsic mechanical properties could be a possible mechanism of the CLL cells retention within the tissue and could be reverted by effective therapies. Detailed studies aimed at dissecting the relation between the mechanical properties of CLL cells and the signaling pathways involved are warranted in the future to define new potential therapeutic targets and strategies focused on the normalization of the mechanical fingerprints of the leukemic cells.

3.7 Supplementary methods

Cell seeding

Both fresh and thawed primary cells were plated on adapted 40mm petri dish (TPP, 93040) coated o/n with poli-L-ornitine solution 0.01% (Merck) in Roswell Park Memorial Institute (RPMI) medium supplemented with 10% Fetal Bovine Serum (FBS) for 2 hours in standard incubator with a concentration of $2x10^5$ cells/plate. After careful removal of medium, cells were washed twice with Phosphate Buffered Saline (PBS). Measures were carried out in PBS supplemented with Ca^{2+} and Mg^{2+} (Thermo Fisher Scientific).

Statistical analysis

Statistical analyses were performed with Mann-Whitney U test, considering statistically significant a value of $p<0.05$ (*), and consequently $p<0.005$ (**), $p<0.0005$ (***). When not specified elsewhere, all the data were expressed as the median combined with the interquartile range (i.e. from 25th to 75th percentile), both in the text (using the notation: median [25th percentile-75th percentile]) and in the graph fences.

3.8 Supplementary results

Control experiments on cell viability

In order to exclude that cell death could affect our survey, a control petri dish was kept in the incubator in the same conditions of the cells under measure. No significant differences were found in terms of cell viability at the end of the measurement window (maximum 2h, Fig. S1). However, beyond this temporal window both HB and CLL viability started to decrease steeply, reducing drastically the number of possible measurements for every patient.

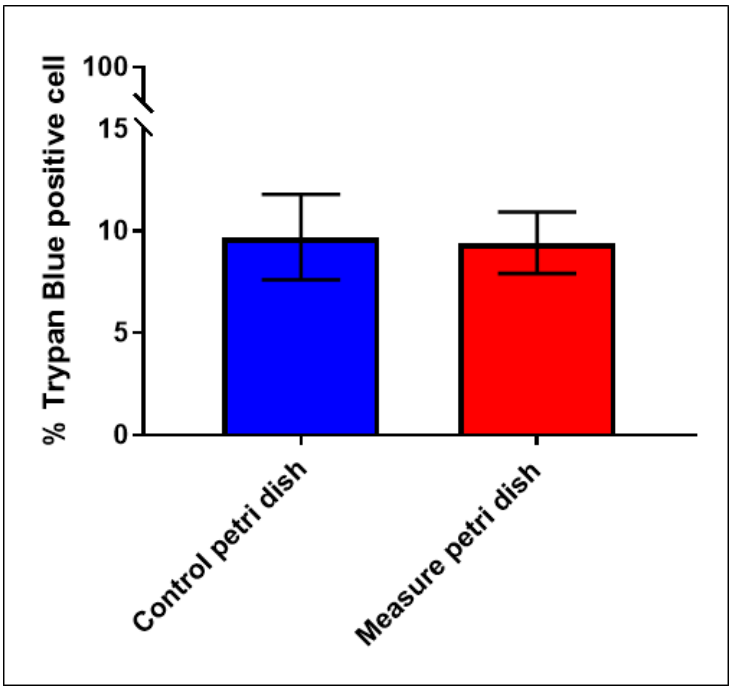

Figure S1. Cell viability count. Histogram of the percentage of dead cells (CLL and HB) for the petri dish before (blue) and after (red) the AFM-FS measurement showing

that measurements do not affect the cell viability. The fences represent the standard deviations of the measured data.

AFM-FS data analysis

The most common model describing the elastic properties of cells is the Hertz model corrected by Sneddon considering the tip geometry that affects the contact area. Following this model, the relation between the loading force F and the resulting indentation δ for a pyramidal tip is:

$$F=2/\sqrt{2}\cdot\tan\beta\cdot E'\cdot\delta^2$$

Where β is the face tip angle and E' is the reduced Young's Modulus $E'= E_{cell}/(1-\mu_{cell}^2)$ that takes into account the cell Poisson ratio μ_{cell} usually assumed to be 0.5.

Tips with different shapes are available on the market for AFM-FS measurements, and recently a lot of authors choose the colloidal probes for the investigation of cell stiffness. In this work, we performed stiffness measurements with pyramidal probes in order to have an easier experimental strategy. Indeed, several attempts to acquire reproducible force-indentation curves on B lymphocytes with colloidal probes (Novascan, CT.AU.SA.SN, on 0.06N/m cantilevers) and tipless cantilever (Bruker, MLCT-O10) resulted in contact point buckling and cell sliding.

It is also worth noting that the absolute value of Young's Modulus is difficult to determine. For this reason, no matter the model applied,

all results should be compared to a reference sample. Here we used as reference sample B lymphocytes from healthy donors and cells treated with drugs of known effect.

The mechanical properties of a complex system such as a cell were described through several theoretical models returning different values of the mechanical parameters. In this work, we applied the traditional Hertz-Sneddon model to determine YM parameter. As reported in Figure 1E, the acquired data are apparently well described by the Hertz-Sneddon model on a large subset of data. It has been reported that this is not always the case and deviations from the Hertz-Sneddon model have been often reported. We faced this with an operational approach by selecting all the curves which were more effectively described by the model and by disregarding the others. As a consequence of this simplified approach, it is possible that the YM values reported in this article could be affected by a systematic bias. However, since the aim of the investigation is how the targeted therapy affects mechanical properties of CLL cells, and given the fact that the supposed biases do not alter the general trend of the data, our practical approach can be considered correct and effective.

AFM-FS measurements on fresh cells.

The uniformity of the response to AFM-FS of the B lymphocytes coming from different patients or different healthy donors was firstly tested. We measured the rigidity of single CLL cells isolated from 6 different patients, they showed similar rigidity values, ranging

between 375 and 580 Pa (Fig. S2, blue data), and HB cells the rigidity values attested between 816 and 1,606 Pa (Fig. S2, red data).

We collected the data obtained for all the patients or all the healthy donors. Figure S2 displays the collective values of rigidity measured on the cells within 3 hours from isolation from different CLL patients (n=5) and healthy donors (n=5). The rigidity values of fresh CLL cells (501 [451-538] Pa) were significantly lower than the values obtained for fresh HB cells (1,092 [980-1,174] Pa), with a $p<0.0001$. No significant differences were found in terms of cell viability during the measurements, comparing CLL cells or HB cells.

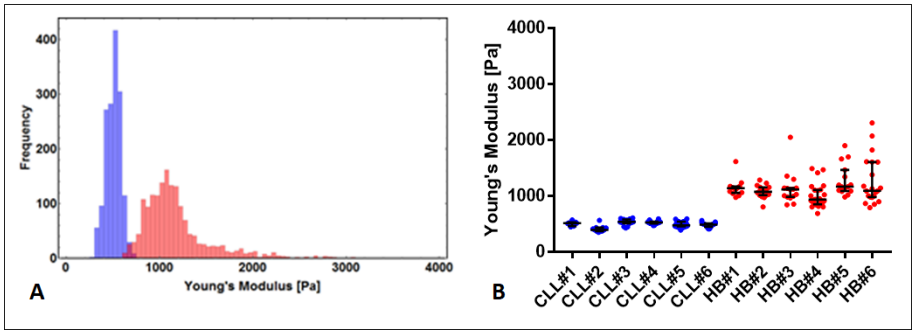

Figure S2. Uniformity of response to AFM-FS measurements assessed for CLL and HB fresh cells. Fresh cells from 6 CLL patients (blue) and 6 HB donors (red) were tested. (A) The histograms include all the measurements acquired on the single cells (16 measurements on each cell per each cell). (B) Swarm plot of fresh single cells from 6 CLL patients and 6 HB donors, where each dot represents the median value of the measurements on a single cell and the black bars report the median and interquartile range of the presented data.

Stiffness of fresh vs thawed cells

In order to increase the number of measurements we tested the response to the primary cells to a freezing procedure. To verify whether there was no difference between the rigidity of fresh B cells versus thawed B cells we compared samples coming from 5 CLL patients and 5 HB donors before and after freezing. For each sample a fraction of the fresh cells was measured within 3 hours from the isolation, while the remaining fraction was frozen and thawed only before measuring. We found no appreciable difference in the rigidity values of CLL or HB cells comparing thawed cells and fresh cells for each donor, as reported in Figure S3-A and S3-B. All together, the data show a similar distribution of rigidity of the fresh CLL or HB cells if compared to the rigidity of the respective thawed cells (CLL: fresh 501 [451-538] Pa, vs. thawed 402 [325-486] Pa; HB: fresh 1,092 [980-1,174] Pa vs. thawed 1,243 [1,032-1,530] Pa) (Fig. S4). Accordingly, since we verify that the freezing procedure is not affecting the relative difference between CLL and HB cells, we extended our further measurements to thawed cells.

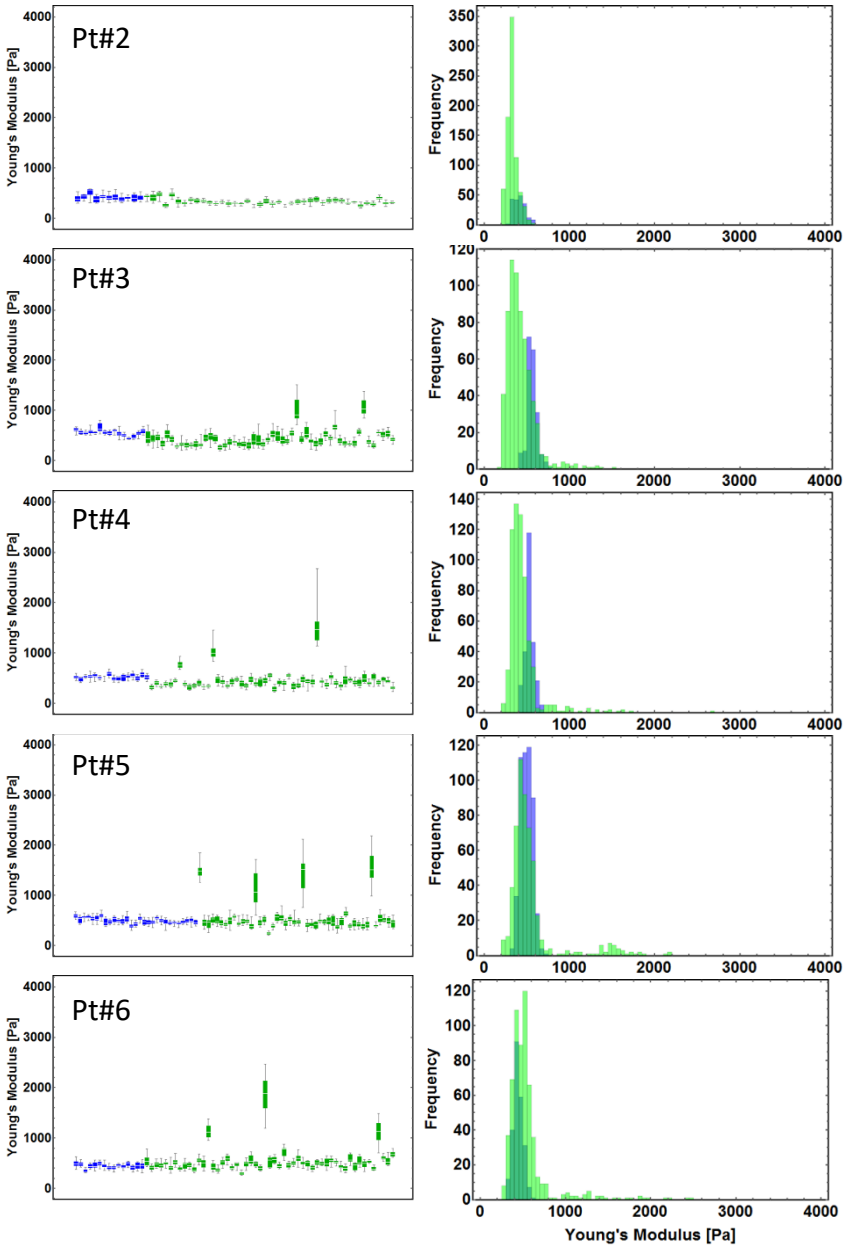

Figure S3-A. Comparison of the rigidity between fresh and thawed CLL cells. The figure reports the measure of the YM obtained for fresh (blue) and thawed (green) CLL cells for the single patients #2, #3, #4, #5, #6. (Left) Each box comprises all the YM values measured for a single cell: the median value (middle white line) and the interquartile range of values (25-75%, colored box) are represented, the lower and upper fences correspond to the 0-100% values (black bars). (Right) The histograms include all the measurements acquired on single cells.

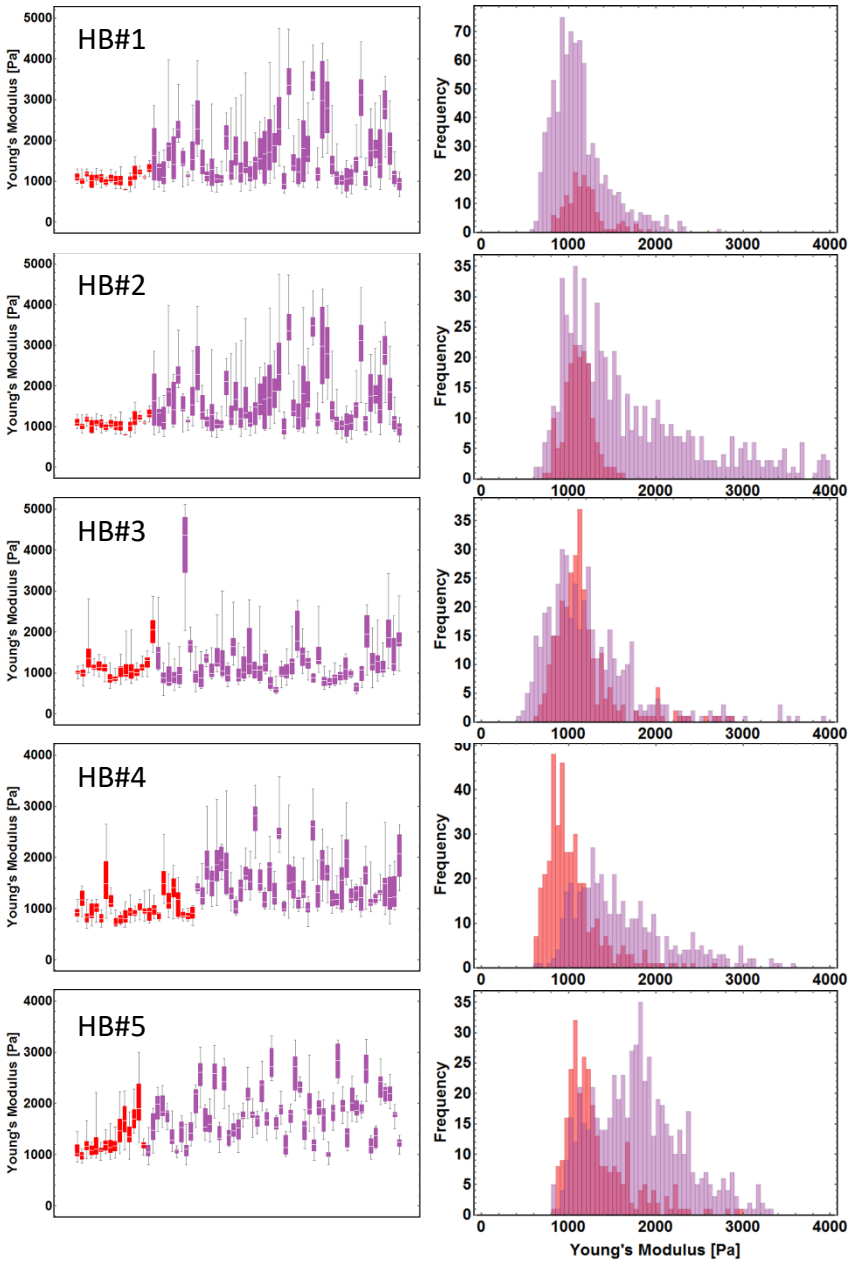

Figure S3-B. Comparison of the rigidity between fresh and thawed HB cells. The figure reports the measure of the YM obtained for fresh (red) and thawed (purple) HB cells for the single healthy donors #1, #2, #3, #4, #5. (Left) Each box comprises all the YM values measured for a single cell: the median value (middle white line) and the interquartile range of values (25-75%, colored box) are represented, the lower

and upper fences correspond to the 0-100% values (black bars). (Right) The histograms include all the measurements acquired on single cells.

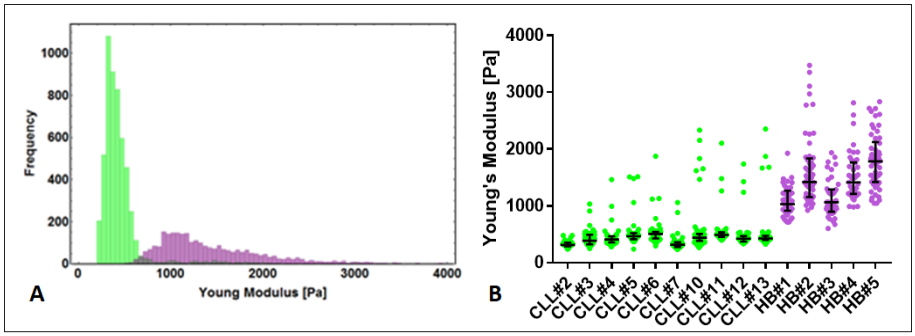

Figure S4. Uniformity of response to AFM-FS measurements assessed for CLL and HB thawed cells. Thawed cells from 10 CLL patients (light green) and 5 HB donors (violet) were tested. (A) The histograms include all the measurements acquired on the single cells (16 measurements on each cell). (B) Swarm plot of thawed single cells from 10 CLL patients and 5 HB donors, where each dot represents the median value of the measurements on a single cell and the black bars report the median and interquartile range of the presented data.

Drug treatments

All treatments were performed in RPMI before cell seeding on coated plates. Fasudil (Selleckchem, S1573) has been administered at a final concentration of 10 µM, while ibrutinib (Selleckchem, S2680) has been administered at concentrations of 1 and 10 µM. After 4 hours of incubation, drugs were removed, and cells were plated on coated plates. Also longer incubation (24 hours) have been tested finding no significant differences if compared to the 4 hours treatment (Fig. S11). Conversely, Cytochalasin D (Sigma) has been added directly to PBS, incubated for 10 minutes and maintained in the plate during

measurements. All treatments, including poli-L-ornitine coating, do not affect cell viability (Fig. S5).

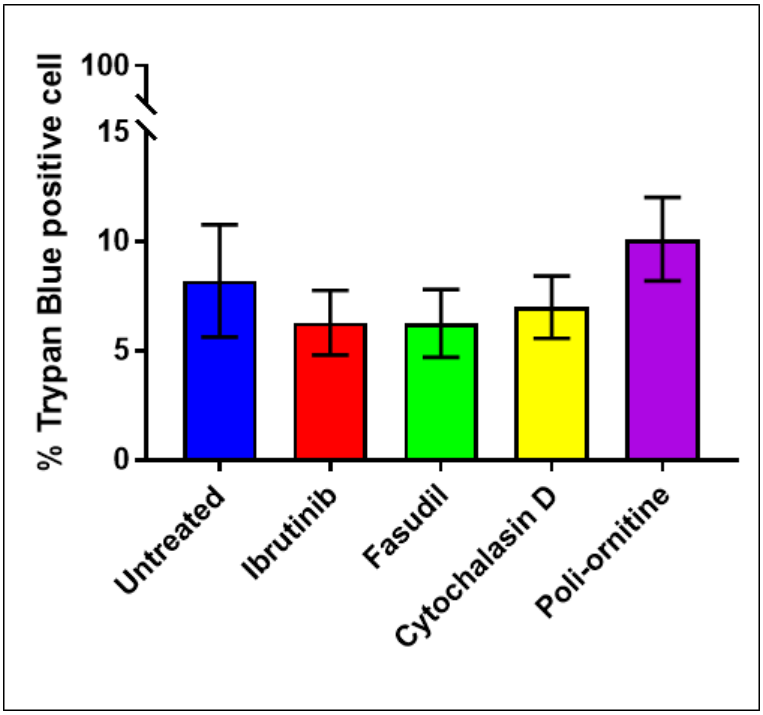

Figure S5. Cell viability count. Histogram of the percentage of dead cells (CLL and HB) untreated (blue) and treated with ibrutinib for 4 hours (red), with fasudil for 4 hours (green), with cytochalasin D for 2 hours (yellow) and plated on poli-L-ornitine for 2 hours (purple) showing that none of the used drugs affect the cell viability. The fences represent the standard deviations of the measured data.

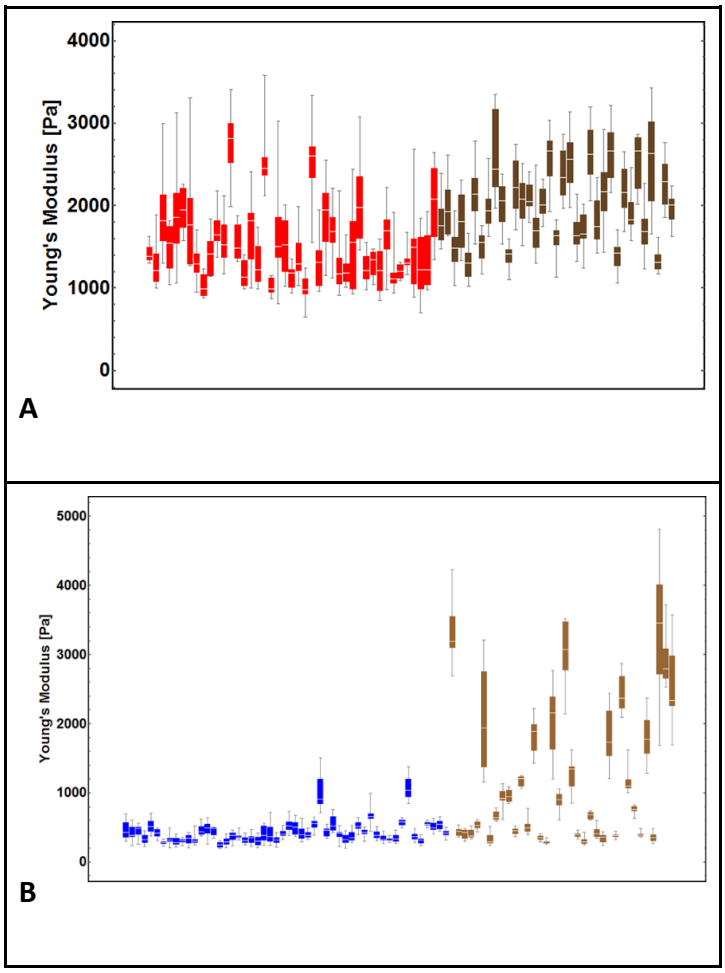

Figure S6. Effect of in vitro fasudil treatment on the cell rigidity. (A) Whisker plot of YM values acquired on HB#4 cells before (red, 43 cells) and after (dark brown, 35 cells) 4h of treatment with fasudil. (B) Whisker plot of YM values acquired on CLL Patient#3 cells before (blue, 52 cells) and after (brown, 36 cells) 4h of treatment with fasudil. Each box comprises all the YM values measured for a single cell: the median value (middle white line) and the interquartile range of values (25-75%, colored box) are represented, the lower and upper fences correspond to the 0-100% values (black bars).

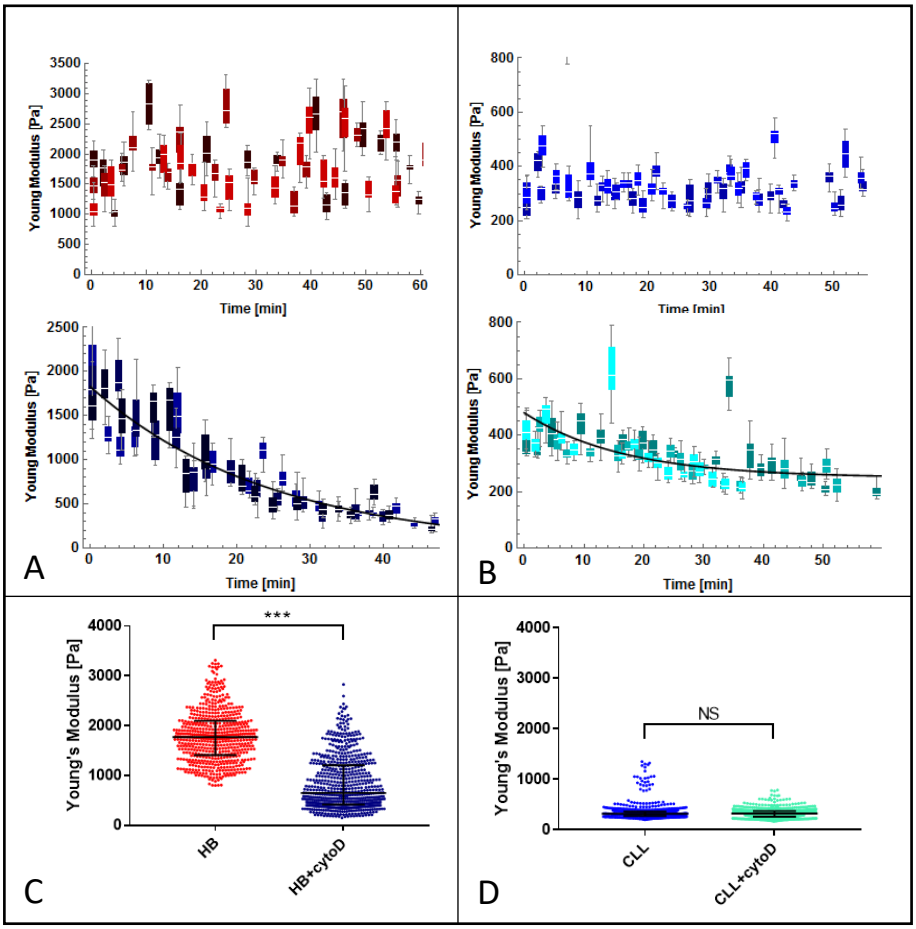

Figure S7. Time effect of in vitro cytochalasin D treatment. (A) Whisker plot of HB#5 untreated (top panel) and treated with cytochalasin D (bottom panel in dark blue). (B) Whisker plot of Patient#7 untreated (top panel) and treated with cytochalasin D (bottom panel). After 10 min from the cytochalasin D addition, data were taken in triplicate; each sample was measured for approximately 1 hour, indicating a progressive decrease of the YM during the treatment. Each box contains all the measures on each cell, reporting the median value (middle white line) and the interquartile range of values (25-75%, colored box), while the lower and upper fences correspond to the 0-100% values (black bars). (C) HB#5 before (54 cells in red) and after (51 cells in dark blue) the treatment with cytochalasin D. The black continuous lines represent a guide to the eyes. (D) Patient#7 before (54 cells in blue) and after (53 cells in light blue) the treatment with cytochalasin D. Every dot represents a single measurement acquired on the cells. The data show a median YM value of 1772 [1364-2057] Pa before and 649 [369-1163] Pa after the treatment with cytochalasin D for HBs, and 317 [281-348] Pa before and 322 [262-379] Pa after for CLL cells.

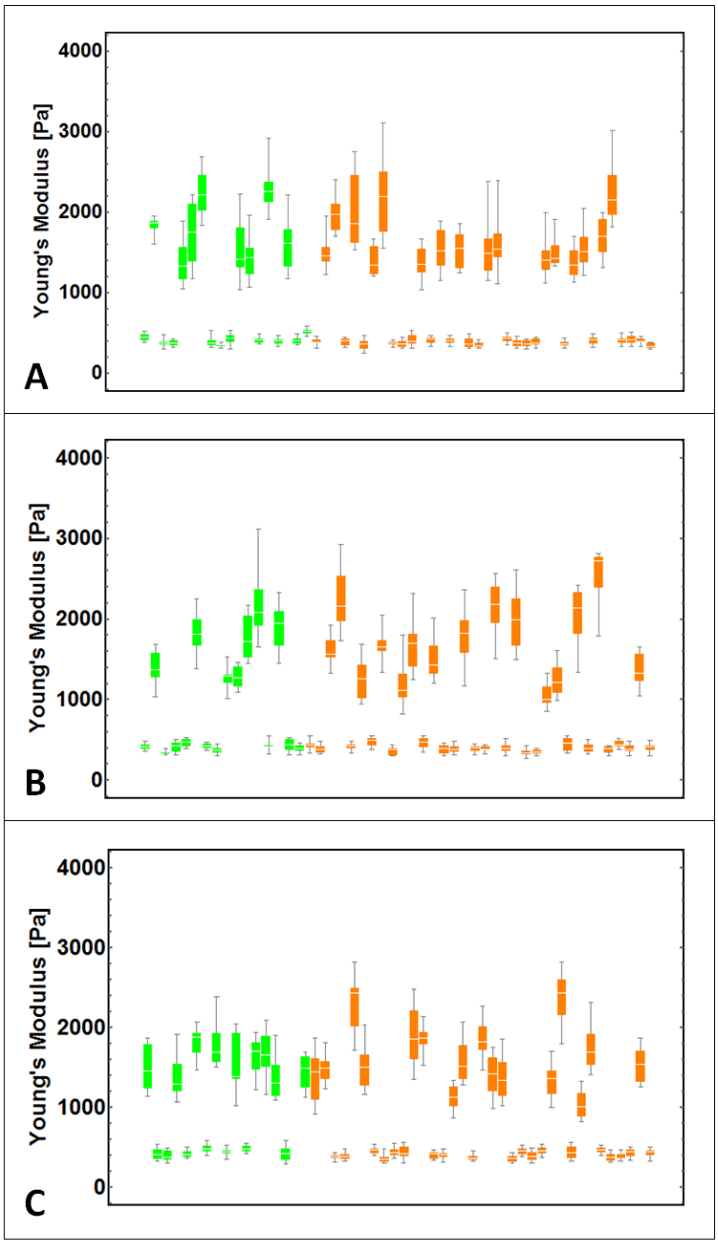

Figure S8. Comparison of the effect of different concentrations of Ibrutinib on 3 CLL patients. Patient#6 (A), Patient#2 (B) and Patient#13 (C) treated with ibrutinib at a final concentration of 10 µM (green) and 1 µM (orange).

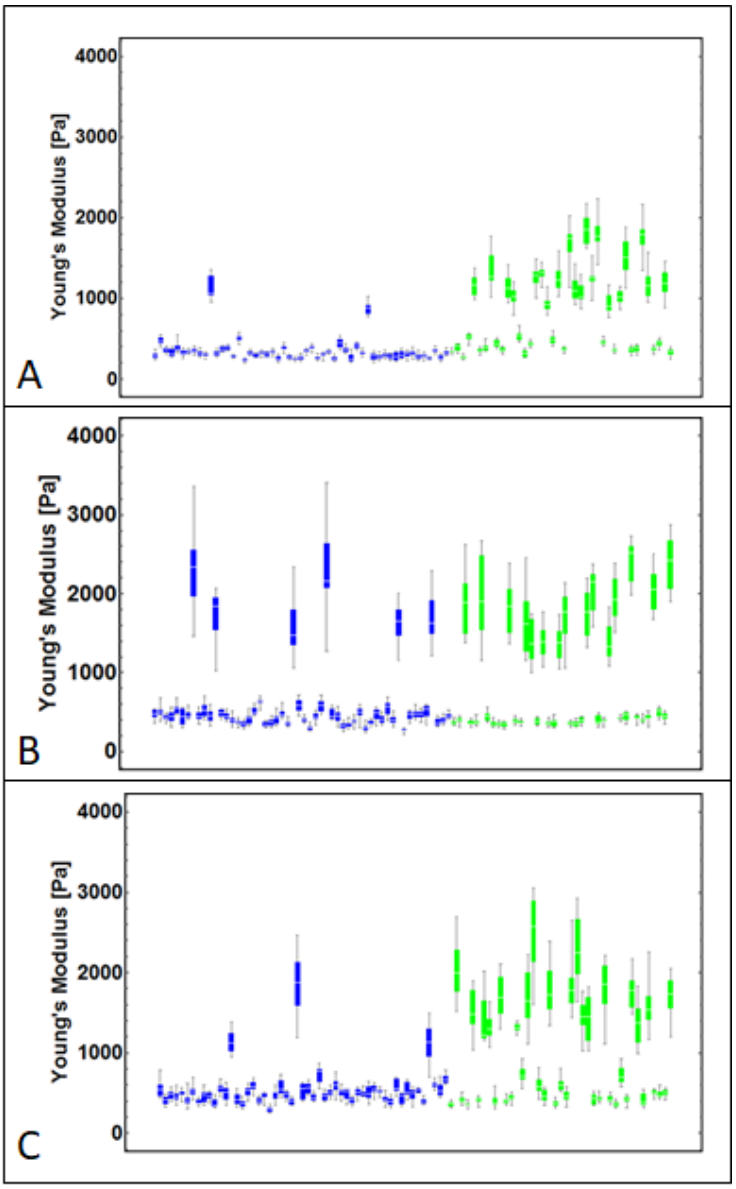

Figure S9. Effect of in vitro ibrutinib treatment on 3 different patients. Whisker plots of (A) Patient#7, (B) Patient#10 and (C) Patient#12, untreated (blue) and after 4h of treatment with ibrutinib (green). Each box represents all the measures on each cell, reporting the median value (middle white line) and the interquartile range of values (25-75%, colored box), while the lower and upper fences correspond to the 0-100% values (black bars).

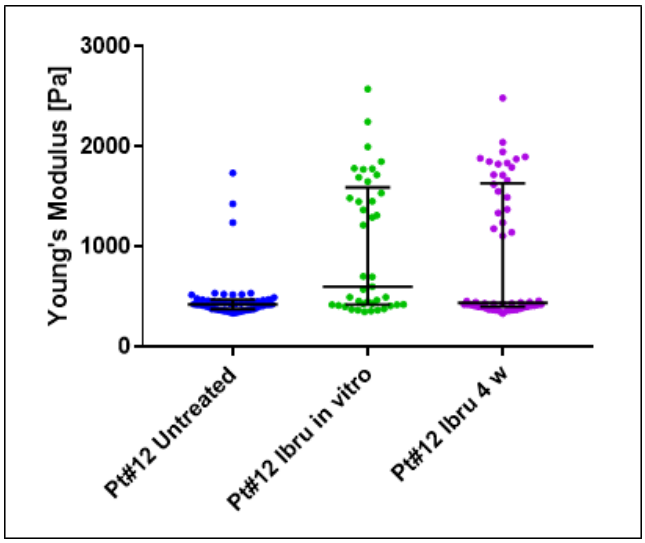

Figure S10. Comparison of in vitro and in vivo ibrutinib treatment on CLL cells of patient#12. Patient#12 before treatment (blue), after 4 hours of treatment with ibrutinib in vitro (green) and after 4 weeks of therapy with ibrutinib (purple).

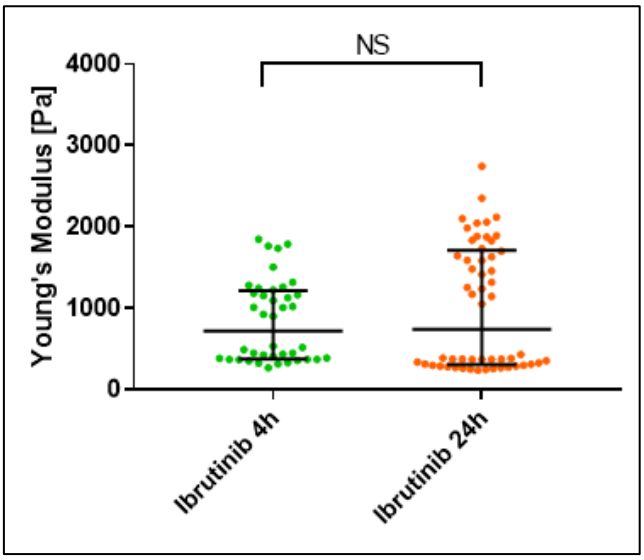

Figure S11. Comparison between time treatments. Swarm plot of cells from a single CLL patient treated in vitro with ibrutinib for 4 hours (green) and 24 hours (orange) where each dot represents the median value of a single cell. No differences have been found depending on the treatment time.

	Rai	Binet	CD38 result	IGHV identity	FISH	Clin. course	Resp. ibrutinib	AFM YM (Pa)	RT-DC YM (Pa)
PT#1	NA	NA	NA	NA	NA	NA	NA	511.64	NA
PT#2	0	A	12.3	100	del13q14.3 (90.6%, homozygous 27.8%, heterozygous 62.8%)	Progr.	YES	366.01	1259.03
PT#3	0	A	12.4	NA	del13q14.3 (20%), del13q34 (16.5%)	Stable	NA	476.04	1205.52
PT#4	1	A	0.68	95.49	del13q14.3 (29%), del13q34 (17.4%)	Stable	NA	450.11	1234
PT#5	0	A	5.2	92.28/96.18	NA	Stable	NA	494.24	NA
PT#6	1	A	57.2	NA	NA	Stable	NA	519.24	NA
PT#7	0	A	19.1	NA	NA	Stable	NA	326.94	1288.4
PT#8	0	A	NA	NA	NA	Stable	NA	NA	1369.77
PT#9	0	A	3	88.9	NA	Progr.	NA	NA	1211.87
PT#10	0	A	0.1	93.33	Normal	Stable	NA	442.1	NA
PT#11	0	A	NA	96.26	del13q14.3 (90%)	Stable	NA	458.34	NA
PT#12	0	A	15.9	98.30	Normal	Progr.	YES	416.13	NA
PT#13	1	A	2	95.53	del17p13.1 (12%), +12 (80%)	Progr.	YES	431.41	NA

Tab S1. Clinical and biological characteristics of the patients used for the experiments presented in the manuscript (n=13). Samples were collected from patients with stable or progressive disease courses. NA=not available.

3.9 Bibliography

1. Hallek M. Chronic lymphocytic leukemia: 2020 update on diagnosis, risk stratification and treatment. *Am J Hematol* 2019; **94**: 1266-1287.

2. Davids MS and Burger JA. Cell trafficking in chronic lymphocytic leukemia. *Open J Hematol* 2012; **3**: -3.

3. Scielzo C, Hacken ET, Bertilaccio MT, Muzio M, Calissano C, Ghia P, *et al.* How the microenvironment shapes chronic lymphocytic leukemia: the cytoskeleton connection. *Leuk Lymphoma* 2010; **51**: 1371-1374.

4. Hacken ET, Scielzo C, Wierda WG, Keating MJ, O'Brien S, Ghia P, *et al.* Ibrutinib differentially interferes with surface IgM and IgD BCR signaling kinetics in chronic lymphocytic leukemia. *Blood* 2013; **122**: 4143.

5. Freise KJ, Jones AK, Eckert D, Mensing S, Wong SL, Humerickhouse RA, *et al.* Impact of venetoclax exposure on clinical efficacy and safety in patients with relapsed or refractory chronic lymphocytic leukemia. *Clin Pharmacokinet* 2017; **56**: 515-523.

6. Schiattone L, Ghia P, Scarfò L. The evolving treatment landscape of chronic lymphocytic leukemia. *Curr Opin Oncol* 2019; **31**: 568-573.

7. O'Brien S, Jones JA, Coutre SE, Mato AR, Hillmen P, Tam C, *et al.* Ibrutinib for patients with relapsed or refractory chronic lymphocytic leukaemia with 17p deletion (RESONATE-17): a phase 2, open-label, multicentre study. *Lancet Oncol.* 2016; **17**: 1409-1418.

8. Deeks ED. Ibrutinib: a review in Chronic Lymphocytic Leukemia. *Drugs* 2017; **77**: 225-236.

9. Herman SEM, Gordon AL, Hertlein E, Ramanunni A, Zhang X, Jaglowski S *et al.* Bruton tyrosine kinase represents a promising therapeutic target for treatment of chronic lymphocytic leukemia and is effectively targeted by PCI-32765. *Blood* 2011; **117**: 6287-6296.

10. Burger JA and Wiestner A. Targeting B cell receptor signalling in cancer: preclinical and clinical advances. *Nat Rev Cancer*. 2018; **18**:148-167.

11. Haga M, Yamashita A, Paszkowiak J, Sumpio BE, Dardik A. Oscillatory shear stress increases smooth muscle cell proliferation and akt phosphorylation". *Eur J Vasc Surg* 2003; **37**: 1277-1284.

12. Butcher D, Alliston T, Weaver V. A tense situation: forcing tumour progression. *Nat Rev Cancer* 2009; **9**: 108-122.

13. Lim CG, Jang J, Kim C. Cellular machinery for sensing mechanical force. 2018 *BMB Rep* 2018; **51**: 623-629.

14. Wang JH and Li B. Application of cell traction force microscopy for cell biology research. *Met Mol Biol* 2009; **586**: 301-313.

15. Polacheck WJ, Chen CS. Measuring cell-generated forces: a guide to the available tools. *Nat Met* 2017; **13**: 415–423.

16. Van Helvert S, Storm C, and Friedl P. Mechanoreciprocity in cell migration. *Nat Cell Biol* 2018; **20**: 8-20.

17. Plodinec M, Loparic M, Monnier CA, Obermann EC, Zanetti-Dallenbach R, Oertle P, *et al.* The nanomechanical signature of breast cancer. *Nat Nanotechnol.* 2012; **7**: 757-65.

18. Byun S, Son S, Amodei D, Cermak N, Shaw J, Kang JH, *et al.* Characterizing deformability and surface friction of cancer cells. *Proc Natl Acad Sci USA*. 2013; **110**: 7580-7585.

19. Zheng Y, Wen J, Nguyen J, Cachia MA, Wang C, Sun Y. Decreased deformability of lymphocytes in chronic lymphocytic leukemia. *Sci Rep* 2015; **5**: 7613.

20. Lam WA, Rosenbluth MJ, Fletcher DA. Chemotherapy exposure increases leukemia cell stiffness. *Blood* 2007; **109**: 3505-3508.

21. Wu PH, Aroush DR, Asnacios A, Chen WC, Dokukin ME, Doss BL, *et al.* A comparison of methods to assess cell mechanical properties. *Nat Met* 2018; **15**: 491-498.

22. Jalili N, Laxminarayana K. A review of atomic force microscopy imaging systems: application to molecular metrology and biological sciences. 2004 M E 2004; **14**: 907-945.

23. Cassina V, Manghi M, Salerno D, Tempestini A, Iadarola V, Nardo L, *et al.* Effects of cytosine methylation on DNA morphology: an atomic force microscopy study. *BBA - Gen Subj* 2016; **1860**: 1-7.

24. Figuereido I, Paiotta A, Magro RD, Tinelli F, Corti R, Re F *et al*. A new approach for glyco-functionalization of collagen-based biomaterials. *Int J Mol Sci* 2019; **20**: 1747.

25. Thomas G, Burnham NA, Camesano TA, Wen Q. Measuring the mechanical properties of living cells using atomic force microscopy. *J Vis Exp* 2013; **76**: 50497.

26. Lee Y, Koay EJ, Zhang W, Qin L, Kirui DK, Hussain F, *et al.* Human equilibrative nucleoside transporter-1 knockdown tunes cellular mechanics through epithelial-mesenchymal transition in pancreatic cancer cells. *PLoS ONE* 2014; **9**: e107973.

27. Lekka M, Fornal M, Pyka-Fościak G, Lebed K, Wizner B, Grodzicki T *et al.* Erythrocyte stiffness probed using atomic force microscope. *Biorheol* 2005; **42**: 307-317.

28. Dulinska I, Targosz M, Strojny W, Lekka M, Czuba P, Balwierz W *et al.* Stiffness of normal and pathological erythrocytes studied by means of atomic force microscopy. *J Biochem Bioph Meth* 2006; **66**: 1-11.

29. Guz NV, Patel SJ, Dokukin ME, Clarkson B, Sokolov I. Biophysical differences between chronic myelogenous leukemic quiescent and proliferating stem/progenitor cells. *Nanomed Nanotechnol* 2016; **12**: 2429-2437.

30. Fortier H, Variola F, Wang C, Zou S. AFM force indentation analysis on leukemia cells. *Anal Met* 2016; **8**: 4421-4431.

31. Otto O, Rosendahl P, Mietke A, Golfier S, Herold C, Klaue D, *et al.* Real-time deformability cytometry: on-the-fly cell mechanical phenotyping. *Nat Met* 2015; **12**: 199-202.

32. Mietke A, Otto O, Girardo S, Rosendahl P, Taubenberger A, Golfier S, *et al.* Extracting cell stiffness from real-time deformability cytometry: theory and experiment. *Biophys J* 2015: **109**: 2023-2036.

33. Herbig M, Kräter M, Plak K, Müller P, Guck J, Otto O. Real-time deformability cytometry: label-free functional characterization of cells. *Methods Mol Biol* 2018; **1678**: 347-369.

34. Golfier S, Rosendahl P, Mietke A, Herbig M, Guck J, Otto O. High-throughput cell mechanical phenotyping for label-free titration assays of cytoskeletal modifications". *Cytoskeleton* 2017; **74**: 283-296.

35. Hallek M, Cheson BD, Catovsky D, Caligaris-Cappio F, Dighiero G, Döhner H, *et al*. Guidelines for the diagnosis and treatment of chronic lymphocytic leukemia: a report from the International Workshop on Chronic Lymphocytic Leukemia updating the National Cancer Institute-Working Group 1996 guidelines. *Blood* 2008; **111**: 5446-5456.

36. Hutter JL, Bechhoefer J. Calibration of atomic force microscope. *Trends Pharmacol Sci Rev Sci Instrum* 1993; **64**: 1868-1873.

37. Sneddon IN. The relation between load and penetration in the axisymmetric boussinesq problem for a punch of arbitrary profile. *Int J Eng Sci* 1965; **3**: 47-57.

38. Dokukin ME and Sokolov I. On the measurements of rigidity modulus of soft materials in nanoindentation experiments at small depth. *Macromolecules* 2012; **45**: 4277-4288.

39. Guz NV, Dokukin ME, Kalaparthi V, Sokolov I. If cell mechanics can be described by elastic modulus: study of different models and probes used in indentation experiments. *Biophys J* 2014; **107**: 564-575.

40. Lekka M, Laidler P, Gil D, Lekki J, Stachura Z, Hrynkiewicz AZ. Elasticity of normal and cancerous human bladder cells studied by scanning force microscopy. *Eur Biophys J* 1999; **28**: 312-316.

41. Butt HJ, Cappella B, Kappl M. Force measurements with the atomic force microscope: technique, interpretation and applications. *Surf Sci Rep* 2005; **59**: 1-52.

42. Panciera T, Citron A, Di Biagio D, Battilana G, Gandin A, Giulitti S *et al*. Reprogramming normal cells into tumour precursors requires ECM stiffness and oncogene-mediated changes of cell mechanical properties. *Nat Mater* 2020; **19**: 797-806.

43. Zhang Z, Ren J, Li Z, Nong L, Wu G. Fasudil inhibits lung carcinoma-conditioned endothelial cell viability and migration. *Oncol Rep* 2012; **27**: 1561-1566.

44. Elson EL, Pasternak C, Daily B, Young JI, McConnaughey WB. Cross-linking surface immunoglobulin increases the stiffness of lymphocytes". *Mol Immunol* 1984; **21**: 1253-1257.

45. Wang N, Butler JP, Ingber DE. Mechanotransduction across the cell surface and through the cytoskeleton. *Science* 1993; **260**: 1124-1127.

46. Wakatsuki T, Schwab B, Thompson NC, Elson EL. Effects of cytochalasin D and latrunculin B on mechanical properties of cells. *J Cell Sci* 2001; **114**: 1025-1036.

47. Schliwa M. Action of cytochalasin D on cytoskeletal networks. *J Cell Biol* 1982; **92**: 79-91.

48. Li M, Liu L, Xiao X, Xi N, Wang Y. Viscoelastic properties measurement of human lymphocytes by atomic force microscopy based on magnetic beads cell isolation. *IEEE T Nanobiosci* 2016; **15**: 398-411.

49. Toepfner N, Herold C, Otto O, Rosendahl P, Jacobi A, Kräter M. *et al.* Detection of human disease conditions by single-cell morpho-rheological phenotyping of blood. *eLife* 2018; **7**: e29213.

50. Laperrousaz B, Berguiga L, Nicolini FE, Martinez-Torres C, Arneodo A, Satta VM, *et al.* Revealing stiffening and brittling of chronic myelogenous leukemia hematopoietic primary cells through their temporal response to shear stress. *Phys Biol* 2016; **13**: 03LT01.

Chapter 4

Summary, conclusions and future perspectives

The high frequency and mortality rate of cancer make it one of the most dangerous and deadly diseases [Ferlay J *et al.*, 2015]. Mutations occurring in oncogenes or in their regulatory sequences impair intracellular signalling pathways, ultimately enhancing survival and growth of tumor cells [Cairns RA *et al.*, 2011]. In addition, the influence of the microenvironment on the metabolic phenotype affects cancer progression, response to therapy and patient outcome [Lunt SJ *et al.*, 2008]. At last, cancer cells gain the ability to migrate through the lymph and blood systems, and are potentially able to colonize new tissues *via* metastatic invasion [Chaffer CL and Weinberg RA, 2020]. These features, not entirely elucidated yet, make cancer extremely hard to cure and almost impossible to be predicted.

The biomechanical properties of the cell and of its components play a crucial role in the onset and progression of cancer [Yallapu MM *et al.*, 2015]. Indeed, they are known to be strictly connected both with oncogene regulation [Pienta KJ *et al.*, 1989; De S and Michor F, 2011] and the structural reorganization of metastatic cells [Carter SB, 1965; Weaver AM, 2006]. The field of nanomechanics can offer a significant contribution in shedding light on these mechanisms, since it grants the opportunity to observe these events from a different and detailed point of view. As a matter of fact, the possibility to study a single DNA molecule or a single cell can provide a deeper insight on the onset of cancer as well as on novel therapies [Kozminsky N and Sohn LL, 2020]. The thesis work herein presented provides several evidences of the contribution that nanomechanics can offer to cancer research.

The investigation of the nanomechanical properties of oncogenes can facilitate the comprehension of their regulation aimed at the development of novel therapies. The mechanical characterization of the promoter of an oncogene, as in the case of the *c-KIT* promoter, provides the possibility of speculating on its function and on a possible explanation of the role of G4s within its sequence. As our results revealed, in physiological conditions of pH, temperature and ionic strength, the G4 folding occurs at negative supercoiling. This condition better mimics the mechanical denaturation occurring within the chromatin during the transcription/replication processes compared to heat or acid induced denaturation. We showed that, in this regime, the folding of the G4s facilitates the opening of the denaturation bubble by lowering the energy required to separate the strands despite the high GC content. These findings suggest that the folding of the three G4s structures present in the *c-KIT* promoter stabilizes the opening of this regulative region, exposes the promoter to the assembly of the transcriptional machinery, and ultimately favors the transcription of *c-KIT*. Since all the forms of cancer, in which KIT is involved, are associated to an overexpression of the protein [Ray P *et al.*, 2008; Cruse G *et al.*, 2015], the *c-KIT* promoter represents an eligible target to prevent the oncogene overexpression. In the last few years, small molecules such as AQ1 and AN6, able to specifically target *c-KIT* G4s, were proposed [Zorzan E *et al.*, 2016], and the interaction of this region with transcription factors was also found [Balasubramanian S *et al.*, 2011]. In the near future, we would orient our work on characterizing by means of MT the dynamics of interaction of these

drugs or transcriptional factors for the *c-KIT* promoter, and their capability of inhibiting the expression of the oncogene.

The process of metastatization plays a pivotal role in the progression of cancer, being the most deadly and the least known [Seyfried TN and Huysentruyt LC, 2013]. During migration, a cell senses the environment and responds to its changes by modifying its own structure in a continuous process known as mechanoreciprocity [Byun S *et al.*, 2013]. An impairment of this process promotes cancer progression and raises the invasive potential of migrating tumor cells [Plodinec M *et al.*, 2012]. B lymphocytes are intrinsically dynamic cells that continuously migrate across several organs, thus constantly modifying their mechanical behavior. The outbreak of CLL entails an impairment of their dynamic activities and, reasonably, of their mechanical processes. Besides, targeted therapies reversibly restore their behavior, with a mechanism that is still far from being understood. In this context, we studied the rigidity of living cells from CLL patients and healthy donors by means of two single cell techniques. Moreover, we observed the effect of the targeted therapy ibrutinib on those cells both *in vitro* and in patients under clinical trial. Our data show one side of this behavior, which can be summarized in three milestones: (i) there is a basic difference between healthy and leukemic cells, regardless of the used technique, (ii) a softening of leukemic cells when stopped on a substrate (i.e. AFM setup) in contrast with their hardening when floating on a stream (i.e. RT-DC setup), and (iii) the selective effect of the targeted therapy on leukemic

cells, that recover the rigidity values of healthy cells, while the latter are unaffected by the drug. Taken together, these data show a dynamic behavior of leukemic cells, which seem to continuously modify their rigidity depending on the external stimuli. In contrast, the rigidity of healthy cells appears unaltered, maintaining their mechanical properties regardless of the external stimuli. This outcome may depend on an impairment of the mechanoreciprocity process in leukemic B lymphocytes, while ibrutinib can temporarily restore its proper functioning. Despite these findings, we are still far from understanding the mechanisms that drive the mechanics of cancer cells. Anyway, by a systematical monitoring of the rigidity of the cells of CLL patients under ibrutinib treatment, we could provide a deeper understanding of this complex aspect and we could obtain a personalized clinical follow-up.

As a broader conclusion, taken together our data clearly indicate that nanomechanics represents an essential tool to help dissecting the mechanisms that underlie the onset, progression and metastatization of cancer in a patient-orientated perspective, from the diagnosis of the disease and, through monitoring, to a personalized treatment.

4.1 Bibliography

- Ferlay J, Soerjomataram I, Dikshit R, Eser S, Mathers C, Rebelo M, *et al*. Cancer incidence and mortality worldwide: sources, methods and major patterns in GLOBOCAN 2012. *Int. J. Cancer*. **2015**, 136, 359-386.
- Cairns RA, Harris I, Mak, T. Regulation of cancer cell metabolism. *Nat. Rev. Cancer*. **2011**, 11, 85-95.
- Lunt SJ, Chaudary N, Hill RP. The tumor microenvironment and metastatic disease. *Clin. Exp. Metastasis*. **2009**, 26, 19-34.
- Chaffer CL and Weinberg RA. A perspective on cancer cell metastasis. *Science*. **2020**, 331, 1559-1564.
- Yallapu MM, Katti KS, Katti DR, Mishra SR, Khan S, Jaggi M, *et al*. The roles of cellular nanomechanics in cancer. *Med. Res. Rev*. **2015**, 35, 198-223.
- Pienta KJ, Partin AW, Coffey DS. Cancer as a disease of DNA organization and dynamic cell structure. *Cancer Res*. **1989**, 49, 2525-2532.
- De S and Michor F. DNA secondary structures and epigenetic determinants of cancer genome evolution. *Nat. Struct. Mol. Biol*. **2011**, 18, 950-955.
- Carter SB. Principles of cell motility: the direction of cell movement and cancer invasion. *Nature*. **1965**, 208, 1183-1187.
- Weaver AM. Invadopodia: specialized cell structures for cancer invasion. *Clin. Exp. Metastasis*. **2006**, 23, 97-105.
- Kozminsky M and Sohn LL. The promise of single-cell mechanophenotyping for clinical applications. *Biomicrofluidics*. **2020**, 14, 031301.
- Ray P, Krishnamoorthy N, Ray A. Emerging functions of c-kit and its ligand stem cell factor in dendritic cells: regulators of T cell differentiation. *Cell Cycle*. **2008**, 7, 2826-2832.
- Cruse G, Metcalfe DD, Olivera A. Functional deregulation of KIT: link to mast cell proliferative diseases and other neoplasms. *Immunol. Allergy Clin. North. Am*. **2014**, 34, 219-237.
- Zorzan E, Da Ros S, Musetti C, Shahidian LZ, Coelho NF, Bonsembiante F, *et al*. Screening of candidate G-quadruplex ligands for the human c-KIT promotorial region and their effects in multiple in-vitro models. *Oncotarget*. **2016**, 7, 21658-21675.
- Balasubramanian S, Hurley LH, Neidle S. Targeting G-quadruplexes in gene promoters: a novel anticancer strategy? *Nat. Rev. Drug Discov*. **2011**, 10, 261-275.

- Seyfried TN and Huysentruyt LC. On the origin of cancer metastasis. *Crit. Rev. Oncog*. **2013**, 18, 43-73.
- Byun S, Son S, Amodei D, Cermak N, Shaw J, Kang JH, *et al*. Characterizing deformability and surface friction of cancer cells. *Proc. Natl. Acad. Sci. USA*. **2013**, 110, 7580-7585.
- Plodinec M, Loparic M, Monnier CA, Obermann EC, Zanetti-Dallenbach R, Oertle P, *et al*. The nanomechanical signature of breast cancer. *Nat. Nanotechno*l. **2012**, 7, 757-765.

4.2 Publication outside the thesis topic

Double-stranded flanking ends affect the folding kinetics and conformational equilibrium of G-quadruplexes forming sequences within the promoter of KIT oncogene

G. Vesco, M. Lamperti, D. Salerno, C. A. Marrano, V. Cassina, R. Rigo, E. Buglione, M. Bondani, G. Nicoletto, C. Sissi, F. Mantegazza, L. Nardo

Abstract

G-quadruplex forming sequences embedded within gene promoters play a crucial epigenetic role in regulating the gene expression. KIT is a widely studied oncogene, whose promoter contains three different G-quadruplex forming sequences, usually referred to as c-kit1, c-kit2 and c-kit*. Recently, c-kit2 has been reported to fold according to a multi-step process involving folding intermediates. Whereas for c-kit1 and c-kit2 available studies cover ensemble and single molecules analyses, for c-kit*, the latter one to be individuated, detailed single molecule studies were not performed yet. Here, by exploiting fluorescence resonance energy transfer, both in ensemble and at the single molecule level, we investigated the folding of expressly designed constructs in which either c-kit2 or c-kit* are flanked by double stranded DNA segments. These constructs are intended to model the physiological assembly of G-quadruplex forming sequences embedded within promoters. To assess whether the presence of flanking ends at the borders of the G-quadruplex actually affects the folding, we

studied under the same protocols the folding of oligonucleotides corresponding to the minimal G-quadruplex forming sequences. Data suggest that addition of flanking ends results in biasing both the final equilibrium state and the folding kinetics. A previously unconsidered aspect is thereby unravelled, which ought to be taken into account to achieve a deeper insight of the complex relationships underlying the fine tuning of the gene-regulatory properties of these fascinating DNA structures.